ELSEVIER

Prog. Polym. Sci. 27 (2002) 1473–1572

PROGRESS IN
POLYMER SCIENCE

www.elsevier.com/locate/ppolysci

Polyelectrolyte–surfactant complexes (synthesis, structure and materials aspects)

Andreas F. Thünemann

Fraunhofer Institute for Applied Polymer Research, Geiselbergstrasse 69, D-14476 Golm, Germany

Received 29 October 2001; revised 20 February 2002; accepted 21 February 2002

Abstract

Self-assembled polyelectrolyte–surfactant complexes in the solid state and as nanoparticles are the topic of this review. These materials combine the properties of polymers (mechanical stability) and surfactants (formation of highly ordered mesophases). Their building principle is modular which allows a great variety in their designing as well as their structural and functional properties. Typical examples discussed in this review are complexes of fluorinated surfactants. Thin and ultra-thin films of these polyelectrolyte–fluorosurfactant complexes form different smectic structures with low surface energies. The critical surface energies are in the range 6–18 mN/m. Optically functionalized complexes form rigid-rod, smectic A, B and turbostratic layered mesophases. Electroluminescent complexes with low turn-on points are described. It is reported that complexes of hexa-*peri*-hexabenzocoronene with polysiloxanes and poly(ethylene imine) form different columnar discotic structures with columns as long as 200 nm. These materials behave as viscoelastic solids. © 2002 Elsevier Science Ltd. All rights reserved.

Keywords: Polyelectrolyte–surfactant complexes; Small-angle X-ray scattering; Liquid crystal-like complexes; Self-assembly; Wetting; Fluorinated surfactants; Low surface energies; Light-emitting diodes; Discotic-columnar complexes; Hexa-*peri*-hexabenzocoronene; Nanoparticles; Nanodispersions; Poly(ethylene imine); Poly(*p*-phenyleneethynylene); Diazosulfonate polymers; Polysiloxanes

Contents

0079-6700/02/$ - see front matter © 2002 Elsevier Science Ltd. All rights reserved.
PII: S0079-6700(02)00017-5

1. Introduction

1.1. The scope of this review

The self-assembly of matter is manifest throughout biotic and abiotic nature. In scientific discourse, it is commonly accepted that self-assembly is the cornerstone of so-called ‘bottom-up’ synthetic routes to nano- and mesostructured materials [1]. The ‘bottom-up’ nanotechnologies are, however, competing with ‘top-down’ methods. In the latter, structures are carved or sculpted out of macroscopic materials, which are difficult and costly procedures. Experimental work on self-assembly is, therefore, a very active and scientifically rich field of inquiry.

In this review, the concept of self-assembly is applied in order to construct ordered arrays of organic molecules or, more generally speaking, to form periodic nanostructures. A typical periodicity is on a length scale of about 5 nm. For the construction of ordered organic molecules—periodic nanostructures—two basic building blocks are used: polyelectrolytes and ionic surfactants of opposite charges, defined as polyelectrolyte–surfactant complexes. The design and investigation of polyelectrolyte–surfactant complexes undertaken in this study is of an interdisciplinary nature. It lies on the border between polymer and colloid science, concerning issues that belong equally to the fields of physics and chemistry.

The formation of polyelectrolyte–surfactant complexes is modular and, accordingly, very comprehensive, as an immense number of building blocks are available. Polyelectrolytes as well as the surfactants used as building blocks, can be of either natural or synthetic origin. Polyethyleneimine, polyamino acids and DNA are examples of polyelectrolytes, while typical representatives of useful surfactants are carboxylic acids and lipids. For the purposes of this review, an effective criterion for the selection of building blocks and their combinations had to be created. Therefore, it was decided to accept only those combinations of building blocks that offer insight into the development of new materials. Highly ordered nanostructures are to be utilized in such a way that new materials will have, at least in theory, useful physical properties for everyday applications.

Section 1 of this review introduces the definitions of order and the methods of their measurement as far as they are used for the characterization of the polyelectrolyte–surfactant complexes presented here. Section 2 covers the self-assembly and the wetting of complexes containing fluorine and silicon moieties. It focuses on the formation of low surface energies. The optical properties of nanostructured complexes including their fluorescence and electroluminescene are presented in Section 3. Section 4 present columnar discotic complexes that are formed by complexes of hexa-peri-hexabenzocoronenes.

Diagrams illustrating the structures of chemical compounds are provided when it is unlikely that readers are familiar with their names. On the other hand, the derivations of formulae, the origins of which are readily available in the literature, have been omitted.

1.2. Definitions of order

In Section 1.1, the words ‘order’ and ‘self-assembly’ are used without any precise definition. Most definitions of order involve thermodynamic concepts. In this context, one might say that the most ordered state of a system is the one in which the system approaches as the temperature tends to zero. However, this definition would be of little service in the context of polyelectrolyte–surfactant complexes. Many of the complexes discussed here, either as a powder or as films, are in states of metastable equilibrium which are likely to survive longer periods than the time taken to carry out experiments. Typically, these periods are as long as 4 weeks and in some cases years. Therefore, a different definition of order is used in this review, one which can also be found in the description of order in thin organic films as shown by Tredgold [2]. From a practical point of view, the extent to which disorder can be tolerated depends widely on the context. In a system like DNA encoding the structure of a particular enzyme, a single defect may render the entire system useless. By contrast, a nematic liquid crystal display may perform its function well if the axis of each molecule in a particular region lies at an angle not too far removed from that of the director, even when no other order exists.

In solid-state physics, a perfect, single crystal is usually considered as the ideal, ordered system. In

practice, however, typical crystals contain dislocations and localized lattice defects. In the materials formed by polyelectrolyte–surfactant complexes, the degree of perfection of typical crystals is not achieved. Most of these complexes are really best described as frozen liquid crystals. For this reason the nomenclature of liquid crystals is used for the description of the self-assembled nanostructures of polyelectrolyte–surfactant complexes.

1.3. Methods of measuring the degree of order

A discussion of the concept of order is related to the description of the various experimental techniques used to measure this in polyelectrolyte–surfactant complexes. The list given below includes the techniques which have been employed in this review.

1. The most important is X-ray diffraction in the small-angle mode for the determination of order at length scales in the range 1–100 nm. Two types of system are used: pinhole cameras and a Kratky camera.
2. X-ray diffraction in the wide-angle mode is used to determine the degree of order on an atomic length scale, i.e. smaller than 1 nm. Examples are the side-chain crystallinity of the tail of alkyl chains of surfactants within the polyelectrolyte–surfactant structures.
3. Optical polarization microscopy is a method used to obtain information quickly about optical anisotropy of films of complexes and about liquid crystalline-like structures.
4. Electron microscopy is useful to supplement the information of the small-angle X-ray scattering about periodic nanostructures in the complexes as bulk material. Furthermore, it is a method for the investigation of nanoparticles of the complexes, especially in types of core–shell morphology.
5. Atomic force microscopy (AFM) is suitable for creating images of the surfaces of complexes deposited as thin films and of nanoparticles that have been settled on a solid substrate. This method is successfully used in order to visualize terraced structures of the surfaces of films and their dewetting. It is further used to characterize nanoparticles of different morphology such as compact, core–shell and doughnut shape.
6. Infrared, UV–Vis and fluorescence spectroscopies are techniques for the investigation of the degree of complexation and the optical properties of polyelectrolyte–surfactant complexes.

1.4. X-ray diffraction

The scattering intensities are given as a function of the scattering vector which is defined here as $s = q/2\pi = 2/\lambda \sin\theta$, where θ is the Bragg angle and λ is the wavelength of the X-ray radiation (0.154 nm).

1.4.1. Kratky camera

It is well known that the maximum position of a small-angle scattering peak, using a Kratky camera, is different from that found using a pinhole system. In general, it can be observed that the peak position determined by using a pinhole system is located between the maximum of the Kratky peak and its point of inflection. Two possibilities exist for the determination of the correct peak position of a Kratky peak. The first is a desmearing of the scattering curve. The second is to fit a length-smeared peak onto a Kratky peak. The solution for the latter has been given by Ruland [3]. In this work length-smeared Lorentzian

peaks are used. Here, they correspond better with the experimental data than Gaussian peaks. The spherical average $\langle\ \rangle_\omega$ of a three-dimensional Lorentzian distribution $I_{L3}(s)$ with the integral width b and the distance s_h from the origin of the reciprocal space is given by $I_L(s) = \pi b/(b^2 + \pi^2(s - s_h)^2)^2$. A length slit smearing of this function, with the approximation of an infinite length of the slit, produces

$$J(s) = \frac{1}{2s_h}\left(\frac{(A^2 + B^2)^{1/2} - A}{2(A^2 + B^2)}\right) \tag{1.1}$$

in which $A = b^2 + \pi^2(s^2 - {s_h}^2)$ and $B = 2\pi b s_h$. J represents the slit-smeared intensity and s_h is the reflex position without slit-smearing effects. This expression can be fitted easily to peaks measured with a Kratky camera and produces a good determination of peak positions and width when compared to measurements carried out with a high-resolution pinhole small-angle X-ray camera.

1.4.2. Nanostructures with sharp interfaces

The nanostructures of periodic or non-periodic microphase-separated systems normally show density transitions at interfaces that separate the different phases. In the ideal case, the density transitions between these regions are sharp. Examples are strongly segregated block copolymers and numerous polyelectrolyte–surfactant complexes. Sharp phase boundaries are identified in the small-angle scattering by the presence of Porod's law [4] which is given by

$$\lim_{s\to\infty} 2\pi^3 s^4 I(s) = \frac{k}{l_p}, \tag{1.2}$$

I is the scattering intensity when measured with a pinhole system, l_p is the average cord length, and k is the invariant, which is given by the expression

$$k = 4\pi \int_0^\infty s^2 I(s)\, \mathrm{d}s. \tag{1.3}$$

The scattering intensity is experimentally available between a lower limiting value of the scattering vector s_{min} and an upper value s_{max}. In order to calculate the invariant as precisely as possible, the experimental limits are taken into account by approximations of the region of high and low scattering vectors, which results in

$$k = \frac{4}{3}\pi {s_{min}}^3 I(s_{min}) + 4\pi \int_{s_{min}}^{s_{max}} s^2 I(s)\, \mathrm{d}s + \frac{4\pi}{s_{max}} \lim_{s\to\infty} [s^4 I(s)]. \tag{1.4}$$

A similar approximation for measurements performed with a Kratky camera was used earlier by Ruland [5]. Typically the first and third term in Eq. (1.4) represents less than 10% of the invariant. When using a Kratky camera, Porod's law is modified due to its length smearing effect, which results in

$$\lim_{s\to\infty} 4\pi^2 s^3 J(s) = \frac{k}{l_p}, \tag{1.5}$$

where k is given by the expression

$$k = 2\pi \int_0^\infty sJ(s)\, \mathrm{d}s. \tag{1.6}$$

Again in order to calculate the invariant as precisely as possible the experimental limits are taken into account by approximations of the region of high and low scattering vectors, which results in

$$k = \pi {s_{\min}}^2 J(s_{\min}) + 2\pi \int_{s_{\min}}^{s_{\max}} sJ(s)\,\mathrm{d}s + \frac{2\pi}{s_{\max}} \lim_{s\to\infty} [s^3 I(s)]. \tag{1.7}$$

The main source of error in the range of validity covered by Porod's law is the scattering due to density fluctuations and the widths of the domain boundary [6]. Broader transitions or a statistical structuring of the domain boundary, as typically observed in microphase-separated block copolymers change the scaling of $I(s) \propto s^{-4}$ when using a pinhole camera system or the scaling of $J(s) \propto s^{-3}$ when using a Kratky camera. Small deviations from a sharp boundary would indicate a significant deviation from Porod's law [6]. A linear behavior of a scattering curve in a $s^4 I(s)$–s^4 plot of a pinhole camera measurement or in a $s^3 J(s)$–s^3 plot of a Kratky camera measurement proves that the only deviation from Porod's law is a three-dimensional homogeneous density fluctuation. The latter is given as the slope of a straight line in the curve. Then a broader transition or a statistical structuring of the domain boundary, as typically observed in microphase-separated block copolymers [7], can be excluded. If Porod's law is strictly fulfilled the phase boundaries of the nanostructures are in the order of 1–2 atomic distances.

1.4.3. Lamellar nanostructures in the bulk material

An ideal lamellar nanostructure is here considered to be a two-phase system with sharp boundaries and planar interfaces. The scattering of such a structure is determined by the statistics of the thicknesses of the lamellae as well as the finite size of the stacks of the lamellae. If the evaluation of the small-angle scattering is limited to the angular range of the first-order maximum, the separation of these effects is not possible. The wider the angular range, and the more precise the measurements at higher angles, the more detailed and reliable are the results of the evaluation. The simplest lamellar nanostructure of a polyelectrolyte–surfactant complex is a microphase-separated model consisting of an ionic phase and a non-ionic phase. The ionic phase contains the polyelectrolyte chains and the ionic head groups of the surfactants, where the non-ionic phase contains the hydrophobic moieties such as alkyl chains. The repeat unit of a lamellar system d is given by $d = d_1 + d_2$, where d_1 and d_2 are the thicknesses of the two lamellae. Their values can be determined by calculating the interface distribution function $g(r)$ [8], which is defined as the second derivative of a one-dimensional autocorrelation function for positive definite values of the distance r in real space. The interface distribution function can be computed by a combination of the inverse Fourier transformation and the slit-length desmearing, given by the expression

$$g(r) \propto \int_0^\infty G(s)\left(4J_0(2\pi rs) - \frac{1 - 4\pi^2 r^2 s^2}{\pi rs} J_1(2\pi rs)\right) \mathrm{d}s, \tag{1.8}$$

where J_n is the Bessel function of the first kind and the nth order, and $G(s)$ is the interference function defined by

$$G(s) \propto \left[\lim_{s\to\infty} s^3 J(s)\right] - s^3 J(s). \tag{1.9}$$

The interface distribution function can be written in the form

$$g(r) \propto h_1 + h_2 - 2h_{12} + h_{121} + h_{212} - 2h_{1212} + \cdots, \tag{1.10}$$

where h_i represents the normalized distributions of the distances between interfaces, measured at a perpendicular to the planes of the lamellae. A model that can describe the statistics of lamellar phases is the lattice model, in which the statistics are given by the distributions $h_1(d_1)$ and $h_d(d)$ of the lamellar thicknesses [7].

If the interfaces of the lamellae are completely planar, and the lateral dimensions are large compared to the thicknesses of the lamellae, the total interface area per volume is given by $S_0/V = 2/d$. But, if the interface is not planar, the total interface area S obtained from l_p is larger than S_0 obtained from d. A measure of the planarity of the interfaces is obtained from the ratio

$$\frac{S}{S_0} = \frac{2d_1d_2}{dl_p}. \tag{1.11}$$

Obviously S/S_0 is 1 for planar interfaces and becomes larger than 1 for undulated or wavy interfaces. The thicknesses d_1 and d_2 can be calculated by using the interface distribution function of Eq. (1.10) but, if planar interfaces are present, then the thicknesses can also be calculated [7]. This can be done by the relationships

$$d_1 = \frac{d}{2}\left(1 - \sqrt{1 - \frac{2l_p}{d}}\right) \quad \text{and} \quad d_2 = d - d_1. \tag{1.12}$$

1.4.4. Finite lamellar structures of nanoparticles

The X-ray scattering intensities for spheres with an internal lamellar structure used to discriminate between different mesomorphous structured nanoparticles have been discussed [25]. In particular, indicators which distinguish an onion-type structure of concentric lamellae (Fig. 1(A)) from a structure of parallel layers (Fig. 1(B)) are of interest. This object is called a tart-type particle. Other structures may be constructed by the superposition of these limiting cases, which then will look more like a 'patch-work'.

The scattering amplitude of the onion-type is given by

$$A(s) = \frac{3}{(2\pi Rs)}\sum(\Phi(2\pi r_j s) - \Phi(2\pi r_{j-1}s))\rho_j \tag{1.13}$$

with

$\Phi(x) = \sin(x) - x\cos(x)$.

The onion is assumed to be a sphere of diameter $D = 2R$ with layer boundaries at $0 = r_0 < r_1 < r_2 < \cdots < r_n = R$ and layer densities $\rho_1, \ldots, \rho_n$. The amplitude is normalized such that $A(0) = 1$ for a sphere of constant unit density $\rho_1 = \rho_2 = \cdots = \rho_n = 1$. The corresponding intensity is given as $I(s) = |A(s)|^2$. The scattering amplitude of the tarts, i.e. spheres with an internal structure of parallel lamellae (Fig. 1(B)) is given by the following Fourier integral:

$$A(s,\vartheta) = \frac{1}{R^3}\int_{-R}^{R} \mathrm{d}z\rho(z)\int_{-r(z)}^{r(z)} \mathrm{d}r'\int_0^{2\pi} \mathrm{d}\phi \exp \mathrm{i}(2\pi srz\cos\vartheta + 2\pi sr'\sin\vartheta\cos\phi)$$

$$= \frac{1}{R^3}\int_{-R}^{R} \mathrm{d}z\rho(z)\frac{r(z)}{2\pi s\sin\vartheta}J_1(2\pi sr(z)\sin\vartheta)\exp(\mathrm{i}2\pi sz\cos\vartheta). \tag{1.14}$$

Here, the ϕ and r' integrations are reduced to the Bessel function $J_1(x)$. The sphere has a diameter of $D = 2R$ with layer boundaries at $-R = z_0 < z_2 < \cdots < z_n = R$ and layer densities $\rho_1, \ldots, \rho_n$. The

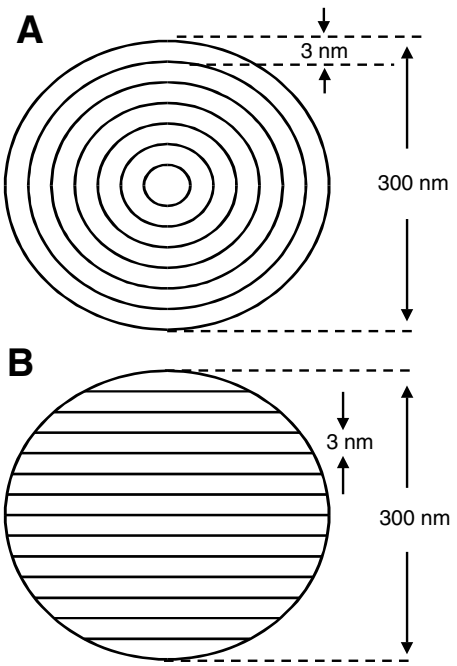

Fig. 1. Idealized models for the finite lamellar structures of nanoparticles are the onion-like (A) and the tart-like structures (B). The size of the particles is about 300 nm whereas the internal lamellar structure has a unit cell dimension of about 3 nm. Reprinted with permission from Langmuir 2000;16:850 © American Chemical Society [25].

scattering intensity results from an integration over all orientations of these tart-type particles:

$$I(s) = \frac{1}{2}\int_0^{\pi} \mathrm{d}\vartheta \sin\vartheta |A(s,\vartheta)|^2. \tag{1.15}$$

To produce results that allow for a comparison of the two limiting internal structures for a lamellar sphere, the intensities for model systems using realistic data are taken. The two parameters that are taken where the ratio of the two densities $\rho^{(1)}/\rho^{(2)}$ and the ratio of the thickness d_1 of the first part of the double layer to its total thickness $d = d_1 + d_2$. The parameter d_1 is interpreted here as the thickness of the non-ionic rich phase, and d_2 as the thickness of the ionic, that is the polyelectrolyte-rich phase. Two complexes 'C1' and 'C2' with differing parameter values are considered. For the complex C1, the densities are $\rho^{(1)}/\rho^{(2)} = 0.9/1.1$, and for the layer thickness they are $d_1/d = 1.80/3.00$. For the other complex, C2, values are 0.9/1.1 and 2.07/3.00, respectively. Fig. 2 shows the logarithmic intensities for complex C1 in simultaneous plots for the onion- and tart-type structures. The main peaks in intensity correspond to integer values of $m = sd$. For C1 the peak at $m = 5$ is missing. The reason is that here $d_1/d = 3/5$ and cancellation takes place in both sublayers individually for $m = 5$. The fine structure of the curves can be shown to result from the overall dimensions of the spheres, i.e. from integer values of sD. Obviously this fine structure is a lot more pronounced in the case of the spherically symmetric onion structure. This difference results from the spherical symmetry and the uniform boundaries of the onion and, in principle, makes it possible to distinguish onion- and tart-type structures by small-angle X-ray scattering experiments. Note that in the logarithmic plot values close to zero also become pronounced.

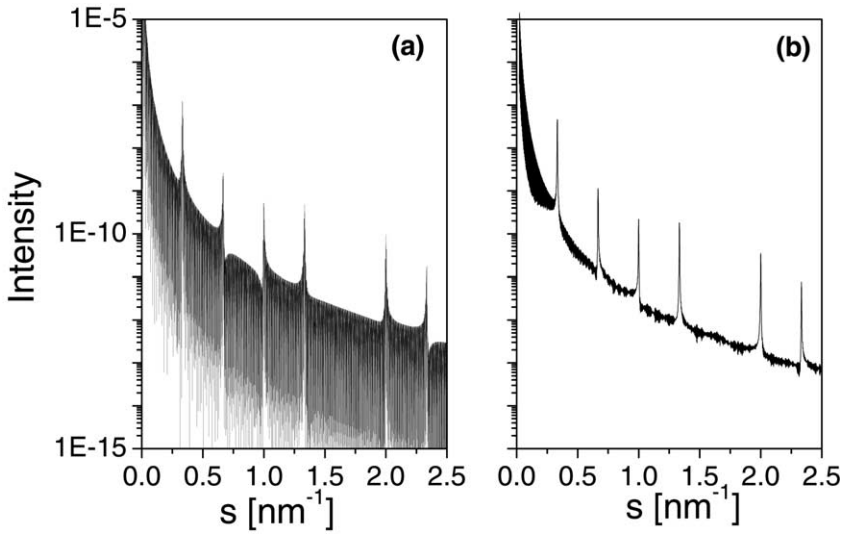

Fig. 2. Theoretical scattering curves of lamellar nanoparticles with an onion-type structure (a) and a tart-type structure (b). The lamellar unit cell dimension is $d = 3.00$ nm, $d_1 = 1.80$ nm. The densities are $\rho_1 = 0.9$ and $\rho_2 = 1.1$. The size of the particle is 100 $d = 300$ nm. The density of the surroundings is 1. Reprinted with permission from Langmuir 2000;16:850 © American Chemical Society [25].

No significance can be given to the amplitudes of these downward 'peaks', because they have an artificial distribution due to the numerical cut-off.

To study the difference of the two internal structures in more detail, the intensities near the first peak at $s = 1/d$ in linear plots are given in Fig. 3.

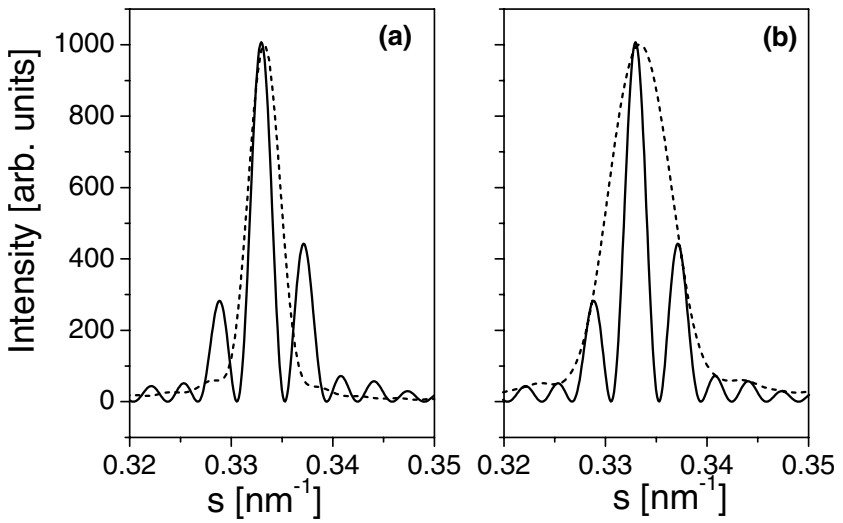

Fig. 3. Scattering in the region of the first Bragg reflection. The scattering of the onion-type particle is characterized by a number of additional maxima (diagram a, solid line). By contrast, no additional maxima are present in the scattering of the tart-type particle (diagram a, dashed line). A polydispersity of 1% smears out the additional maxima (b, dashed line) which are present in the scattering of the same but monodisperse onion-type particles (b, solid line). The particle parameters are $d = 3.00$ nm, $d_1 = 1.80$ nm, $\rho_1 = 0.9$, $\rho_2 = 1.1$ and $D = 100d$. Reprinted with permission from Langmuir 2000;16:850 © American Chemical Society [25].

In addition it is considered as to whether the apparent difference in the signal could indeed be detected in a realistic experiment. To this end a polydispersity is assumed for the diameter D of the 'onions' to a value of 1%. In the model this means a deviation of up to ± 1 layer. The scattering intensity of such a polydisperse sample is calculated by averaging over intensities I_D for onions with diameter D in the range $D_0 \pm 1\%$ assuming a uniform distribution for D. An onion for which the diameter D is not an integer multiple of the layer thickness d is allowed to have a core layer that is smaller than d. The intensity resulting from this average is plotted together with the original curves in Fig. 3. Obviously polydispersity smears out the fine structure of the onion-type signal, but a slight yet significant difference to the tart-type signal remains. From the width of the Bragg reflection, a correlation length of about the size of the particle (300 nm) is determined. This is an order of magnitude larger than those observed experimentally. It must be stated that currently the polydispersity ($>10\%$) of the nanoparticles of the polyelectrolyte–surfactant complexes is too large to permit detailed information by small-angle X-ray scattering to be obtained.

It is easier to detect the onion-type scattering experimentally when the particle sizes are smaller. In these cases, the distance between the minima next to the Bragg peak (Fig. 3) increases. This is clearly shown in Fig. 4. The influence of the polydispersity on the scattering curve is considerable. It seems to be realistic to think that it is possible to detect onion-type structures experimentally if the number of double layers is not greater than 20 and the polydispersity is lower than 5%.

2. Self-assembly and wetting

2.1. Complexes of polyelectrolytes and fluorinated surfactants (PEFAs)

The systematic preparation of low energy surfaces prepared by the self-assembly of PEFA complexes

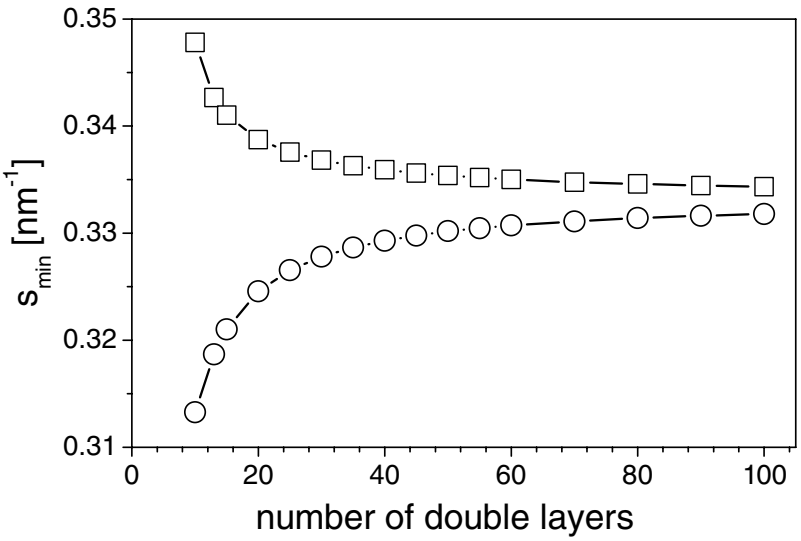

Fig. 4. The positions of the two minima next to the first Bragg reflection. The particle parameters are $d = 3.00$ nm, $d_1 = 1.80$ nm, $\rho_1 = 0.9$, $\rho_2 = 1.1$ and $D =$ (number of layers)d. Reprinted with permission from Langmuir 2000;16:850 © American Chemical Society [25].

is potentially of high technological importance as well of fundamental scientific interest. There are a variety of possible applications for these new materials as coatings. Due to their easy preparation, such coatings are very promising, for example, as easy-to-clean surfaces such as thin protective coatings for walls which are prone to contamination (graffiti), coatings for sport equipment (as a colloidal substitution of ski wax) or as anti-soiling coatings for textiles. PEFA materials are the fluoro-containing mirror image of non-fluorinated solid polyelectrolyte–surfactant complexes (PE-surfs), which have been reviewed recently [9–11,152]. The various properties of PEFAs and non-fluorinated PE-surfs are comparable to those of the classical polymers PTFE and polyethylene. A common property of PEFA and PE-surfs is a pronounced tendency to form well-ordered liquid crystalline-like structures with a high mechanical and thermal stability. The main difference is in their wetting behavior: PEFA form highly oleophobic, while PE-surfs form oleophilic surfaces.

This section is divided in the following way: In Section 2.1.1, the general principle of the complex formation is introduced. Sections 2.1.2 and 2.1.3 show the variability of lamellar nanostructures formed when the surfactant and the charge density are varied. Coatings from nanoparticles of complexes are presented in Section 2.1.4. This is followed by Section 2.1.5, which focus on the surface structure. Columnar discotic complexes of PEFAs are the subjects of Section 2.1.6. A description of ultra-thin films of a PEFA is given in Section 2.1.7, followed by Section 2.1.8 on the fine-tuning of the surface energy by varying the length of the fluorinated groups. Diazosulfonate polymer complexes form the content of Section 2.2. Then in Section 2.3 an investigation of polyelectrolyte–silicon–surfactant complexes is given, and finally polysiloxane–fluorosurfactant complexes are dealt in Section 2.4.

2.1.1. Complex formation

Recently, the solid-state structures of PEFA materials, which are first presented in 1996 [12], have become a focus of interest. The preparations of these complexes are carried out by common precipitation from aqueous solution. As a result of a cooperative zipper mechanism between a polyelectrolyte and oppositely charged surfactants, a 1:1 stoichiometry can be achieved [13–15].

The complexation of a single chain is schematically shown in Fig. 5(a). It can be seen that two building blocks are used normally to form a nanostructured polymeric material. The predominant phase morphology of the bulk materials is the lamellar architecture which looks, in ideal cases, like the sketch in Fig. 5(b). Fluorinated lamellar sheets (dark shaded) alternate with ionic sheets in a super-strongly segregated arrangement similar to block copolymers in the super-strongly segregation regime [16]. The molecular arrangement at the PEFA/air interface is characterized by an enrichment of CF_3-groups, which are responsible for the low surface energies of these types of complexes (Fig. 5(c)). In well-aligned structures the first ionic layer lies parallel to the CF_3-group layer at a distance of 1–2 nm from the surface layer.

Typical building blocks which are useful for the formation of PEFA complexes are shown in Fig. 6 The polymers p, the first building blocks, are homopolymers and copolymers of diallyldimethylammonium chloride such as poly[(diallyldimethylammonium chloride)-*co*-(*N*-methyl-*N*-vinylacetamide)] (p_1) or commercial polymers such as poly[(acrylamidopropyl)trimethylammonium chloride] (p_2) and polyethyleneimine (p_3). Examples of fluorinated surfactants a, which compose the second building blocks, are perfluorinated carboxylates (a_1), fluorinated sulfonates (a_2), sodium [bis(perfluorohexylethyl)-2-sulfosuccinate] (Fluowet SB, a_3) and fluorinated phosphates such as Zonyl FSE (a_4). The possibilities of modifying the solid-state structures and the surface properties by varying each of the building blocks are manifold.

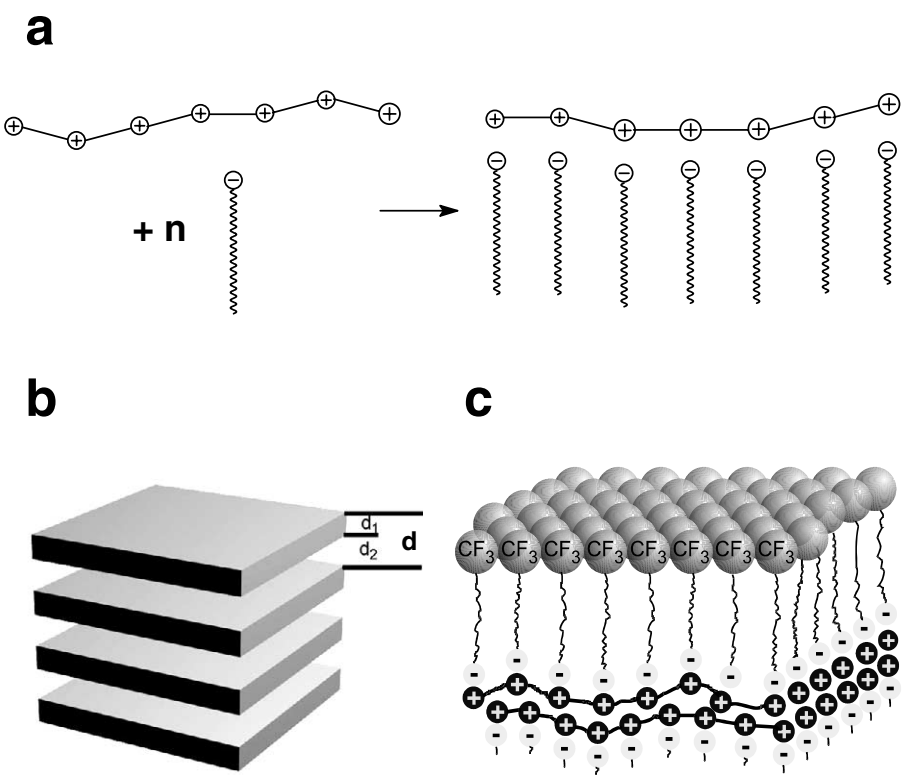

Fig. 5. (a) The formation of a PEFA complex by a cooperative zipper mechanism between a polyelectrolyte chain and oppositely charged fluorinated surfactant molecules. (b) An idealized lamellar mesomorphous complex structure with a repeat unit length of d consisting of fluoroalkyl-containing sheets with a thickness of d_1 (dark shaded) and ionic sheets containing polyelectrolytes with a thickness of d_2 (not shown). This multi-lamellar structure is typical of many fluorinated PEFA materials. (c) The molecular arrangement at the interface complex to air is dominated by the enrichment of CF_3-groups. The surfactants are strongly linked to the polyelectrolyte chains which lie about 1 nm beyond the CF_3-layer. Reprinted with permission from Polymer International 2000;49:636 © Society of Chemical Industry [17].

2.1.2. Variation of the surfactant [17]

Examples of the possibility of altering the complex properties by the surfactants are the complexes poly(diallyldimethylammonium)-Fluowet SB (p_1-a_3) and poly(diallyldimethylammonium)-Zonyl FSE (p_1-a_4) [18]. The polyelectrolyte had a molecular weight of $M_n \approx 190000$ g/mol and $M_w \approx 500000$ g/mol as determined by GPC. The differences of the solid-state structures of both complexes are determined by scattering and visualizing methods. In the small-angle region of the X-ray diagram of p_1-a_3 three equidistant reflections are present (Fig. 7(a)). This finding is consistent with a lamellar bulk structure such as shown in Fig. 5(b). From the reflex positions, the repeat unit has been determined to be 3.13 nm. Information about the order of the atomic length scale has been established by wide-angle X-ray scattering (Fig. 7(b)). In addition to the fourth-order reflection of the lamellar system, only two broad reflections at about 2 and 4 nm^{-1} have been found; the latter is due to uncorrelated positions of the fluorinated segments. The absence of sharp reflections proves that no crystalline regions are present within the complex. The lamellar structure has been confirmed by electron microscopy and AFM of p_1-a_3 freeze-fractured complex films (Fig. 8(a) and (b)). The structure of p_1-a_4 varies from that of p_1-a_3.

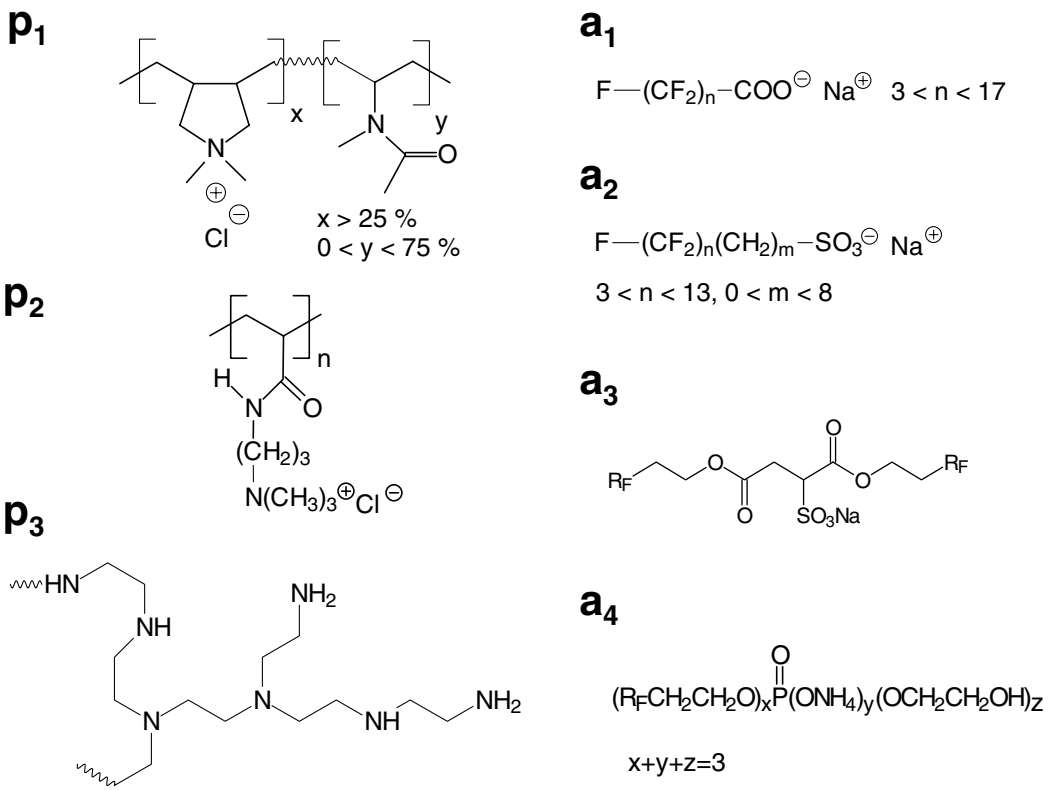

Fig. 6. Typical building blocks which are useful for the formation of PEFA materials. The polyelectrolytes are poly[(diallyldimethylammonium chloride)-*co*-(*N*-methyl-*N*-vinylacetamide)] (p_1), poly[(acrylamidopropyl)trimethylammonium chloride] (p_2) and polyethyleneimine (p_3). Examples of fluorinated surfactants are perfluorinated carboxylates (a_1), fluorinated sulfonates (a_2), sodium [bis(perfluorohexylethyl)-2-sulfosuccinate] (Fluowet SB, a_3) and fluorinated phosphates such as Zonyl FSE (a_4). Reprinted with permission from Polymer International 2000;49:636 © Society of Chemical Industry [17].

As can be seen in the small-angle X-ray diagram of p_1–a_4 two broad reflections are present with relatively positions of $1:1^{1/3}$ in addition to three sharp equidistant reflections (Fig. 9(a)). This scattering pattern can be explained by a perforated lamellar structure with a good ordering of the lamellar stacks with a repeat unit of 4.36 nm. The perforations within the ionic layers are hexagonally ordered with an in-plane center-to-center distance of about 3.7 nm. In the wide-angle region of complex p_1–a_4 (Fig. 9(b)), a relative sharp reflection at $s = 1.95\ \mathrm{nm}^{-1}$ is present. This is consistent with a parallel packing of fluorinated chains in such a way that their main axes have positions which correlate with a chain-to-chain distance of 0.59 nm. The CF_2-segments of the adjacent chains do not show a positional correlation. The perforated lamellar structure of p_1–a_4 is determined by freeze-fracture electron microscopy. This is shown in Fig. 10(a) and a model of a polyelectrolyte containing layer is shown in Fig. 10(b). Using the termini of liquid crystals, the structure of p_1–a_3 is smectic A-like and that of p_1–a_4 is smectic F-like. In contrast to thermotropic liquid crystals only glass-transitions are found at 8 °C (p_1–a_3) and at −38 °C (p_1–a_4); this has been done by using differential scanning calorimetry (DSC). No other phase transitions are detected up to the decomposition of the complexes, which occur at temperatures higher than 200 °C.

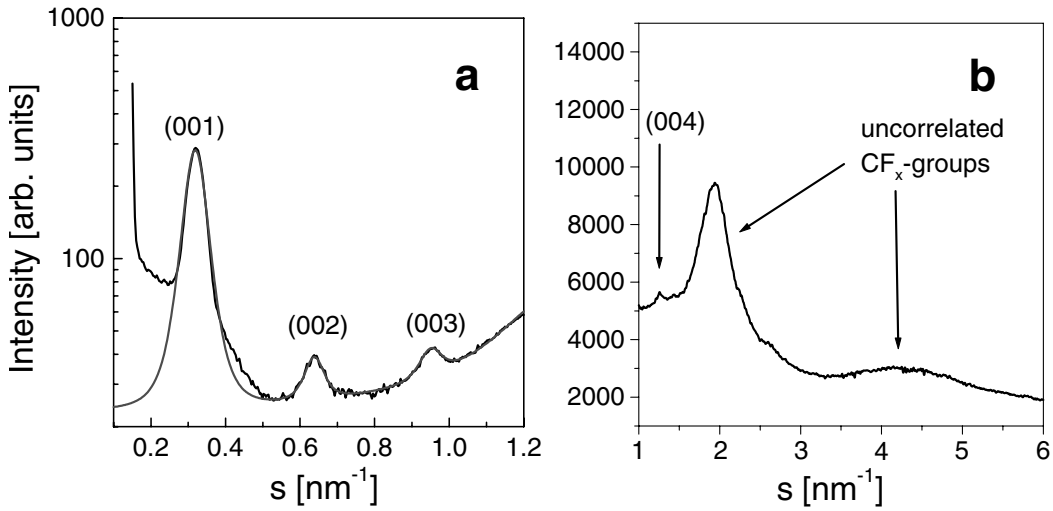

Fig. 7. X-ray scattering curves of a lamellar complex formed by poly(diallyldimethylammonium chloride) homopolymer (molecular structure p_1) and Fluowet SB (molecular structure a_3). In the small-angle region three equidistant reflections are present (a). To determine the structure parameters Lorentzian profiles are fitted to the scattering curve (lower curve). The Miller indices are (001), (002) and (003). In the wide-angle region the (004) reflection of the lamellar system and two broad reflection are present (b). Reprinted with permission from Polymer International 2000;49:636 © Society of Chemical Industry [17].

The differences of p_1-a_3 and p_1-a_4 in their structures and in their glass-transitions temperatures is reflected macroscopically by a higher mechanical strength σ and a higher Young's modulus E of p_1-a_3-films. σ and E are determined by stress–strain experiments. Typical curves are shown in Fig. 11(a) and (b). Films of p_1-a_3 with thicknesses in the range 0.1–1 mm have a Young's modulus of

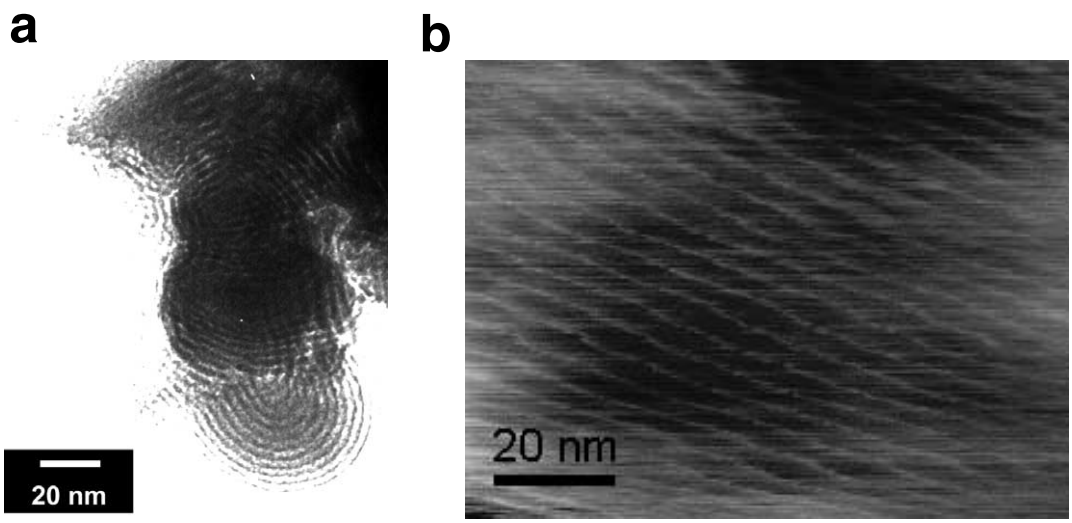

Fig. 8. Visualizing method results of the poly(diallyldimethylammonium) Fluowet SB structure: (a) electron microscopy of a fractured complex film and (b) AFM of a film edge. The lamellae are oriented perpendicular to the measured plane. The bright stripes are due to the ionic sheets, the dark ones are due to the fluorinated sheets. Reprinted with permission from Polymer International 2000;49:636 © Society of Chemical Industry [17].

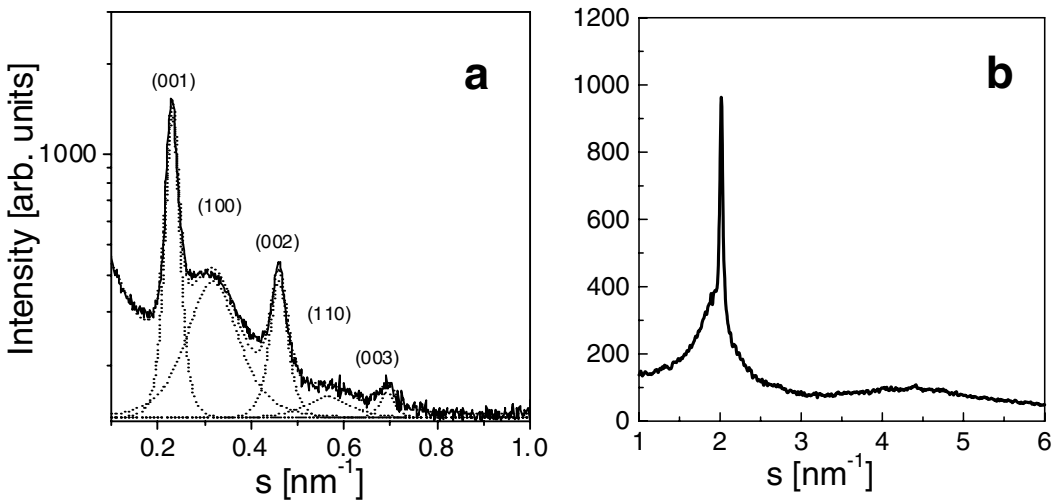

Fig. 9. X-ray scattering curves of a lamellar complex formed by poly(diallyldimethylammonium chloride) homopolymer (molecular structure p_1) and Zonyl FSE (molecular structure a_4). In the small-angle region three small equidistant reflections and two broader reflection with relative position of $1:3^{1/2}$ are present (a). This is consistent with the scattering of a perforated lamellar structure with a hexagonal order of the perforations in the plane and no correlation of the perforations of adjacent layers. For determination of the structure parameters Lorentzian profiles are fitted to the scattering curve. For clarity the Lorentzian profiles are plotted (dashed curves). Miller indices are (001), (100), (002), (110) and (003). In the wide-angle region one sharp and two broad reflection are present (b). The former results from a parallel alignment of rod-like perfluorinated segments. Reprinted with permission from Polymer International 2000;49:636 © Society of Chemical Industry [17].

5000–6000 MPa and a strength of about 70 MPa. By contrast films of p_1-a_4 have only a modulus of 400–500 MPa and a strength of 4 MPa. It is probable that the differences in the mechanical properties of p_1-a_3 and p_1-a_4-films are due to the differences of the polyelectrolyte layer structures. The modulus and the strength of the non-disturbed layer structure are higher than that of the perforated layer structure. Contact angles of drops of hexadecane on film surfaces are as high as 74° (for p_1-a_3) and 70° (for p_1-a_4). These indicate low surface energies for both complexes, which are calculated to be about 14 mJ/m^2 (p_1-a_3) and 12 mJ/m^2 (p_1-a_4); this has been done using the procedure described by Neumann and Li [19,20].

2.1.3. Variations in the charge density [21]

A fine tuning of the PEFA structure can be carried out easily by reduction of the charge density of the polyelectrolyte. This has been demonstrated for complexes of poly[(diallyldimethylammonium chloride)-*co*-(*N*-methyl-*N*-vinylacetamide)] (p_1) and perfluorodecanoic acid (a_1). The amount of charged monomers of p_1-a_1 complexes are in the range from 25 to 100 mol%. No stoichiometric solid-state complexes are obtained below a content of 25 mol% charged monomers.

The nanostructure of p_1-a_1 complexes is that of a perforated lamellar structure with a pseudo-cubic or tetragonal ordering of the perforations. For clarity the structure of the polyelectrolyte layers is shown in Fig. 12. The unit cell volume decreases with increasing charge density from 101 nm^3 (25 mol% cationic charges) to 49 nm^3 (100 mol%). This is shown in Fig. 13. The reduction of the unit cell volume corresponds to an increase in the perforation density within the polyelectrolyte-rich layers. This enhances the curvature of the interfaces between the ionic and fluorinated layers.

Macroscopically it is found that the densities of the complexes increases with an increase of the

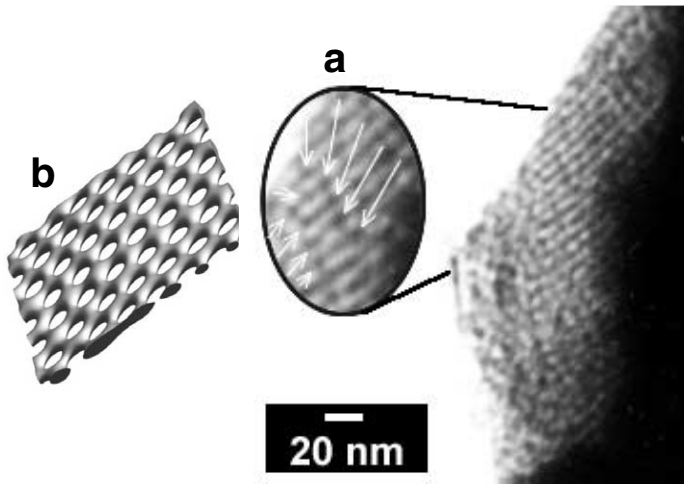

Fig. 10. TEM picture of a perforated lamellar structure of a poly(diallyldimethylammonium)-Zonyl FSE complex (a). Some perforations are indicated by arrows. The molecular structures of the building blocks are shown in Fig. 6 (p_1 and a_4). (b) Shows a simulated model of one perforated polyelectrolyte layer. Reprinted with permission from Polymer International 2000;49:636 © Society of Chemical Industry [17].

charge density from 1.44 g/cm^3 (25 mol% cationic monomers) to 1.87 g/cm^3 (100 mol%, Fig. 13). The increase of the density in the solid state is accompanied by an increase of the molecular order. This has been determined by wide-angle X-ray measurements. Only broad reflections are present in the wide-angle X-ray scattering diagrams of p_1-a_1 complexes with 25, 47 and 65 mol% cationic monomers (Fig. 14), indicating that there is no order on an atomic length scale. The degree of the molecular order of a p_1-a_1 complex with a charge density of 87 mol% is similar to that of p_1-a_4, i.e. a parallel alignment of

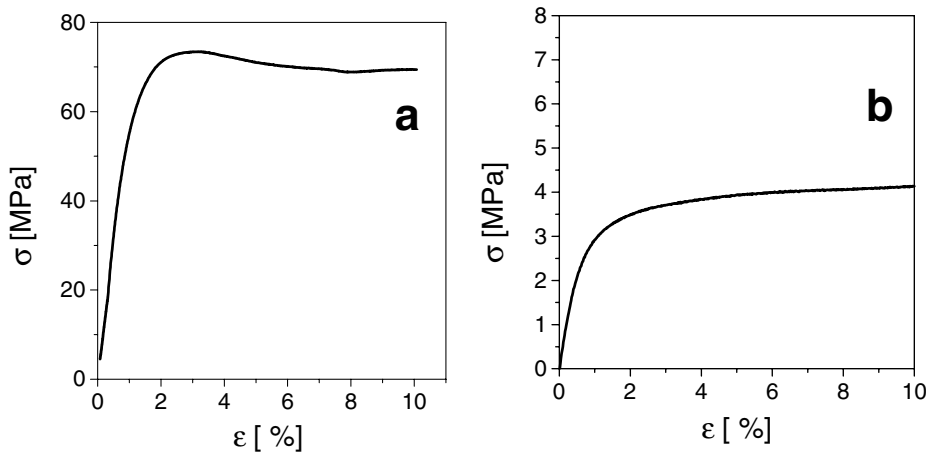

Fig. 11. Stress–strain diagrams of complex films: (a) is poly(diallyldimethylammonium) Fluowet SB which has an *E*-modulus of 5600 MPa, a glass transition at 301 K and a non-disturbed lamellar structure with a repeat unit of 3.22 nm. (b) is poly(diallyldimethylammonium) Zonyl FSE which has an *E*-modulus of 400 MPa, a glass transition at 236 K and a hexagonal perforated lamellar structure with a repeat unit of 4.38 nm. Reprinted with permission from Polymer International 2000;49:636 © Society of Chemical Industry [17].

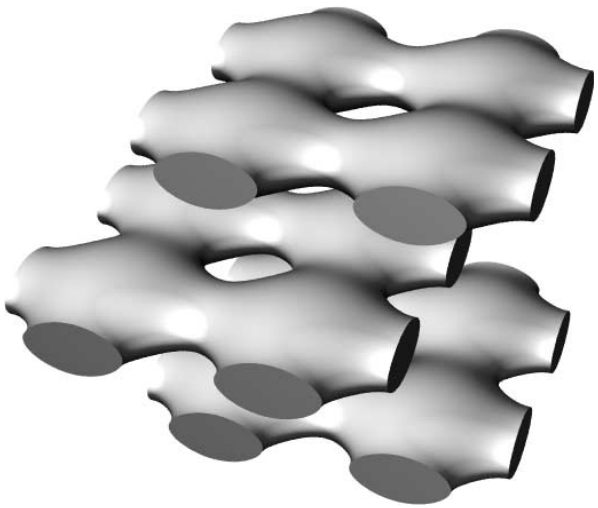

Fig. 12. A model of the tetragonal perforated lamellar layer structure of poly[(diallyldimethylammonium)-*co*-(*N*-methyl-*N*-vinylacetamide)] perfluorodecanoate. Within this structure, the polyelectrolyte phase is plotted in gray. The surfactant molecules fill the interlayer space. Reprinted with permission from Langmuir 1998;14:4901 © American Chemical Society[21].

fluorinated chains. A typical pattern of a side-chain crystalline-like ordered structure is found for p_1-a_1 with 100 mol% cationic groups, which crystallize from solution as sharp elongated needles. The wetting behavior of all p_1-a_1 complex films, even with different charge densities, is very similar. The contact angles of hexadecane are between 71 and 79°.

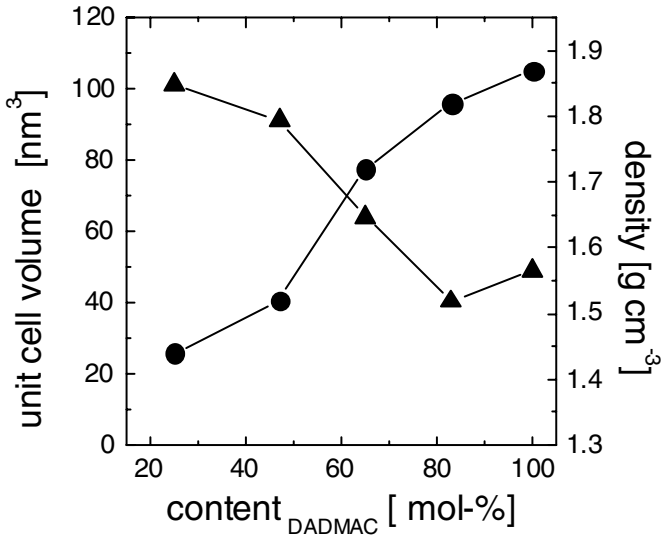

Fig. 13. The unit cell volume of the tetragonal supramolecular structure of poly[(diallyldimethylammonium)-*co*-(*N*-methyl-*N*-vinylacetamide)] perfluorodecanoate complexes (triangles) and the density (circles) of the complexes depending on the content of diallyldimethylammonium groups. The diallyldimethylammonium content is given in mol% of the copolymer composition. Reprinted with permission from Langmuir 1998;14:4902 © American Chemical Society[21].

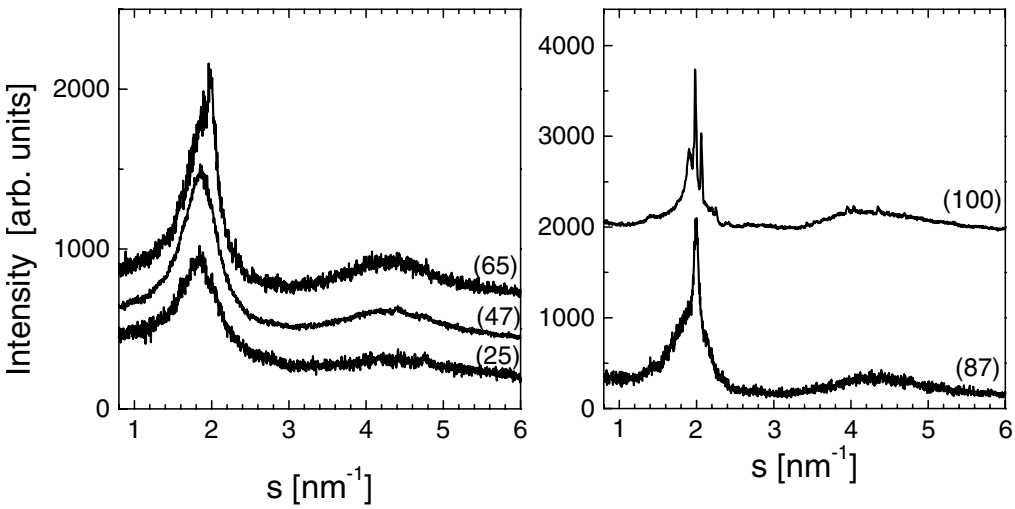

Fig. 14. Wide-angle X-ray scattering diagrams of poly[(diallyldimethylammonium)-*co*-(*N*-methyl-*N*-vinylacetamide)] perfluorodecanoate complexes. The content of cationic monomers is given in brackets. The molecular order increases successively with increasing charge density from amorphous (25% cationic monomers) to highly crystalline (100% cationic monomers). Reprinted with permission from Langmuir 1998;14:4902 © American Chemical Society[21].

2.1.4. Coatings from nanodispersions of PEFAs [22]

Films of PEFAs are regularly prepared by the solvent cast procedure form organic solutions. The best solvents for these complexes are fluorinated. For scientific purposes this situation is acceptable, however, not for the development of commercially viable PEFA products. Only materials that combine low cost and ecologically friendly synthesis have a chance of coming into everyday use. Here, it is important to avoid organic solvents. In order to do this, waterborne nanodispersions of PEFA complex coatings have been developed. One example is the complex of polyethyleneimine (p_3), a branched water-soluble polymer that is widely used in the paper industry [23], and Fluowet SB (a_3), which is frequently used as a spreading agent [24].

Complex dispersions of p_3–a_3, which are stabilized by an excess of a_3, consist of particles with diameters of about 200 nm. These complex dispersions are freeze-dried and redispersed in water. An interesting characteristic of the nanoparticles is their internal lamellar structure. The X-ray scattering diagrams of a solvent cast film and a complex dispersion are shown in Fig. 15(a) and (b). In the small-angle region, two reflections are found; these correspond to a first- and third-order reflection of a lamellar smectic A-like mesophase. The reflex positions show the long period to be $d = 3.6$ nm for the powder complex, and 3.8 nm for the complex nanodispersion. The absence of second-order reflections indicates a symmetrical lamellar two-phase system that consists of two types of alternating layers. One layer is strongly enriched with perfluorinated alkyl chains while the second layer is enriched with polyelectrolyte chains and ionic head groups. The thickness of each is about 1.8 nm for the powder complex and 1.9 nm for the nanodispersion complex. The slightly larger long period found for the nanodispersion complex particles compared to that of the powder complex is explained by the less densely packed structure of the latter, which is caused by the boundary effects of small particles (curvature). The scattering behavior of lamellar particles of finite-size has been described in detail [25]. Only an amorphous halo at about 2 nm^{-1} is found in the wide-angle region (Fig. 15), thus proving the

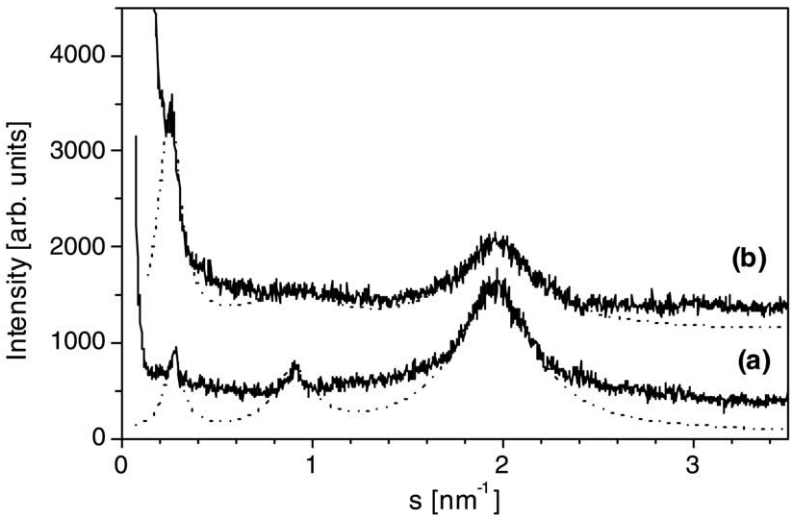

Fig. 15. X-ray scattering curves of polyethyleneimine–Fluowet SB complexes as a function of the scattering vector. The scattering patterns indicate lamellar mesomorphic smectic A-like structures: (a) complex powder made by the classical precipitation procedure described earlier [100] and (b) complex dispersion with particle sizes of about 200 nm. The straight lines are fitted curves, consisting of Lorentzian profiles for determination of the structure parameters. For the powder (a) the long period is determined to be $d = 3.6$ nm and for the dispersion $d = 3.8$ nm. The broad reflection in both curves at about 2 nm^{-1} represents an amorphous halo of the fluorinated alkyl chains. Reprinted with permission from Advanced Materials 1999;11:323 © Wiley–VCH[22].

absence of any crystallinity. From this value an average distance of 0.5 nm is given for the fluorinated alkyl chains. In the scattering curve of the powder (Fig. 15(a)), the halo is smaller than that found for the complex dispersion (Fig. 15(b)). This indicates a better packing of fluorinated chains in the material in bulk form than when it is dispersed, which again may be due to the boundary effects of the small particles.

The surface free energy of a solid can be used as a guide to its relative adhesive properties. Dynamic contact angles of test liquids with different surface tensions have been measured by means of the sessile drop method [20]. It is found that all non-polar liquids, which spread readily on pristine surfaces, show high contact angles for complex-coated surfaces. From the contact angles of a homologue series of non-polar liquids the critical surface tension γ_c of coatings on different substrates have been calculated. As shown in Fig. 16(a) and summarized in Table 1, Zisman plots result in critical surface tensions varying from 13.1 to 5.7 mJ/m^2 depending on the coated material. The latter value is identical the lowest critical surface tension encountered to date (6 mN/m) [26]. It can be concluded that the complex-coated surfaces presented here must be strongly enriched with CF_3-groups.

The wettability data are also used to determine the dispersion force component of the surface energy γ_s^d by using the Girifalco–Good–Fowkes–Young equation [27–29]. Fig. 16(b) shows such Girifalco–Good–Fowkes–Young plots for the dynamic advancing contact angle data which is obtained for glass and aluminum. Linear fits resulted in dispersive surface energies of 10.2–10.7 mJ/m^2 for the complex coating, which is independent of the substrate (Table 1). Both γ_c and γ_s^d values indicate a rather ordered packing in the perfluorinated segments, exposing CF_3-groups at the surface of the materials. It is worth noting that the contact angle measured with water (the most polar test liquid, $\gamma_l = 72.7$ mN/m) is

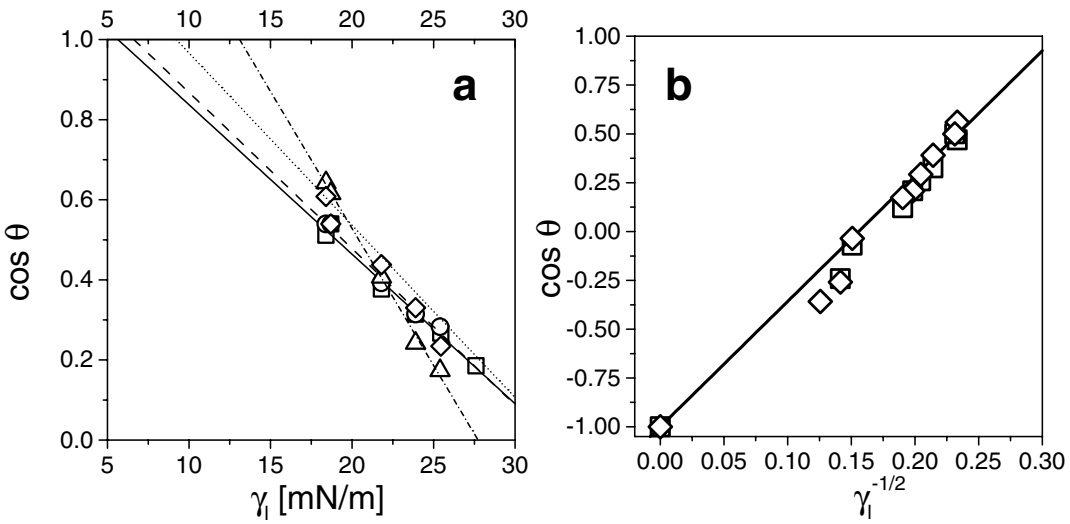

Fig. 16. Surface energy determination of complex coated surfaces. (a) Zisman plots for different polyethyleneimine–Fluowet SB coated surfaces. The points are obtained with (1) hexane, $\gamma_l = 18.4$ mN/m; (2) PDMS, $\gamma_l = 18.7$ mN/m; (3) octane, $\gamma_l = 21.8$ mN/m; (4) decane, $\gamma_l = 23.9$ mN/m;(5) dodecane, $\gamma_l = 25.4$ mN/m; (6) hexadecane, $\gamma_l = 27.6$ mN/m; the critical surface tensions are 5.7 mJ/m^2 (glass, squares), 6.6 mJ/m^2 (airplane wing, circles), 8.6 mJ/m^2 (aluminum, diamonds), 13.1 mJ/m^2 (painted car bodywork, triangles). Advancing contact angles are used for cos θ. (b) Girifalco–Good–Fowkes–Young plots for the determination of the dispersive surface energy of the PEI–Fluowet SB coated surfaces. From left to right points are values obtained with (1) methylene iodide, $\gamma_l = 50.0$ mN/m; (2) α-bromonaphthalene, $\gamma_l = 44.0$ mN/m; (3) hexadecane, $\gamma_l = 27.6$ mN/m; (4) dodecane, $\gamma_l = 25.4$ mN/m; (5) decane, $\gamma_l = 23.9$ mN/m; (6) octane, $\gamma_l = 21.8$ mN/m; (7) PDMS $\gamma_l = 18.7$ mN/m; (8) hexane $\gamma_l = 18.4$ mN/m; From the slope both values of γ_s^d are calculated to be 10.3 mJ/m^2 (glass, squares) and 10.7 mJ/m^2 (aluminum, diamonds). Reprinted with permission from Advanced Materials 1999;11:322 © Wiley–VCH [22].

smaller than that of methylene iodide ($\gamma_l = 50.0$ mN/m) and that it depends strongly on the coated surface (i.e. θ is higher for a sprayed car bodywork than for a glass slide). This is clear evidence of the surface reconstruction of the complex surface when it is in contact with water. Such reconstruction phenomena are widespread in polymer coatings, e.g. those observed in self-organizing semifluorinated side-chain ionenes [30] and even polymers containing only a few polar groups like Teflon–PFA show surface reconstruction when they are in contact with water [31].

Table 1
Zisman critical surface energies γ_c and the dispersive surface energies γ_s^d according to the Girifalco–Fowkes–Young equation for thin complex films on different substrates

Substrate	γ_c (mJ/m^2)	γ_s^d (mJ/m^2)
Glass	5.7 ± 1.7	10.3 ± 0.2
'VW' sheet	13.1 ± 1.2	10.2 ± 0.6
'Lufthansa' sheet	6.6 ± 1.4	10.3 ± 0.4
Aluminum	8.6 ± 2.1	10.7 ± 0.3

Reprinted with permission from Adv Mater 1999;11:322 © Wiley–VCH [22].

2.1.5. Surface structure [32]

A detailed investigation of the surface structure and the solid-state properties of poly[(acrylamidopropyl)trimethylammonium chloride] (p_2) and Fluowet SB (a_3) complex (p_2-a_3) has been presented [32]. Surfaces from complex p_2-a_3 show Zisman critical surface energies of 6.9 ± 0.8 mJ/m^2 on complex coated aluminum surfaces and 4.6 ± 1.4 mJ/m^2 on complex coated glass slides. The dispersive surface energies according to the Girifalco–Fowkes–Young equation are 8.1 ± 0.4 and 9.3 ± 0.5 mJ/m^2, respectively. The complex p_2-a_3 shows a fast but reversible reorganization when in contact with water, which results in enhanced surface energies of about 34 mJ/m^2 on aluminum as well as on glass substrates.

This surface reconstruction when in contact with water seems to be very fast, as shown by the constant contact angle of water, which adjusts to an equilibrium within some seconds. The reason for this is found at the nanometer level. Visualization of surfaces of complex p_2-a_3 films is achieved by AFM. The film surface is smooth, even at the micrometer level, whereas it appears structured at a nanometer level (Fig. 17 inset). This structuring consists of elevations and depressions with the distances between elevations ranging from 100 to 300 nm, resulting in a pattern resembling a leopard's fur. Remarkably the elevations have a very uniform height of about 3.4 nm (Fig. 17).

An important question is whether this surface structuring modifies the surface properties. Indeed, it is well known that contact angles are influenced by surface roughness. However, the length scale and roughness morphology observed for complex p_2-a_3 surfaces cannot be compared to a Lotus-like [33,34] or a fractal surface [35]. As far as is known the high values of advancing and static contact angles are not due to the roughness of the surfaces. Nevertheless, this roughness may explain the relatively low receding angles, which are sensitive to physical as well as chemical heterogeneities. The uniform

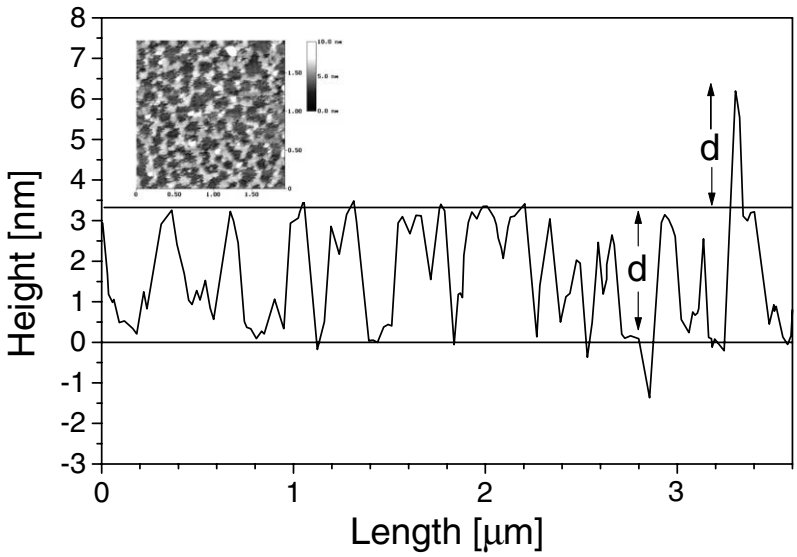

Fig. 17. A typical AFM depth profile of a poly[(acrylamidopropyl)trimethylammonium] Fluowet SB complex surface. A uniform height of about 3.4 nm was measured for the elevations, which is originated by a bilayer structure. It can be seen in the right hand figure that sometimes a second elevation on the first elevation can be found, as would be expected from a bilayer on a bilayer. The inset shows a 2 × 2 μm AFM image of the surface (the scale bar is 10 nm). Reprinted with permission from Langmuir 1999;15:4870 © American Chemical Society [32].

elevation height of 3.4 nm can be explained by the presence of large islands (100–300 nm) of lamellar complex sheets in a head-to-head double-layer arrangement. Within such islands, the sulfonate head groups are separated by cationic polyelectrolyte chains. However, the edges of the islands are energetically very unfavorable, allowing highly polar solvent molecules to penetrate into the polyelectrolyte-rich region. Consequently, when in contact with water, a fast surface reorganization occurs resulting in a much higher-energy surface (34.2 mJ/m^2) than observed for non-polar liquids. This indicates that the thermodynamic equilibrium state of the complex/liquid interface depends on the polarity of the liquid, and that water induces a kinetically favored enrichment of polar groups at the edge of the complex islands.

2.1.6. Hexagonal columnar discotic structures [36]

Perfluorodecanoic acid is a hydrophobic fluorinated surfactant which forms disk-like micelles in diluted aqueous solution [37]. It is shown in Section 2.1.3 that the complexation of poly[(diallyldimethylammonium chloride)-*co*-(*N*-methyl-*N*-vinylacetamide)] with perfluorodecanoic acid results in perforated lamellar complexes with an increasing density of perforations per unit area and an increasing degree of side-chain crystallinity when the charge density of the polymer is increased. The question in this section is whether the charge density influences the structure of the complexes even when the length of the fluorinated moiety is as large as 17. For clarity a representation of the complex formation is given in Fig. 18.

In order to investigate the influence of the charge density on the structure five polymer complexes, varying in the amount of diallyldimethylammonium units, i.e. 25, 47, 65, 83 and 100 mol%, are prepared (P1a–C18 to P1e–C18). These salt-free binary systems with 1:1 stoichiometry present, similar to

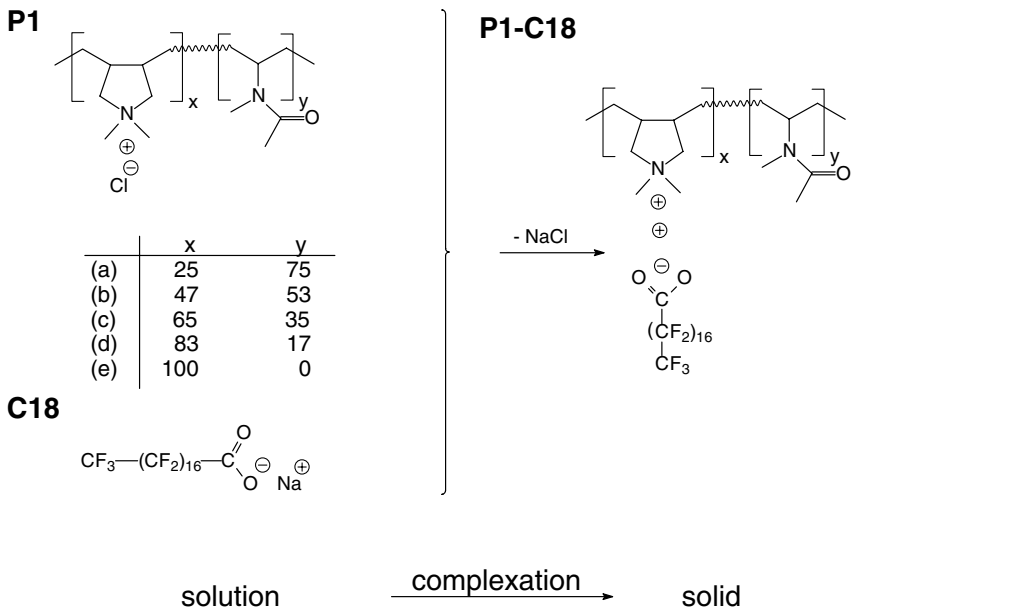

Fig. 18. Complex formation: (P1a–P1e) poly[(diallyldimethylammonium chloride)-*co*-(*N*-methyl-*N*-vinylacetamide)s]; (C18) perfluorooctadecanoic acid; (P1a–C18 to P1e–C18) stoichiometric polyelectrolyte–surfactant complexes. Reprinted with permission from Langmuir 1999;15:6724 © American Chemical Society [36].

diblock copolymers, the simplest case for studying various aspects of microphase transition of fluorinated long-chain surfactants [36].

2.1.6.1. Wetting. Surface energies of the complexes are determined by *n*-alkane wettability measurements. The preparation of complex surfaces is carried out by pressing discs from powder, as described for the preparation of Teflon FEP [19]. However, the procedure is modified by restricting the temperature to not more than 30 °C. The wettability of the complex surfaces with a series of *n*-alkanes is then determined by dynamic contact angle measurements (Table 2). For comparison of the contact angle data, the solid surface energies are calculated using the equation of Neumann and Li [19]. Within the series the maximum value is found for complex P1a–C18 to be 13–14 mN/m.

A minimum surface energy is found for complex P1e–C18, which is between 9 and 10 mN/m (Table 2). Obviously, the surface energy of the complexes decreases with the increasing charge density of the polyelectrolyte, which is accompanied by an increasing amount of perfluorooctadecanoate. For determination of the dispersive component, the wetting relation according to the Girifalco–Good–Fowkes–Young equation [27–29] is found to be suitable. The resulting values for the dispersive surface energies are summarized in Table 2. A comparison of γ_s with γ_s^d shows that the γ_s-values are, at most, 1–3 mN/m higher than the γ_s^d-values. From this it can be concluded that the polymer–liquid interaction is to a large extent dispersive. For the complexes P1a–C18 to P1e–C18, the maximum distance of the

Table 2
The solid surface energies of complexes P1a–C18 to P1e–C18 shown in Fig. 18

Complex	Test liquid	θ_{adv} (°)	θ_{st} (°)	θ_{rec} (°)	γ_s (mN/m)	γ_s^d (mN/m)
P1a–C18	Decane	61	60	54	13.3	
	Dodecane	65	65	55	13.3	13.0
	Hexadecane	67	67	52	14.1	
	Decane	62	60	49	13.0	
P1b–C18	Dodecane	68	68	51	12.5	12.4
	Hexadecane	70	69	52	13.2	
P1c–C18	Decane	65	64	44	12.2	
	Dodecane	70	69	50	12.0	11.7
	Hexadecane	72	72	49	12.6	
P1d–C18	Decane	72	70	53	10.5	
	Dodecane	75	74	55	10.6	9.9
	Hexadecane	80	80	48	10.3	
P1e–C18	Decane	76	74	50	9.5	
	Dodecane	78	77	54	9.9	9.1
	Hexadecane	82	81	55	9.8	

The surface energies γ_s are calculated using the equation of Neumann and Li [19]. Surface tensions of test liquids used for calculations are 23.43 mN/m (decane), 25.44 mN/m (dodecane) and 27.76 mN/m (hexadecane). γ_s^d is the dispersion force component of the surface energy extrapolated according to the Girifalco–Good–Fowkes–Young equation [27–29] using advancing contact angles. θ_{adv}, θ_{st}, θ_{rec} are advancing, static and receding angles. Reprinted with permission from Langmuir 1999;15:6724 © American Chemical Society [36].

carboxylate groups and the polyelectrolyte chains to the surface is about 2 nm. This is large enough to suppress the polar components of the surface energy [38].

From the very low surface energies, consisting predominantly of dispersive forces, it can be concluded that these low surface energies indicate rather ordered packing of the perfluoroalkyl segments, exposing CF_3-groups at the surface of the complexes. Further, it can be concluded that the surface packing density of CF_3-groups increases with the increasing charge density of the polyelectrolyte. This is in contrast to complexes with short-chain perfluorinated acids, which do not show a dependence of the surface energy on the charge density (Section 2.1.3).

2.1.6.2. Nanostructures. Periodic nanostructures with repeat units on a length scale in the range 1–10 nm can be expected for the complexes P1a–C18 to P1e–C18. Small-angle X-ray measurements are performed in order to prove this assumption. As expected, for P1a–C18 to P1e–C18, a series of reflections are found in the scattering curves. As can be seen in Fig. 19, that there are five reflections, which divide into two groups. The relative positions of the three broader reflections, at lower scattering vectors, are $1:\sqrt{3}:2$ and that of the two sharper reflections, at higher scattering vectors, is 1:2. No meaningful values are found for the positions of the reflections between these two groups.

For the interpretation of the characteristic scattering pattern, it is assumed that the phase behavior of analogous perfluorinated carbon acids is decisive. The phase behavior of single chain perfluorinated carbon acids is characterized by the formation of disc-shaped micelles in low concentrations [39,40]. At higher concentrations it is often the case that neither the cubic nor the hexagonal phase exists, and that the lamellar phase borders on an isotropic micellar solution [39]. Sometimes it is found that a discotic nematic phase exists in an intermediate position between the isotropic and lamellar phases [41]. The lack of cubic and hexagonal phases is explained by the aggregation of the disc-shaped micelles, which form a lamellar phase even at low concentrations [42]. It has been shown that perfluorooctadecanoic acid forms monodisperse thin disc-like micelles at low concentrations (10^{-3}–10^{-2} mol/l) [37].

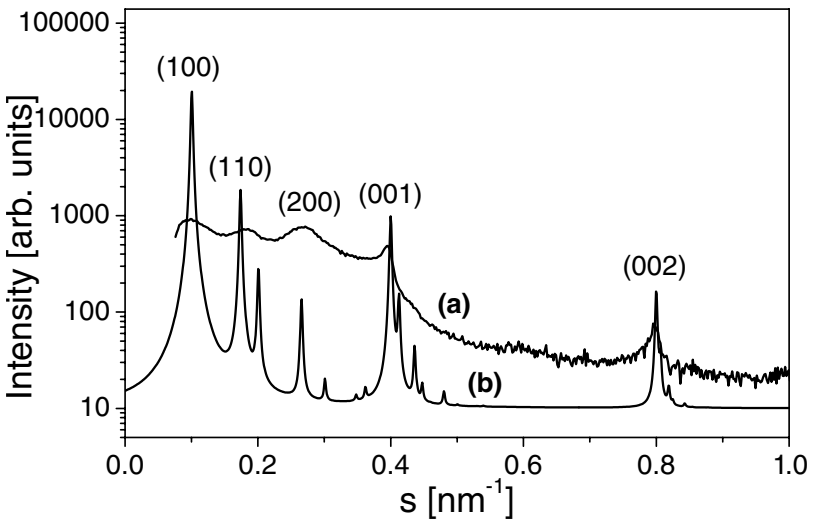

Fig. 19. The small-angle X-ray scattering curve of complex P1c–C18 (curve a) and a calculated curve according to a hexagonal columnar structure with a column distance of 11.5 nm and an inter-columnar disc distance of 2.5 nm (curve b). Reprinted with permission from Langmuir 1999;15:6724 © American Chemical Society [36].

The complex preparations are performed at a temperature at which monodisperse micelles are present. Therefore, the complex formation may be explained by the following simple mechanism. At first, the micelles agglomerate into columns which are packed into a two-dimensional hexagonal lattice in a second step. In this model the polyelectrolyte chains act as a kind of glue which prevents the merging of micelles forming extended lamellar sheets. The repulsive Coulomb forces between negatively charged micelles are replaced by attractive forces. Probably the very long fluorinated C17 alkyl chains cause slow exchange dynamics between the micelles and the soluted molecules. Therefore, the micelles may be stable while the complexation proceeds. Further, the critical micelle concentration of about 8×10^{-5} mol/l is extremely low [37], from which it can be concluded that the complexation of single molecules [13] cannot be a relevant competitive process. Analytical scattering curves of hexagonally packed discotic columns are calculated and compared with the measured scattering curves. An example is shown in Fig. 19. It can be seen that reflex positions and approximated intensities are reproduced in this simple model. From the position of the 001 and 002 reflections, an intra-columnar distance of about 2.5 nm is calculated which is independent of the charge density of the polyelectrolyte. The positions of the 100, 110 and 200 reflections give the distances of the column centers which decreases slightly from 12.0 nm (complex P1a–C18) to 10.0 nm (P1e–C18).

The lengths of the perfluorooctadecanoate chains in an all-*trans* conformation are calculated to be about 2.45 nm [37]. This is nearly the same as the intra-columnar disc distance. An interdigitated arrangement of the fluorinated chains within the discs is consistent with this length and the known stiffness of perfluorinated alkyl chains [39]. Further, the surface of each disc is enriched with carboxylate head groups. A model of the hexagonal columnar discotic structure is hown in Fig. 20.

2.1.6.3. Side-chain order. In Section 2.1.3 it is shown that the ordering of fluorinated chains in solid polyelectrolyte–fluorosurfactant complexes may be tuned between liquid-like and crystalline structures by the charge density of the polyelectrolyte. In the wide-angle diagram of the complexes P1a–C18 to P1e–C18, two broad reflections with maxima at 1.8 and 4.2 nm^{-1} are found, superimposed by an intense

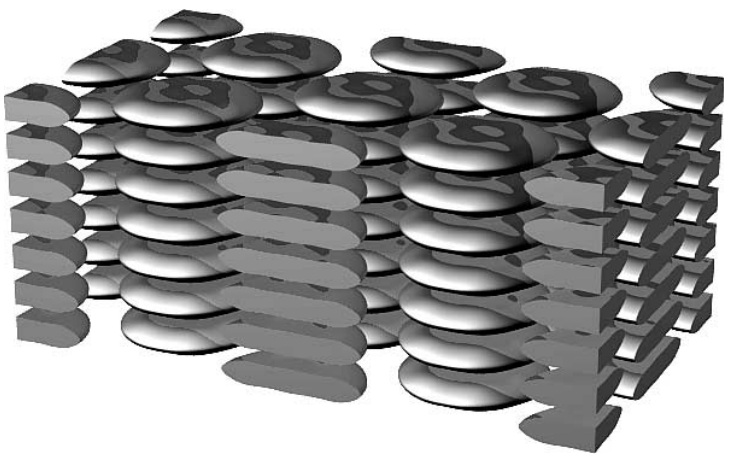

Fig. 20. A model of the hexagonal columnar discotic structure. The column center distance decreases slightly from 12.0 to 10.0 nm with the increasing charge density of the polyelectrolyte (P1a–C18 to P1e–C18), while the intra-columnar distance remains constant (2.5 nm). The polyelectrolyte (not shown) fills the space between the discs. Reprinted with permission from Langmuir 1999;15:6724 © American Chemical Society [36].

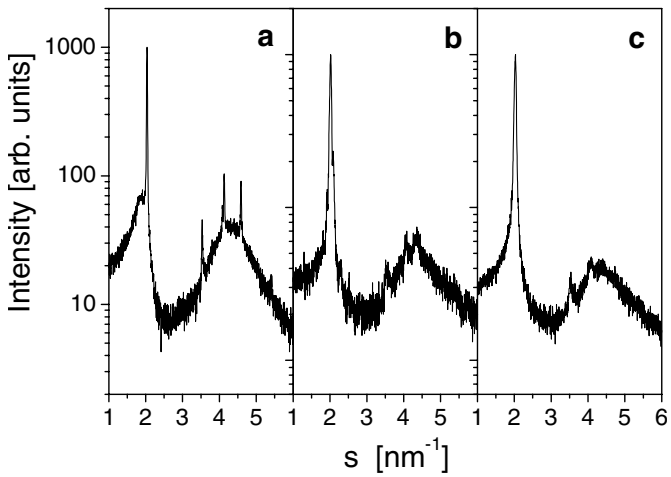

Fig. 21. Wide-angle X-ray diagrams of polytetrafluoroethylene in the hexagonal IV phase (curve a), perfluorooctadecanoic acid (curve b) and complex P1c–C18 (curve c). Reprinted with permission from Langmuir 1999;15:6724 © American Chemical Society [36].

sharp reflection at 2.03 nm^{-1} and two weak reflections at 3.53 and 4.08 nm^{-1} (Fig. 21(c)). The relative positions of the latter are 1:$\sqrt{3}$:2. This is indicative of a partially hexagonal arrangement of the long-chain perfluorinated moieties. A comparison of the scattering curves of the complexes P1a–C18 to P1e–C18 with that of pure perfluorooctadecanoic acid (Fig. 21(b)) and polytetrafluoroethylene (Fig. 21(a)) reveal a very similar shape. In particular the reflex positions are found to be almost identical. From this it is concluded that a kind of side-chain crystallinity is present in the complexes, which crystallizes in a lattice in a very similar way to that described for polytetrafluoroethylene in the hexagonal IV phase, and with the same lateral chain-to-chain order. The chain-to-chain distance is therefore 0.57 nm. In contrast to the hexagonal IV phase, the lower number of reflections and the increased width of the reflections are explained by the lack of a periodic arrangement in the direction of the chains, as well as a smaller domain size. The domain size relevant for the wide-angle scattering is that of a crystallite of polytetrafluoroethylene. For the complexes, the domain size is limited to that of the discs. The structure shown in Fig. 20 may result from a fast crystallization of the perfluorinated moieties. Therefore, on the basis of the current data, non-equilibrium structures cannot be ruled out.

2.1.7. Ultra-thin films [43]

This section reports on the nanostructure and the physical properties of a complex (PEI–FSA), which are formed by PEI (Section 2.1.4) and a partially fluorinated carboxylic acid, FSA. The complexation is shown schematically in Fig. 22. The lithium salt of FSA is used as an active spreading agent. A comparison of the IR spectra of FSA and PEI–FSA shows that the carboxylic acid vibrations found for FSA at 1690 cm^{-1} (C=O stretch, dimer) and at 1300 cm^{-1} (C–O stretch, dimer) are absent in the spectrum of PEI–FSA (Fig. 23). From this it can be concluded that the complex has a 1:1 stoichiometry.

2.1.7.1. Thermal properties. The thermal properties of the surfactant FSA and the complex PEI–FSA have been investigated by using DSC and TGA. The second heating DSC traces are shown in Fig. 24. A sharp endothermic peak at 45 °C is present for FSA and a peak at 180 °C for PEI–FSA. These peaks are

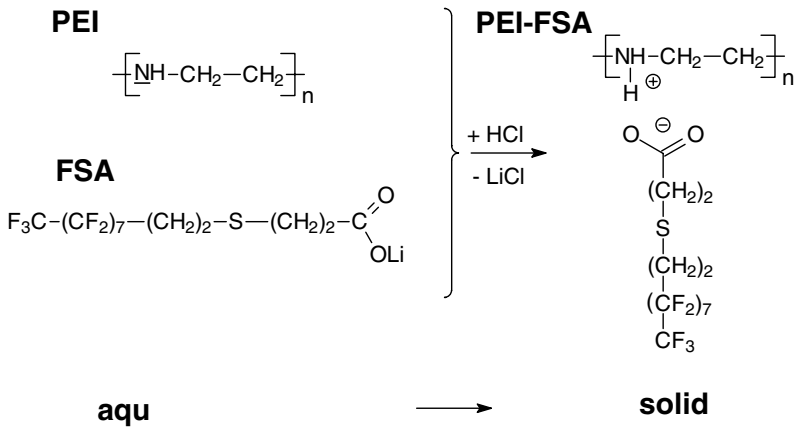

Fig. 22. Complex formation: (PEI) polyethyleneimine; (FSA) 3-[(1*H*,1*H*,2*H*,2*H*-fluorooctyl)thio] propionic acid; (PEI–FSA) stoichiometric polyelectrolyte–surfactant complex. Reprinted with permission from Langmuir 2000;16:8562 © American Chemical Society [43].

attributed to the melting transitions of the compounds. Below these temperatures the morphology of the compounds are constant. The considerable rise of 135 °C in the melting point of the complexed surfactant PEI–FSA compared to that of the non-complexed compound FSA is surprising and must be considered as a consequence of the stabilizing effect of the complexation. It is known that polyethyleneimine possesses good thermal stability compared to other polyelectrolytes and that no substantial decomposition in air occurs below 300 °C [44]. Therefore, it is suggested that its complexes with fluorinated surfactants are also thermally stable. This has been proved by TGA. It is found that the decomposition of the complex starts at temperatures above 280 °C, followed by a rapid decrease of about

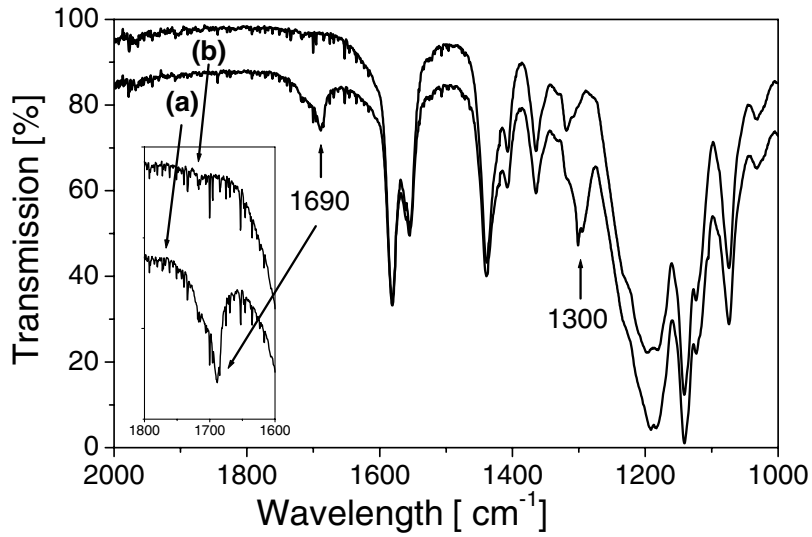

Fig. 23. FTIR-spectrum of the surfactant FSA (curve a) and that of its complex PEI–FSA with polyethyleneimine PEI (curve b). For the structures of the compounds see Fig. 22. In the spectrum of the surfactant an intense carboxylic acid band at a wave number of 1690 cm^{-1} is found. This results from the C=O stretch vibration. Reprinted with permission from Langmuir 2000;16:8562 © American Chemical Society [43].

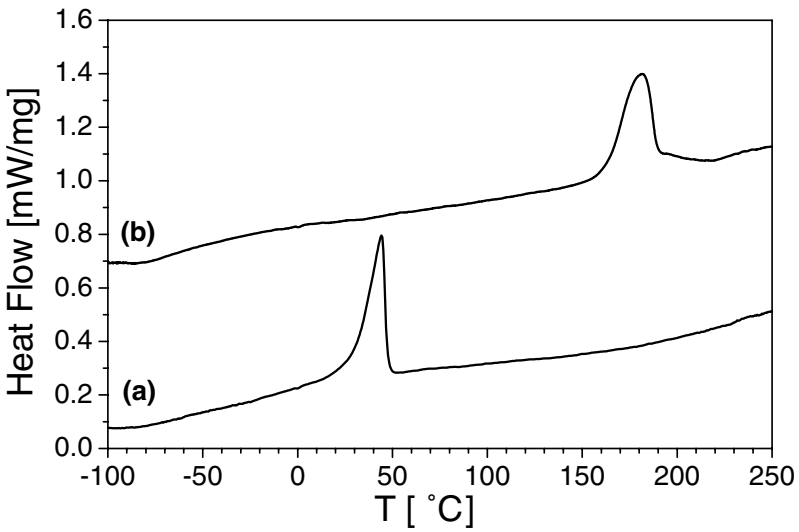

Fig. 24. DSC heating traces of the surfactant FSA (curve a) and the complex PEI–FSA (curve b). Melting points are at 45 and 180 °C for FSA and PEI–FSA, respectively. Reprinted with permission from Langmuir 2000;16:8562 © American Chemical Society [43].

80% of the total mass up to 350 °C. Therefore, it is concluded that the thermal stability of the complex is not much lower than that of PEI.

2.1.7.2. Wetting. Complex surfaces are prepared by spin-casting a 0.1% (w/w) complex solution onto silicon wafers. Dynamic contact angles of the test liquids with different surface tensions are measured by means of the sessile drop method [45] after the evaporation of the solvent (1,1,1,3,3,3-hexafluoropropanol). It is found, in particular, that all non-polar liquids, which spread readily on uncoated surfaces, show high contact angles on complex-coated surfaces (Table 3). In addition the values of the contact angles are independent of the film thickness in the experimental range 5.7–370 nm (see section, thin films). The surface energies calculated using the equation of Neumann and Li [19], range from 9.7 to 12.6 mN/m for all test liquids with surface tensions in the range 18.4–50.0 mN/m (Table 3). Zisman plots result in a critical surface tension of 7.1 ± 1.2 mN/m for complex coated silicon wafers (Fig. 25). Within the experimental range of error, the value is equal to the lowest critical surface tension observed to date (6 mN/m) [26], which are measured for an oriented closely packed monolayer of perfluorododecanoic acid. Such low critical surface tensions characterize the resulting properties of a surface of closely packed perfluoromethyl $-CF_3$-groups. Therefore, it is concluded that the complex-coated surfaces presented are strongly enriched with CF_3-groups.

The wettability data are also used to determine the dispersion force component of the surface energy γ_s^d by using the Girifalco–Good–Fowkes–Young equation [27–29]. The Girifalco–Good–Fowkes–Young plots are used to show the dynamic advancing contact angle data obtained for complex surfaces on silicon wafers (Fig. 26). Linear fits result in a dispersive surface energy of $\gamma_s^d = 10.1 \pm 0.3$ mN/m. Both γ_c and γ_s^d values indicate a fairly ordered packing of the perfluorinated segments, exposing CF_3-groups on the surface. It is particularly interesting that the contact angles of water (the most polar test liquid with $\gamma_l = 72.7$ mN/m) are smaller than those of methylene iodide ($\gamma_l = 50.0$ mN/m). The calculated surface energy using the equation of Neumann and Li [19] has been determined to be

Table 3
List of contact angles of different test liquids on materials coated with complex PEI–FSA at 20 °C

Solvent	γ_l (mN/m)	Advancing angle (°)[a]	Stationary angle (°)[a]	Receding angle (°)[a]	γ_s (mN/m)
Hexane	18.4	57	55	39	11.1
PDMS[b]	18.7	60	59	40	10.7
Octane	21.8	67	65	60	10.9
Decane	23.9	72	72	65	10.7
Dodecane	25.4	76	74	69	10.3
Hexadecane	27.6	82	80	73	9.7
α-Bromonaphthalene	44.0	93	93	87	12.6
Methylene iodide	50.0	102	100	90	11.4
Water	72.7	80	75	20	35.5

The surface tensions of the test liquids γ_l, advancing, stationary and receding contact angles, are measured by a Krüss contact angle goniometer and are listed. γ_s is the surface energy calculated by using equation of Neumann and Li [19] and advancing contact angles. Reprinted with permission from Langmuir 2000;16:8562 © American Chemical Society [43].

[a] Error of measurement ca. 1°.

[b] Commercial product of poly(dimethylsiloxane) oligomers (trimethylsiloxy terminated) from Geltest Inc.

35.5 mN/m. The low surface energies determined for non-polar liquids can be reproduced, even when the complex coated surfaces are dried after their re-immersion in water. These surface reconstructions seem to be very fast when in contact with water, as shown by the constant contact angle of water, which adjusts to an equilibrium within a few seconds. It is suggested that the reason for this could be found in a nanometer scale topology such as the leopard's fur pattern, which is found for a polymeric complex of a fluorinated double-chain surfactant (Section 2.1.5 and Fig. 17). This nanoscale structured surface is proved to perform fast and reversible surface reconstruction when in contact with water.

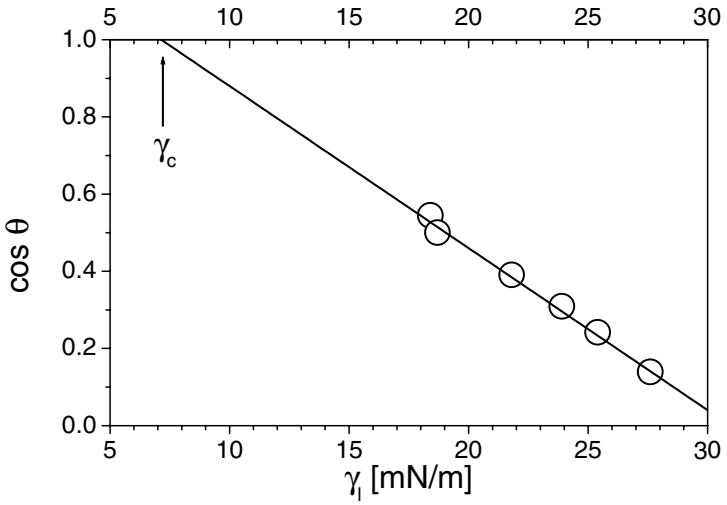

Fig. 25. Zisman plot for complex coated silicon wafers. Points are obtained with (1) hexane, (2) PDMS, (3) octane, (4) decane, (5) dodecane, (6) hexadecane. The critical surface tension of a complex on a silicon wafer is calculated to be 7.1 ± 1.2 mN/m by extrapolating a linear fit (solid line) of the cos θ (circles) to cos $\theta = 1$. Advancing contact angles are used for cos θ. Reprinted with permission from Langmuir 2000;16:8562 © American Chemical Society [43].

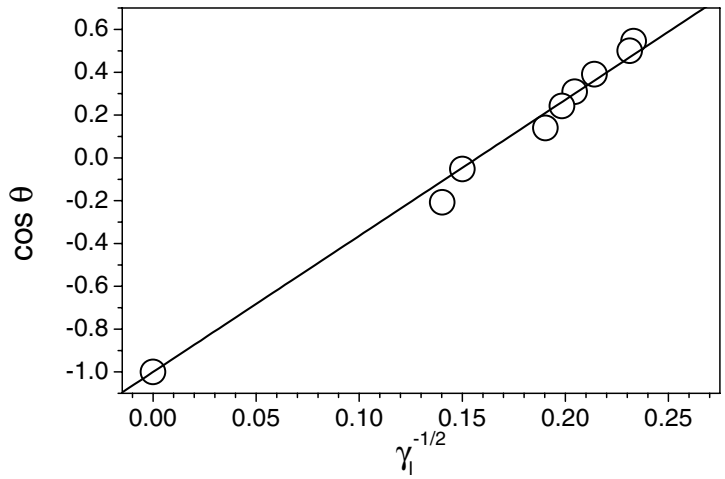

Fig. 26. Girifalco–Good–Fowkes–Young plots for the determination of the dispersive surface energy of a complex coated silicon wafer surface. From left to right the points are values obtained with (1) methylene iodide, (2) α-bromonaphthalene, (3) hexadecane, (4) dodecane, (5) decane, (6) octane, (7) PDMS (8) hexane. γ_s^d are calculated to be 10.1 ± 0.3 mN/m from the slope (circles are measured angles; the solid line is their least square fit). Reprinted with permission from Langmuir 2000;16:8562 © American Chemical Society [43].

2.1.7.3. Nanostructure in the bulk material. The molecular order of fluorinated side-chain polymers is determined primarily by the length of the fluorinated moieties, which act in addition as mesogenic groups [30,46]. In Sections 2.1.2 and 2.1.4, it is shown that the ordering of fluorinated chains in solid polyelectrolyte–fluorosurfactant complexes are liquid-like for short-chain surfactants, and in Section 2.1.3 it is shown that the ordering can be tuned between liquid-like and crystalline by the charge density of the polyelectrolyte. In the case of long-chain surfactants, this is semicrystalline (Section 2.1.6.3). It can be seen in the wide-angle diagram of a powder of PEI–FSA (Fig. 27) that an intense reflection is

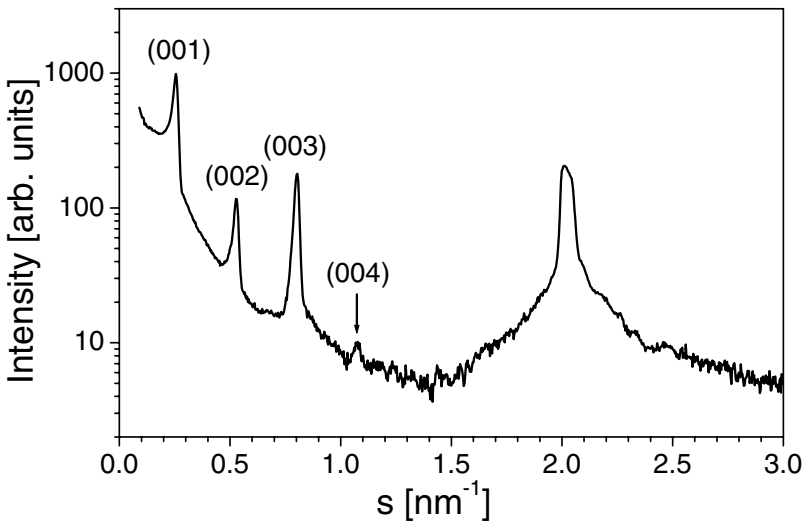

Fig. 27. X-ray diffraction pattern of a complex PEI–FSA powder measured by transmission geometry. Reprinted with permission from Langmuir 2000;16:8562 © American Chemical Society [43].

present in the wide-angle region at 2.0 nm^{-1}. This indicates a two-dimensional hexagonal lattice which is interpreted as arising from the close packing of the fluorinated segments, which have a chain-to-chain-distance of 0.577 nm. A similar molecular ordering has been reported for a fluorinated poly(α,L-glutamate) with a C12 semifluorinated side-chain [46]. Furthermore, this is similar to the close packing of fluorinated chains in poly(tetrafluoroethylene) crystals of the hexagonal IV phase with a chain-to-chain distance of 0.57 nm [47].

The finding of a side-chain crystallinity is consistent with the DSC measurements, from which it is concluded that the crystalline side-chains melt at 180 °C. This result is similar to the side-chain crystallinity of a complex of PEI with perfluorinated acids, where a melting transition is observed at 163 °C for a fluorinated chain length of C16 (Section 2.1.8). In contrast to complexes of PEI with perfluorinated acids, the fluorinated chains of PEI–FSA are significantly shorter (C8) but show a higher melting point. This is attributed to the better packing of the latter. It can be seen in the small-angle region of Fig. 27 that four equidistant reflections are present, this is characteristic of a layered structure in the bulk material. A layer distance of $d = 3.75$ nm is determined from the peak positions. This is consistent with the investigations of fluorinated polyelectrolyte–surfactant complexes presented in the preceding sections and reveals that they have highly ordered nanostructures. By analogy with strongly separated mesophase structures, the lamellar structure are interpreted as consisting of sheets of a thickness d_1, which are enriched in their fluorinated groups and sheets of a thickness d_2, which are enriched in their ionic groups and their polymer backbones. The long period is given by $d = d_1 + d_2$. From the relative intensities of the lamellar (001) to (004) reflections, the thicknesses of d_1 and d_2 are calculated to be 1.70 ± 0.05 nm and 2.05 ± 0.05 nm by using the J.J. Hermans model [7]. Using the terminology of the description of liquid crystals, the structure of complex PEI–FSA is designated as a bulk material which has a smectic B structure, and is stable, at least from 20 to 185 °C. The remarkably high thermal stability of the smectic B structure is comparable to that observed for a complex of a rod-like polyelectrolyte, which has been investigated by temperature dependent X-ray scattering [48].

The next question is, are ordered supramolecular structures possible in view of the branching of the PEI? This commercial product, which is used widely in the paper industry, has a molecular weight of $M_w = 25\,000$ g/mol and ratios of primary to secondary to tertiary amino groups of 34:40:26. Chen and Hsiao [49] have reported on lamellar complexes with dodecylbenzenesulfonic acid for the same PEI. They showed that considerable branching does not hinder the formation of an ordered supramolecular complex structure. Further, Hwang and Kim [50] have shown that the PEI of the same molecular weight and degree of branching could be very effective in assembling rigid Langmuir–Blodgett monolayers of fatty acids. Therefore, the occurrence of self-assembled structures with a high degree of order is not inconsistent with the irregular structure of the polymer backbone of PEI.

2.1.7.4. Structure of thin films. Thin complex films on silicon wafers are prepared by the spin-coat technique from complex solutions. The film structure is then investigated by X-ray reflectivity. Reflectivity curves of ultra-thin and thin complex films are shown in Figs. 28 and 29. Surprisingly well-defined double-layer stacks developed within a few seconds simply as the result of the deposition of droplets of the complex solution. In Fig. 28 the presence of Kiessig fringes indicate a smooth complex film. A thickness of 5.7 ± 0.5 nm is calculated from the angular positions of the fringes [51].

The reflectivity curve can be explained as resulting from 1.5 double layers. Here, a double layer is defined as a structure building block with an ionic sheet surrounded by fluorinated sheets. The latter are formed by the tails of the surfactants. With this definition the structure is given as follows: half an ionic

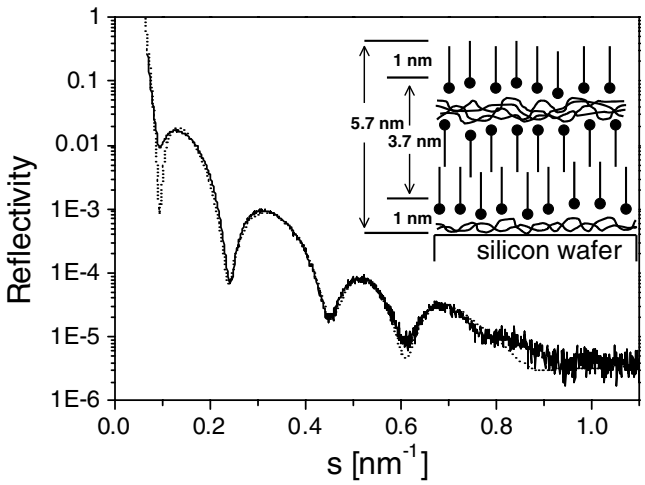

Fig. 28. X-ray reflectivity curve of an ultra-thin complex film (5.7 nm) complex PEI–FSA film on a silicon wafer (solid line, experimental curve; dotted line, fitted curve). The inset shows a sketch of the film structure in the direction vertical to the wafer surface. Reprinted with permission from Langmuir 2000;16:8562 © American Chemical Society [43].

layer (ca. 1.0 nm) lies at the complex/wafer interface, a double layer is in the middle (3.75 nm) and finally a fluorinated layer (ca. 1.0 nm) is located at the complex/air interface (Fig. 28 inset). This assumption can be confirmed by using a box model based on the Parrat formalism [52]. The fit is shown in Fig. 28 (dotted line). The lowest thickness of films is 5.7 nm which could be prepared. For films of larger thicknesses, which are in the range 20–400 nm, as determined by a surface profiler, three Bragg peaks appear. The differences between the peak positions are equidistant. Examples are shown in Fig. 29

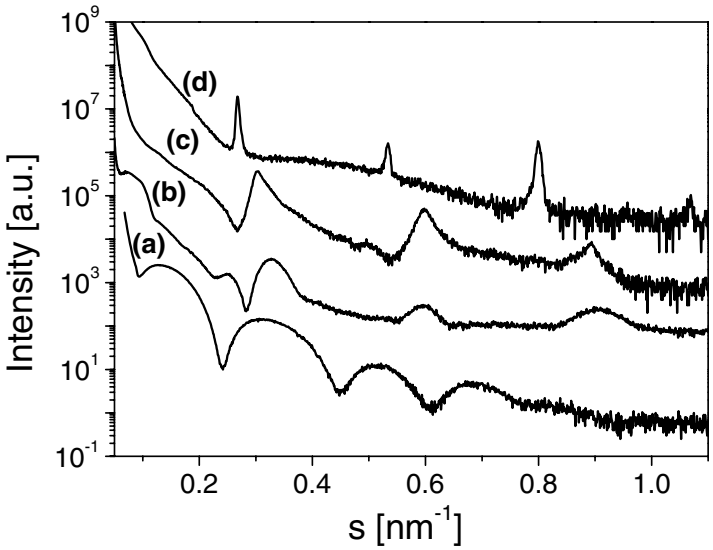

Fig. 29. X-ray reflectivity curves of complex PEI–FSA films on silicon wafers with vertically ordering of alternating fluorinated and ionic layers. The film thicknesses are 5.7 nm (curve a), 16 nm (curve b), 39 nm (curve c) and 370 nm (curve d). Reprinted with permission from Langmuir 2000;16:8562 © American Chemical Society [43].

(curves (b)–(d)). A lamellar spacing of 3.70 ± 0.05 nm is calculated from the reflex positions. Within the experimental error, this value is identical to that determined for the complex as material in the bulk form (3.75 nm). Because of the same nanostructure is developed in a slow film forming process (solvent casting) and in a fast film forming process (spin coating), it is concluded that the time which is necessary for the formation of the nanostructure is shorter than the time necessary for the formation of films. The latter is in the order of 1 s. Furthermore, as expected for a stack of multi-layers, the sharpness of the Bragg peaks increases with increasing film thickness in the line from curve b to d (Fig. 29). Vertical correlation lengths of 16 ± 1 nm (b), 39 ± 2 nm (c) and 370 ± 10 nm (d) are determined from the integral widths of the reflections.

The structure of the films consists of multi-layers aligned parallel to the wafer surface. In addition, from the result of the contact angle measurements and from the good adhesion of the films on the wafers, it is concluded that a fluorinated layer lies on the complex/air interface and an ionic layer lies on the wafer/complex interface. Therefore, the film resulting in curve b (Fig. 29) contains 4.5 double layers, that resulting in curve c contains 10.5 double layers and that in curve d contains about 100 double layers. The observed macroscopic orientation of the complex to multi-layers with a variability of about two decades in their thicknesses, which are produced in a single-step procedure, is a significant progress in using self-assembly for the preparation of thin organic films. Mechanical fields, present during the spin coating procedure, are probably the reason for the macroscopic orientation of the lamellar stacks parallel to the underlying substrate surface.

2.1.8. Fine-tuning of the surface energy [53]

This section reports on lamellar mesophases formed by complexes of polyethyleneimine (PEI) and perfluorinated carboxylic acids of different chain length (C4 to C16) resulting in polyethyleneimine perfluorocarboxylates (PEI–C4 to PEI–C16). The PEI is the same as described in Section 2.1.7. Varying the chain length of the surfactant complexes allow a fine-tuning of the surface energy. The stoichiometry of the complexes is determined by FTIR spectroscopy in the way described in Section 2.1.7.

2.1.8.1. Wetting. Thin films of the complexes with smooth surfaces are prepared by the spin-cast procedure using a 0.1% (w/w) complex solution onto silicon wafers. After the evaporation of the solvent (1,1,1,3,3,3-hexafluoropropanol), the wafers are stored overnight at 30 °C and then for 60 min at 100 °C. From the weight uptake, the thicknesses of the resultant complex coatings are calculated to be in the range 100–400 nm.

The wettability of the complex surfaces with *n*-decane, *n*-hexadecane, diiodomethane and water is then determined by dynamic contact angle measurements (Tables 4–7). It is found that the contact angles of the test liquid increase with an increasing chain length. By comparison, the static contact angles of PEI–C10 ($\theta_{st,n\text{-hexadecane}} = 77°$) and PEI–C12 ($\theta_{st,n\text{-hexadecane}} = 82°$) complex surfaces are at least as high as those found for adsorbed monolayers of C10 ($\theta_{st,n\text{-hexadecane}} = 72°$) and C12 ($\theta_{st,n\text{-hexadecane}} = 78°$) on platinum surfaces [26,54]. The latter are known to be the surfaces showing the lowest critical surface tension observed to date (6 mN/m). Similar high contact angles have been reported for side-chain crystalline polymers with C_8F_{17} fluorocarbon substituents with a polystyrene($\theta_{adv,n\text{-hexadecane}} = 82°$) [55], a methacrylate($\theta_{adv,n\text{-hexadecane}} = 81–82°$) [56] and an ionene-6,6 backbone ($\theta_{adv,n\text{-hexadecane}} = 81°$, $\theta_{st,n\text{-hexadecane}} = 75°$) [30], are all been shown to yield double layers of the hydrocarbon backbone and their fluorocarbon chains.

The use of contact angles to calculate surface energies is only reliable in the case of homogeneous and

Table 4
Dynamic contact angles of the polyethyleneimine perfluorocarboxylate complexes perfluorinated acids monolayers and fluorinated polymers against *n*-decane ($\gamma_l = 23.9$ mN/m)

Samples	θ_{adv} (°)	θ_{st} (°)	θ_{rec} (°)	$\gamma_{s,adv}$ (mN/m)	$\gamma_{s,st}$ (mN/m)
PEI–C4	37	37	36	19.4	19.4
PEI–C5	51	50	44	16.1	16.4
PEI–C7	61	59	47	13.3	14.0
PEI–C8	68	67	61	11.7	12.0
PEI–C10	78	76	71	9.2	9.7
PEI–C12	80	79	76	8.7	9.0
PEI–C16	80	78	75	8.7	9.2
C10[a]	–	62	–	–	13.3
C12[b]	–	70	–	–	11.0
I-6,6-F8H4[c]	71	66	62	10.9	12.2
F8-St[d]	71	–	56	10.9	–

θ_{adv}, θ_{st}, θ_{rec} are advancing, static and receding angles. $\gamma_{s,adv}$ and $\gamma_{s,st}$ are surface energies calculated using the Neumann and Li equation [19], first with static and then receding angles. Reprinted with permission from Langmuir 2000;16:824 © American Chemical Society [53].

[a] [54].
[b] Refs. [28,29].
[c] [30].
[d] [55].

smooth surfaces. In order to be sure that the high contact angles found for the PEI carboxylate complex surfaces are not due to roughness, the surfaces have been investigated by scanning electron microscopy. It is found that all complex surfaces are smooth on length scales in the range from several millimeters down to lengths lower than 1 μm. Therefore, roughness as the fact responsible for the high contact angles of the complex surfaces can be excluded. Thus, dynamic contact angles are used as a measure of the surface energies, which are calculated using the equation of Neumann and Li [19]. For carboxylic chain lengths larger than 4, the surface energies are significantly lower than 18.5–20 mN/m, which is the value for the standard low surface energy of polytetrafluoroethylene [47,57], which shows an advancing contact angle against hexadecane of 51°. In Tables 4–7, it can be seen that the surface energies calculated on the basis of advancing angles (γ_{adv}) differ only slightly from the values which are calculated using stationary angles (γ_{st}). In addition, the difference between the advancing and the receding contact angles is low (about 10°), which is further indicative of the low degree of roughness of the complex surfaces. In the case of PEI–C16, this hysteresis is significantly larger (11–20°), this is possibly due to the long fluorinated chain length.

The surface energies decrease with an increasing chain length from values of about 19–20 mN/m (PEI–C4) down to about 8–9 mN/m (PEI–C12 and PEI–C16). It can be seen from Fig. 30 that constantly low values are reached at a chain length of about 12. The values calculated using *n*-decane, *n*-hexadecane and diiodomethane match very well. Their surface tensions cover a relatively large range (23.9 mN/m, *n*-decane to 50.0 mN/m, diiodomethane), but their interactions with the complex surfaces are exclusively dispersive. By contrast, the surface energy values calculated using water as a test liquid are more complicated because of the high dipole moment of water.

The complex surfaces of PEI–C4, PEI–C5 and PEI–C7 are swollen by water and therefore no

Table 5
Dynamic contact angles of the polyethyleneimine perfluorocarboxylate complexes, perfluorinated acids monolayers and fluorinated polymers against *n*-hexadecane ($\gamma_l = 27.6$ mN/m)

Samples	θ_{adv} (°)	θ_{st} (°)	θ_{rec} (°)	$\gamma_{s,adv}$ (mN/m)	$\gamma_{s,st}$ (mN/m)
PEI–C4	50	49	46	19.0	19.3
PEI–C5	64	62	57	14.9	15.5
PEI–C7	70	68	66	13.1	13.7
PEI–C8	71	71	66	12.8	12.8
PEI–C10	79	77	64	10.5	11.0
PEI–C12	82	82	75	9.7	9.7
PEI–C16	83	80	69	9.4	10.8
C10[a]	–	72	–	–	12.5
C12[b]	–	78	–	–	10.8
I-6,6-F8H4[c]	81	75	69	10.0	11.7
F8-St[d]	82	–	60	9.7	–
F8-MA[e]	81	–	71	10.0	–
PTFE[f]	51	–	40	18.7	–

θ_{adv}, θ_{st}, θ_{rec} are advancing, static and receding angles. $\gamma_{s,adv}$ and $\gamma_{s,st}$ are surface energies calculated using the Neumann and Li equation [19], first with static and then receding angles. Reprinted with permission from 2000;16:824 © American Chemical Society [53].

[a] [54].
[b] Refs. [28,29].
[c] [30].
[d] [55].
[e] [56].
[f] [57].

Table 6
Dynamic contact angles of the polyethyleneimine perfluorocarboxylate complexes, perfluorinated acids monolayers and fluorinated polymers against diiodomethane ($\gamma_l = 50.0$ mN/m)

Samples	θ_{adv} (°)	θ_{st} (°)	θ_{rec} (°)	$\gamma_{s,adv}$ (mN/m)	$\gamma_{s,st}$ (mN/m)
PEI–C4	83	81	75	19.8	20.7
PEI–C5	92	92	88	15.6	15.6
PEI–C7	96	96	92	13.8	13.8
PEI–C8	99	98	90	12.6	13.0
PEI–C10	104	104	91	10.5	10.5
PEI–C12	106	103	90	9.8	11.0
PEI–C16	108	107	89	9.1	9.4
C10[a]	–	90	–	–	16.5
C12[b]	–	103	–	–	11.0

θ_{adv}, θ_{st}, θ_{rec} are advancing, static and receding angles. $\gamma_{s,adv}$ and $\gamma_{s,st}$ are surface energies calculated using the Neumann and Li equation [19] first with static and then receding angles. Reprinted with permission from Langmuir 2000;16:824 © American Chemical Society [53].

[a] [54].
[b] Refs. [28,29].

Table 7
Dynamic contact angles of the polyethyleneimine perfluorocarboxylate complexes, perfluorinated acids monolayers and fluorinated polymers against water ($\gamma_l = 72.3$ mN/m)

Samples	θ_{adv} (°)	θ_{st} (°)	θ_{rec} (°)	$\gamma_{s,adv}$ (mN/m)	$\gamma_{s,st}$ (mN/m)
PEI–C8	112	110	103	15.9	17.1
PEI–C10	120	117	105	11.6	13.1
PEI–C12	123	120	109	10.0	11.6
PEI–C16	124	120	100	9.6	11.5
C10[a]	–	102	–	21.8	–
C12[b]	–	103	–	21.2	–
I-6,6-F8H4[c]	121	–	111	11.1	–

θ_{adv}, θ_{st}, θ_{rec} are advancing, static and receding angles. $\gamma_{s,adv}$ and $\gamma_{s,st}$ are surface energies calculated using Eq. (1), first with static and then receding angles. Reprinted with permission from Langmuir 2000;16:824 © American Chemical Society [53].
[a] [54].
[b] Refs. [28,29].
[c] [30].

contact angles could be measured. In the case of PEI–C8, PEI–C10, the surface energies are significantly higher possibly due to a surface reconstruction as described in Section 2.1.5 as well as for fluorinated side-chain ionenes [30]. The surface reconstruction seems to be absent or very much lower for PEI–C12 and PEI–C16. Probably in these cases, the ionic polymer backbone is far enough below the surface to allow the attack of water, at least within the time of the experiments (30 min). The contact angle hysteresis between advancing and receding angles are typically in the order of 10°. This can be caused by small imperfections, e.g. heterogeneity, swelling and penetration by the wetting liquid.

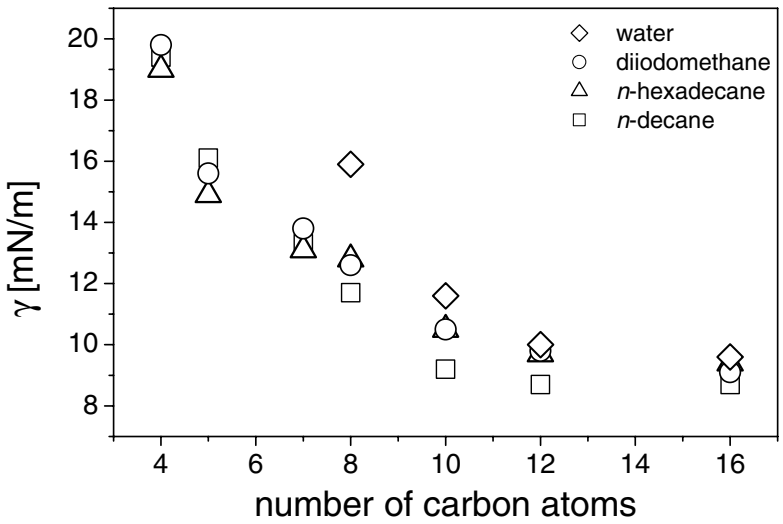

Fig. 30. Surface energies for polyethyleneimine carboxylate complexes are dependent on the chain length of the fluorinated carboxylate moieties. The surface energies were calculated using Neumann and Li equation for water (diamonds), diiodomethane (circles), *n*-hexadecane (triangles), and *n*-decane (squares) as test liquids. Reprinted with permission from Langmuir 2000;16:824 © American Chemical Society [53].

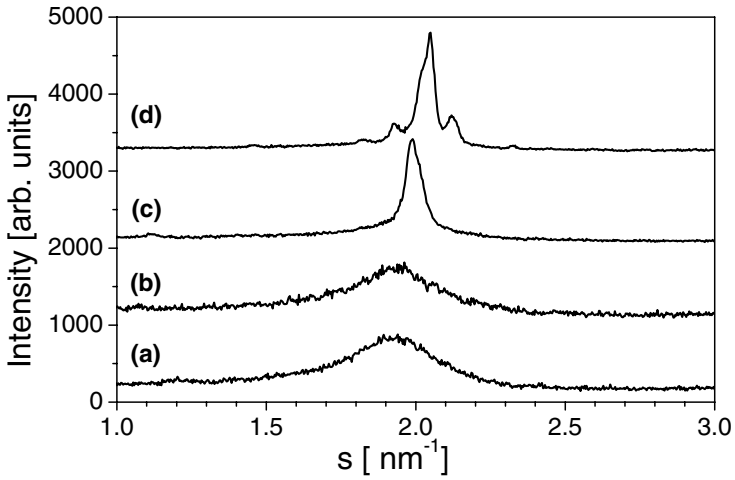

Fig. 31. Wide-angle X-ray scattering diagrams of complex powder of PEI–C8 (a), PEI–C10 (b), PEI–C12 (c) and PEI–C16 (d). Reprinted with permission from Langmuir 2000;16:824 © American Chemical Society [53].

2.1.8.2. Side-chain order. In the wide-angle diagram of the PEI-complexes (Fig. 31), it can be seen that the reflection pattern, and therefore the molecular ordering, changes with the chain length of the perfluorinated acid. For the shorter chain length complexes (PEI–C4 to PEI–C10), only one broad reflection is found (curves (a) and (b) in Fig. 31). Its maximum corresponds to a Bragg spacing of 0.51 nm. The presence of only very broad wide-angle reflections confirms that the complexes PEI–C4, PEI–C5, PEI–C7, PEI–C8, and PEI–C10 are non-crystalline materials. In the wide-angle diagram of PEI–C12, a reflection with a slightly lower Bragg spacing of 0.50 nm, but with a significantly smaller width, is found (Fig. 31(c)). This is indicative of a better lateral ordering of the adjacent fluorinated chains than those present in PEI–C4 to PEI–C10. The simplest molecular arrangement that conforms to the sharper wide-angle reflection of PEI–C12 is that of a parallel alignment of the rod-like perfluoroalkyl chains arranged in a two-dimensional lattice with a rotational disorder and with an average distance of 5.7 nm between the chains. A similar molecular ordering has been reported for a fluorinated poly(α,L-glutamate) with a C12 semifluorinated side-chain [46]. As can be seen in Fig. 31(d), in addition to an intense reflection (Bragg distance of 4.88 nm), further weak reflections are found (Bragg distances of 0.430, 0.472, 0.518, 0.548 nm, respectively) in the wide-angle X-ray scattering curve of PEI–C16. This finding is consistent with a further increase in the molecular order. Probably, the order is three-dimensional with a chain-to-chain distance of 0.56 nm. This is similar to the close packing of fluorinated chains in poly(tetrafluoroethylene) crystals of the hexagonal IV phase with a chain-to-chain distance of 0.57 nm [47].

The presence of side-chain crystallinity of PEI–C16 is confirmed by a first-order transition in the DSC thermogram with a maximum at 163 °C (not shown). This transition is ascribed to the melting of crystalline C16 side-chains. By contrast, no melt transitions are observed in DSC for the other complexes.

2.1.8.3. Nanostructures. An ordering on a length scale in the range 1–10 nm is assumed for the PEI–perfluorocarboxylate complexes. Small-angle X-ray measurements have been performed in order to prove this assumption. The scattering curves of complex powders are shown in Figs. 32 and 33. It can be

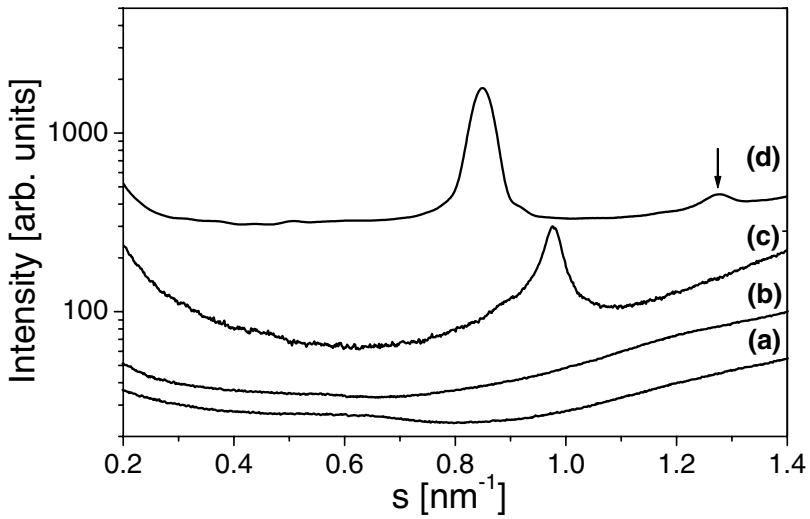

Fig. 32. Small-angle X-ray scattering diagrams of complex powder of PEI–C4 (a), PEI–C5 (b), PEI–C7 (c) and PEI–C8 (d). Reprinted with permission from Langmuir 2000;16:824 © American Chemical Society [53].

seen that no reflections are present for PEI–C4 and PEI–C5 (Fig. 32(a) and (b)) and consequently a regular supramolecular order can be ruled out for these complexes. By contrast, a single reflection at 0.977 nm^{-1} is found for PEI–C7 (Fig. 32(c)) and two for PEI–C8 (Fig. 32(d)) to six for PEI–C16 (Fig. 33(g)) reflections are present in the diagrams of the complexes with the longer chains. These reflections are indicative of the presence of a supramolecular order in the complexes PEI–C7 to PEI–C16.

The increasing number of reflections is indicative of an increasing supramolecular ordering with an increasing chain length of the fluorinated moieties. The reflex maxima positions are summarized in

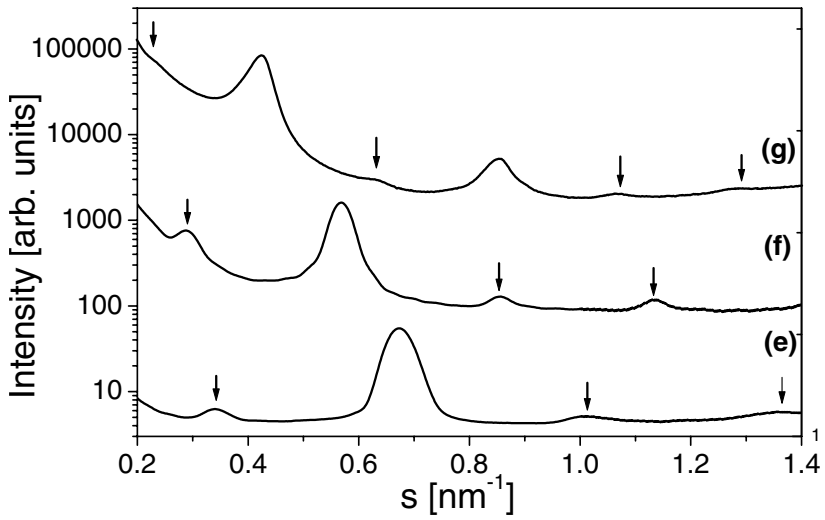

Fig. 33. Small-angle X-ray scattering diagrams of complex powder of PEI–C10 (e), PEI–C12 (f), PEI–C16 (g). Reprinted with permission from Langmuir 2000;16:824 © American Chemical Society [53].

Table 8
Small-angle X-ray diffraction maxima in units of the scattering vector s (nm^{-1}) ($s = 2/\lambda \sin \theta$) and estimates of the observed relative intensities (s, strong; w, weak)

PEI–C7	PEI–C8	PEI–C10	PEI–C12	PEI–C16
0.977s	0.852s	0.342w	0.289w	0.220w
	1.275w	0.672s	0.568s	0.425s
		1.011w	0.860w	0.640w
			1.134w	0.853s
				1.062w
				1.294w

Reprinted with permission from Langmuir 2000;16:824 © American Chemical Society [53].

Table 8. From these the relative reflex positions are determined to be 2.0:3.0 (PEI–C8), 1.0:2.0:3.0 (PEI–C10), 1.0:2.0:3.0:3.9 (PEI–C12), and 1.0:2:0:3.0:4.0:5.0:6.1 (PEI–C16). Therefore, lamellar mesophases are assumed to be present in PEI–C7 to PEI–C16 complexes. In the same sequence form PEI–C7 to PEI–C16, the long period increases with the increasing chain length of the fluorinated chains. The absence of a lamellar structuring in PEI–C4 and PEI–C5 is explained as being due to the chain lengths of perfluorobutanoic and perfluoropentanoic acid, which are not long enough to induce a periodic microphase separation. It is striking that in the scattering curves of PEI–C10, PEI–C12 and PEI–C16, the first reflection is much weaker in intensity than the second.

A possible explanation of the observed ratios and the large differences in the intensities is the presence of two lamellar structures, an α phase and a β phase. Assuming this, the long period of α is about twice as large as the long period of β. The reflections with the indices $l = 2, 4, 6$ of the α modification are found at the same s-values as the reflections with $l = 1, 2, 3$ of the β modification. From the high intensity of the reflection (001) of the β phase (overlapped by reflection (002) of the α phase) compared to the reflection (001) of the α phase it is concluded that the β modification is dominant. The increases of the long periods of the α and β phases as functions of the number of carbon atoms of the carboxylate chains are linear (Fig. 34). The increase of the long period per CF_2-group is determined to be 0.295 ± 0.010 and 0.147 ± 0.002 nm (α and β phase, respectively) from the straight lines in Fig. 34. The length of an axial projection of a CF_2-group in a fluorinated chain is 0.13 nm [58] which gives a thickness of $(n - 1)$ 0.13 nm of fluorinated sheets in a monolayer arrangement and 2 $(n - 2)$ 0.13 nm of fluorinated sheets in a bilayer arrangement of the perfluorinated acids. n is the number of carbon atoms of the acids. It can be seen in Fig. 34 that the theoretical and experimental slopes are in good agreements with a bilayer arrangement of the fluorinated chains in the α phase and a monolayer arrangement in the β phase. Within this model the layer distances of the α phase are 2.92 nm (PEI–C10), 3.46 nm (PEI–C12), and 4.55 nm (PEI–C16). For the shorter chain length, no α phase has been observed. The layer distances of the β phase are 1.02 nm (PEI–C7), 1.17 nm (PEI–C8), 1.49 nm (PEI–C10), 1.76 nm (PEI–C12), and 2.35 nm (PEI–C16).

2.2. Diazosulfonate polymer complexes

In this section, it will be shown that diazosulfonate groups can be integrated as functional moieties in highly ordered nanostructured polyelectrolyte–surfactant complexes. The focus of Section 2.2.1 is on

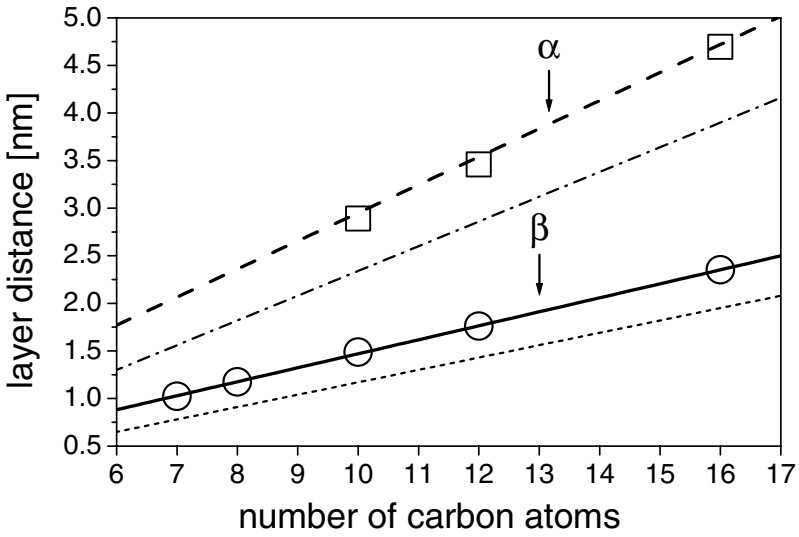

Fig. 34. Layer distances of PEI-complexes are dependent on the number of carbon atoms of the fluorinated acid used for complexation. In the lamellar α phase, the fluorinated chains are arranged in bilayers (squares are measured values, the dashed line is a linear fit, and the dash-dotted line represents the theoretical values of fluorinated bilayer sheets, only). In the lamellar β phase, the fluorinated chains are arranged in monolayers (circles are measured values. The solid line is a linear fit, and the dotted line represents the theoretical values for the fluorinated monolayer sheets). Reprinted with permission from Langmuir 2000;16:824 © American Chemical Society [53].

super-strongly segregated lamellar complexes and that of Section 2.2.2 is on the wetting of ultra-thin films. Water-insoluble complexes are formed by diazosulfonate containing polyelectrolytes and fluorinated cationic surfactants capable of forming low energy surfaces. A fine-tuning of the structures and the surface energies is achieved by varying the composition of the polymer backbone, the charge density and the pH value. It has been shown earlier that polyelectrolytes containing diazosulfonate chromophores are useful for the preparation of solid complexes with non-fluorinated surfactants [59]. The diazosulfonate groups of the polymers act as a functionality that makes the complexes sensitive to light.

2.2.1. Super-strongly segregated lamellar structures [60]

This section reports on complexes of anionic polyelectrolytes which contain diazosulfonate groups and a commercially available fluorinated cationic surfactant (Hoe-L-3658-1). In the experiments, mixing equimolar amounts of polyelectrolyte (Fig. 35, structures (a)–(g)) and fluorinated surfactant resulted in complexes which precipitate immediately. After purification by washing with water, the complexes are dried in vacuum, subsequently soluted in trifluoroethanol and cast into transparent films.

The nature of surfactant chain packing in the complexes is determined by wide-angle X-ray scattering. In the wide-angle X-ray scattering patterns of all complexes, only a broad reflection is found, which corresponded to a Bragg spacing of 0.52 nm. This is attributed to an amorphous packing of fluorinated alkyl chains. This finding is similar to that observed for complexes of cationic copolymers of low charge density with perfluorodecanoic acid but this is in contrast to a complex of poly(diallyldimethylammonium) chloride homopolymer with perfluorodecanoic acid, which is partially crystalline (Section 2.1.3). The absence of crystallinity for the complexes D1a to D1g can probably be

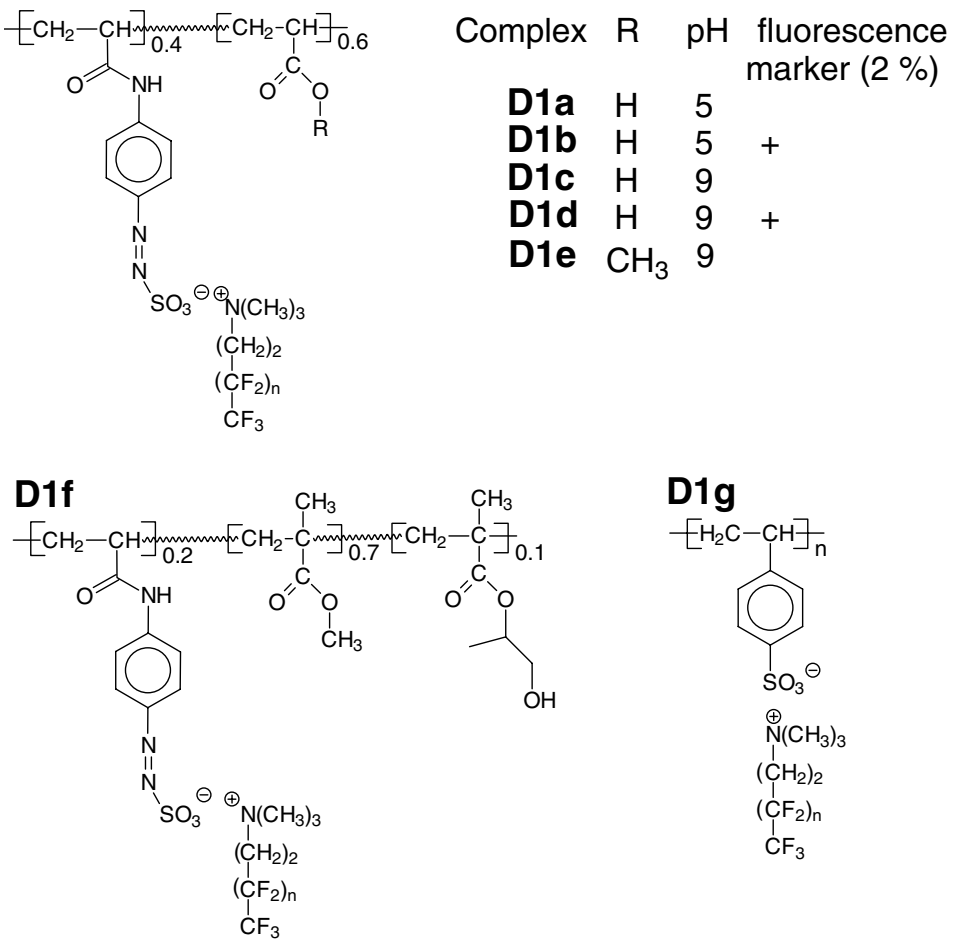

Fig. 35. Complexes of poly[(acrylic acid)-*co*-(acrylamidophenyldiazosulfonate)] (D1a) to (D1e), poly[(acrylamidophenyldiazosulfonate)-*co*-(1-hydroxy-2-methyl-ethyl-methacrylate)-*co*-(methacrylate)] (D1f) and polystyrenesulfonate (D1g). Reprinted with permission from Macromolecules 1999;32:7414 © American Chemical Society [60].

attributed to the relatively short length of the fluorinated chain (C_6F_{13}), which is too short to allow a side-chain analogues crystallinity.

2.2.1.1. Super-strongly segregated lamellar nanostructures. Small-angle X-ray scattering experiments have been carried out in order to study the mesomorphous character of these complexes. The curves for powder and film samples are identical within the range of experimental errors. Typical scattering curves, as found for complex D1a and D1f, are shown in Fig. 36. An intense maximum that confirms the assumption of a microphase-separated system is found in the scattering curves of all complexes. Weak reflections of a second-order are observed in the curves of complexes D1d and D1g, which is indicative of a lamellar structure.

A detailed evaluation of the data has to be carried out for a precise assignment of the phase structure. First, to determine the repeat units, the smearing effect of the Kratky camera system has to be taken into account. To determine the reflex position and its integral width, *b*, the analytical expression of Eq. (1.1)

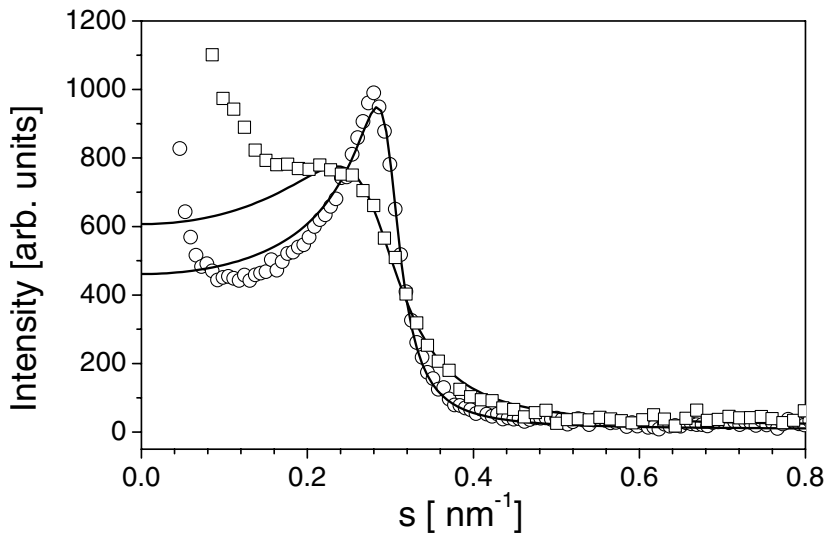

Fig. 36. Small-angle X-ray scattering curve of complex D1a (circles) and D1f (square) and fits according to Eq. (1.1). Reprinted with permission from Macromolecules 1999;32:7414 © American Chemical Society [60].

has been used. This expression is fitted to the Kratky peaks; resulting in s_h and b values of $0.280 < s < 0.333\ nm^{-1}$ and $0.071 < b < 0.190\ nm^{-1}$ (Table 9). It is assumed from the similarity of the values that the complexes are isomorphous to smectic A-like complexes of poly(acrylic acid) and poly(methacrylic acid) with the surfactant Hoe-L-3658-1 described earlier [12].

Additional information concerning these structures have been obtained from the asymptotic decrease of the scattering curve. At larger angles, the scattered intensity decreases with the third power of the scattering vector. This is in accordance with Porod's law (Section 1.4.2). Such a scaling law is a strong indication of a two-phase system with sharp interface boundaries. The main source of error in the range of validity covered by Porod's law is the scattering due to density fluctuations and the widths of the domain boundaries [6]. The linear behavior of the scattering curve in a $s^3J(s)-s^3$ plot (Fig. 37) proves that the only deviation from Porod's law is a three-dimensional homogeneous density fluctuation, which is given by the slope of the straight line. A broader transition or a statistical structuring of the domain

Table 9
Structure parameters determined by small-angle X-ray analysis

Complex	d (nm)	d_1 (nm)	d_2 (nm)	l_p (nm)	S/S_0	s_{max} (nm^{-1})	b (nm^{-1})
A	3.35	1.15	2.20	1.20	1.26	0.299	0.071
B	3.41	1.11	2.30	1.19	1.24	0.293	0.120
C	3.15	1.10	2.05	1.30	1.10	0.317	0.108
D	3.17	1.07	2.10	1.20	1.18	0.315	0.083
E	3.18	1.10	2.08	1.28	1.12	0.314	0.122
F	3.56	–[a]	–[a]	–[a]	–[a]	0.280	0.190
G	2.93	1.00	1.93	1.19	1.11	0.333	0.094

Reprinted with permission from Macromolecules 1999;32:7414 © American Chemical Society [60].
[a] Values cannot be determined due to absence of an asymptotic scaling according to Porod's law.

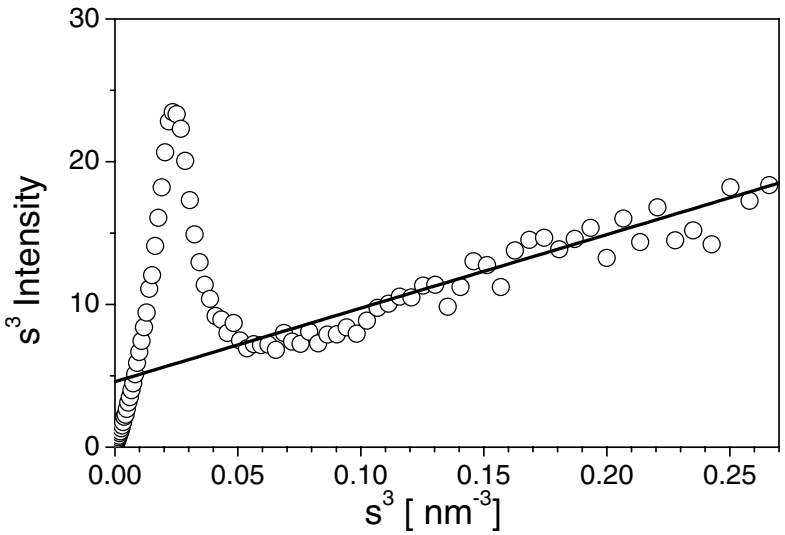

Fig. 37. $s^3J–s^3$ plots of the small-angle X-ray scattering of complex D1a (circles) and their ideal behavior according to Porod's law (solid line). Reprinted with permission from Macromolecules 1999;32:7414 © American Chemical Society [60].

boundary, as typically observed in microphase-separated block copolymers [7], can be excluded. Small deviations from a sharp boundary would indicate a significant deviation from Porod's law (Section 1.4.2). Therefore, it has been concluded that the phase boundaries of the complexes are in the order of 1–2 atomic distances, i.e. the lamellar nanostructure is super-strongly segregated. Using Eq. (1.2) the average chord lengths have been calculated to be in the range from 1.19 to 1.30 nm, which is similar to the polymeric complexes of siloxane surfactants described in Section 2.3.

The simplest structure which is in agreement with these numbers is a microphase-separated model constructed from a smaller ionic phase (polyelectrolyte plus ionic head groups) and a larger non-ionic phase (hydrophobic moieties). The repeat unit of a lamellar system d is given by $d = d_1 + d_2$, where d_1 and d_2 are the thicknesses of the two lamellae. Their values are determined by calculating the interface distribution function $g(r)$ (Section 1.4.3). The interface distribution is computed by the expression (Eq. (1.8)). A model that can describe the statistics of lamellar phases is the lattice model, in which the statistics are described by the distributions $h_1(d_1)$ and $h_2(d)$ of the lamellar thicknesses (Section 1.4.3). In Fig. 38, for example, the interface distribution function computed from the scattering curve of complex D1a and the best fit using the lattice model are plotted. As shown in Table 9, the thicknesses of the ionic layers of complex D1a to D1e are in a narrow range between 1.07 and 1.15 nm, and the thickness of the hydrophobic layers varies between 2.08 and 2.30 nm. The thickness of an ionic layer of complex D1g (1.00 nm) is slightly lower, which is in agreement with its lower ratio of mass per charge. In contrast to the complexes D1a to D1e and D1g, no asymptotic behavior in accordance with Porod's law is found for complex D1f. Consequently, the thicknesses d_1 and d_2 cannot be computed. It must be assumed that the phase separation of D1f is not as strong as that found for the other complexes. A possible reason for this is the lower amount of ionic monomers of D1f (20 mol%). For the other complexes, the amount of ionic monomers (in mol%) is 100 (D1c), 98 (D1d), 40 (D1a and D1e) and 38 (D1b).

In addition to the lamellar thicknesses, the curvature of the interface between ionic and non-ionic

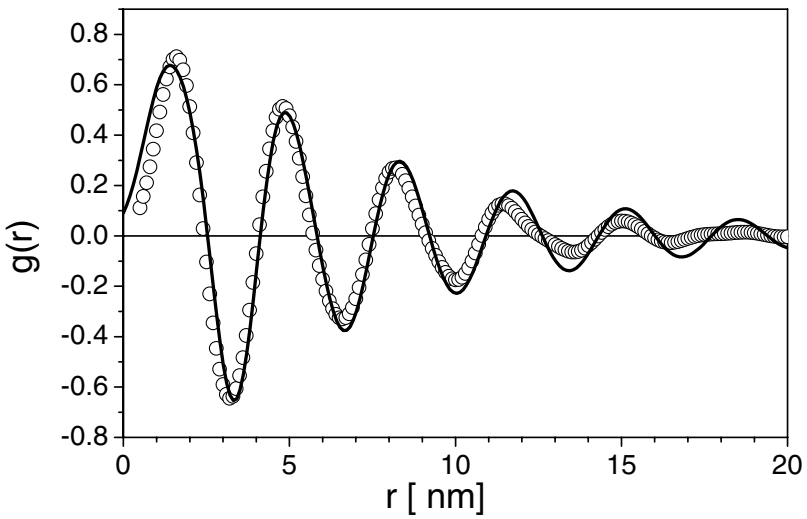

Fig. 38. Interface distribution function computed from the experimental values for complex D1a (circles). The solid line is the theoretical curve with lamellar thicknesses of $d_1 = 1.15$ nm and $d_2 = 2.20$ nm. Reprinted with permission from Macromolecules 1999;32:7414 © American Chemical Society [60].

domains is an important characteristic of the description of the complex morphology. Using Eq. (1.11), the surface ratios S/S_0 are found to be in the range 1.10–1.26 (Table 9). The surface ratios of D1c (1.10), D1e (1.12) and D1g (1.11) are small and nearly identical, and can be seen as essentially flat interface boundaries. The slightly higher value of D1d (1.18) compared to D1c (1.10) may be due to the presence of the fluorescence label (2 mol%), which enhances the waviness to a small extent. The larger values of a (1.26) and b (1.24) are indicative of a significantly higher waviness of the interfaces. These values are similar to those determined by Ruland et al. for the lamellar structures of diblock copolymers. Such undulations are typically due to packing constraints [4].

2.2.1.2. Wetting. Films of the complexes D1a to D1g are prepared by casting 0.1–0.5% (w/w) complex solutions on glass surfaces. The complex solutions are dried at room temperature in dry air resulting in thin transparent coatings with thicknesses of about 500 nm. Dynamic contact angles θ of the test liquids with different surface tensions are measured by means of the sessile drop method [20]. It has been found in particular that all non-polar liquids, which spread readily on uncoated surfaces, show high contact angles on complex-coated surfaces.

The surface free energies have been calculated using the equation of Neumann and Li equation [19]. They range from 11.4 to 16.9 mN/m for all test liquids with surface tensions in the range 18.4–50.0 mN/m (hexane to methylene iodide). Zisman plots (Fig. 39 and Table 10) result in critical surface tensions of 7.5 mN/m (complex D1c) to 13.2 mN/m (complex D1f). These values are significantly lower than those expected for a surface enriched predominantly with CF_2-groups (ca. 18.5 mN/m) and are higher than those expected for an oriented closely packed monolayer of perfluorododecanoic acid (6 mN/m) [26]. Considering the critical surface energy data it seems that the complex surfaces are strongly enriched with loosely packed CF_3-groups. The packing increases along line D1f, D1a, and D1c. This results in a parallel shift of the straight lines (Fig. 39).

The wettability data are also used to determine the dispersion force component of the surface energy

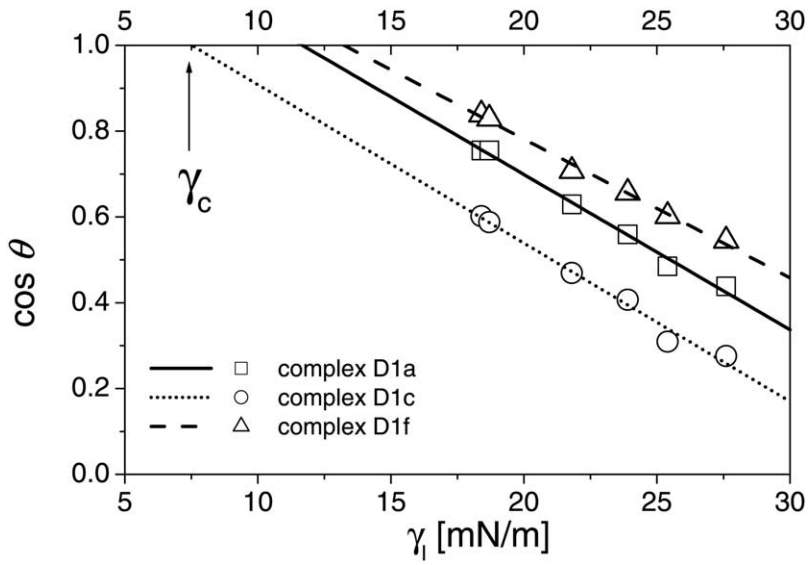

Fig. 39. Zisman plots for complex coated glass surfaces. Points are obtained with (1) hexane, $\gamma_l = 18.4$ mN/m; (2) PDMS, $\gamma_l = 18.7$ mN/m; (3) octane, $\gamma_l = 21.8$ mN/m; (4) decane, $\gamma_l = 23.9$ mN/m; (5) dodecane, $\gamma_l = 25.4$ mN/m; (6) hexadecane, $\gamma_l = 27.6$ mN/m. The critical surface tension of complex D1a is calculated to be 11.7 mN/m by extrapolating a linear fit (solid line) of the cos θ (squares) to cos $\theta = 1$. For complex D1c (circles), a critical surface tension of 7.5 mN/m is determined (dashed line) and for complex D1f (triangles) γ_c is 13.2 mN/m. Advancing contact angles were used for cos θ. Reprinted with permission from Macromolecules 1999;32:7414 © American Chemical Society [60].

γ_s^d by using the Girifalco–Good–Fowkes–Young equation [27–29]. The Girifalco–Good–Fowkes–Young plots are used to show the dynamic advancing contact angle data (Fig. 40). Linear fits result in dispersive surface energies of $\gamma_s^d = 11.4$ mN/m (complex D1c) and 16.2 mN/m (complex D1f). The results are summarized in Table 10. The OH groups present in the polymer may be responsible for the higher surface energy of D1f. From the very similar values found for complex D1a and D1b (14.0 and 14.2 mN/m) as well as for D1c and D1d (11.4 mN/m both), it is concluded that the fluorescence markers (2 mol%) do not affect the surface energy.

A significant effect on the surface energy is found when the complexation is performed in either an

Table 10
Zisman critical surface energies γ_c and the dispersive surface energies γ_s^d according to the Girifalco–Fowkes–Young equation of complex films on glass

Complex	γ_c (mN/m)	γ_s^d (mN/m)
D1a	11.7 ± 1.5	14.0 ± 0.3
D1b	11.9 ± 1.2	14.2 ± 0.4
D1c	7.5 ± 1.9	11.4 ± 0.3
D1d	9.1 ± 1.4	11.4 ± 0.2
D1e	9.2 ± 0.9	12.4 ± 0.3
D1f	13.2 ± 1.4	16.2 ± 0.3
D1g	8.7 ± 1.8	12.3 ± 0.3

Reprinted with permission from Macromolecules 1999;32:7414 © American Chemical Society [60].

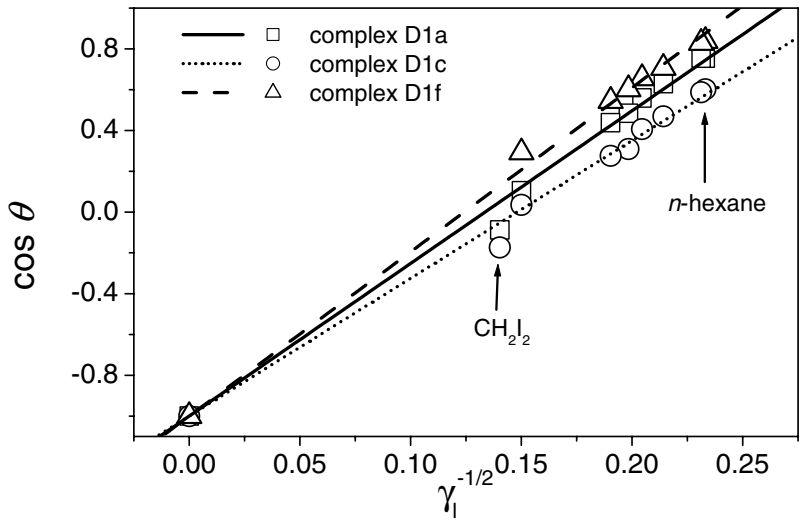

Fig. 40. Girifalco–Good–Fowkes–Young plots for the determination of the dispersive surface energy of complex coated glass surfaces. From left to right the points are values obtained with (1) methylene iodide, $\gamma_l = 50.0$ mN/m; (2) α-bromonaphthalene, $\gamma_l = 44.0$ mN/m; (3) hexadecane, $\gamma_l = 27.6$ mN/m; (4) dodecane, $\gamma_l = 25.4$ mN/m; (5) decane, $\gamma_l = 23.9$ mN/m; (6) octane, $\gamma_l = 21.8$ mN/m; (7) PDMS $\gamma_l = 18.7$ mN/m; (8) hexane $\gamma_l = 18.4$ mN/m. γ_s^d are calculated from the slope to be 14.0 mN/m for complex D1a (squares represent measured angles, the solid line the least square fit), 11.4 mN/m for complex D1c (circles, dotted line), and 16.2 mN/m for complex D1f (triangles, dotted line). Reprinted with permission from Macromolecules 1999;32:7414 © American Chemical Society [60].

acidic or a basic medium. The complexes D1a and D1b are prepared at a pH value of 5, at which the acidic moieties are protonated, the polymeric backbone contains 40 mol% ionic monomers. Under these conditions only the sulfonate groups are complexed by the cationic surfactant, and the 60 mol% carboxylic acid groups, which may enhance the surface energy, remained uncomplexed. Using a pH value of 9, the carboxylic moieties are deprotonated and are able to complex with cations. Under this condition 100% of the monomer units are complexed. The surface energy in these cases (11.4 mN/m) is significantly lower than that determined for D1a and D1b (14.0 mN/m). For the complex of another polymer with 100 mol% ionic monomers (styrenesulfonate) D1g, the surface energy of 12.3 mN/m is close to the low values of D1a and D1b. Here, it is obvious that the lower surface energy values are found for the complexes with the denser packing of the surfactants. Complex D1e, which has 40 mol% ionic monomers, has a significantly lower surface energy than D1a, D1b. This is explained by the presence of the less polar methacrylate group compared to the carboxylate group. The γ_c and γ_s^d values indicate an enrichment of the CF_3-groups on the complex surface.

It is particularly interesting that the contact angles of water (the most polar test liquid with $\gamma_l = 72.7$ mN/m) is only as high as, or smaller than, that of methylene iodide ($\gamma_l = 50.0$ mN/m). The surface energies calculated using the Neumann and Li equation [19] increase in the order of complex D1g (18.2 mN/m), D1c (25.5 mN/m), D1e (29.2 mN/m), D1a (31.1 mN/m) and D1f (50.8 mN/m). The low surface energies determined for non-polar liquids can be reproduced, even when the complex coated surfaces are dried after exposure to water. This indicates a reversible surface reconstruction of the complex surface after it has been in contact with water. It is worth noting that the surface reconstruction of the complex when in contact with water seems to be very fast, as shown by the static constant contact

angle of water which adjusts to an equilibrium within a few seconds. The degree and velocity of surface reconstruction is assumed to be dependent on several factors, such as the number of polar groups within a distance of about 1 nm from the surface and the flexibility of the polymeric backbone, which is affected by the glass transition temperature of the polymer.

2.2.1.3. Thermal properties. The thermal behavior of the complexes has been investigated by DSC. Weak glass transitions can be detected at several degrees above room temperature for the complexes D1c (34 °C), D1d (27 °C), D1e (31 °C), and D1f (30 °C). Above a temperature of 170 °C decomposition sets in, which reaches a maximum decomposition rate at about 200–220 °C. For complexes D1a and D1b, it is not possible to detect glass transitions but their decomposition behavior is essentially the same as that of the other azo containing complexes. The absence of glass transitions is typical for polyelectrolytes.

The highest glass transition, at about 48 °C, has been detected for D1g, a complex, which contains no azo groups. Such a high value may be explained by the higher rigidity of the polystyrenesulfonate backbone compared to that of the polymeric backbones of the other complexes. Below 250 °C no significant decomposition is found. Therefore, the decomposition process is regarded as the thermal decomposition of the diazo groups. This assumption is supported by investigations of the thermal decomposition of diazosulfonate containing polymers and diazosulfonate containing surfactants [61]. No other thermal transitions have been observed in the temperature range from −100 to 170 °C. It is concluded that the thermal stability of the complexes is determined mainly by the stability of the polymer.

2.2.1.4. Optical properties. The significant difference observed in supramolecular structure, surface energies and thermal properties between complex D1a and D1b, and D1c and D1d is assumed to result from different degrees of ionization of the carboxylic groups. This has been proved by IR-measurements. The carbonyl stretch vibration band of complex D1a is located at 1730 cm^{-1}, whereas that of complex D1c at 1689 cm^{-1}. These values can be assigned to the protonated and deprotonated form of the carboxylic acid moieties. Therefore, within the solid complex D1a approximately 40 mol% of the monomer units (SO_3^-) are charged, and approximately 100 mol% in complex D1c. The aromatic ring vibrations can be found at 1598 and 1508 cm^{-1}, the band at 1542 cm^{-1} can be designated to the amidic group. The UV/Vis-spectra for all diazosulfonate containing complexes show an absorption with a maximum at 331 nm referring to the diazo group. Loss of absorption is found after irradiation with UV-light.

The difference between complex D1a, D1b and D1c, D1d in their supramolecular order as well as in their surface properties may partly result from a different organization of the polyelectrolyte chains within the complexes. In order to investigate the polymer chain organization in D1b and D1d, the polymers are copolymerized with 2 mol% *N*-vinylcarbazole, which acts as fluorescence label. At an excitation wavelength of 293 nm, the free monomer shows a structured emission band at 350 nm, whereas for vinylcarbazole homo- and copolymers an additional emission band at lower energies is present due to the formation of excimers. The fluorescence of the polymers is dominated by the emissions of two excimer species: emission centered at ca. 420 nm originates from a conventional 'sandwich like' excited-state dimer, whereas the peak at 370 nm is attributed to luminescence from partially overlapping dimer, which is a 'second' excimer [62]. It can be seen in Fig. 41(a) that the emission spectra of diluted complexes D1b and D1d solutions (5×10^{-3} w/w%) differ significantly. All

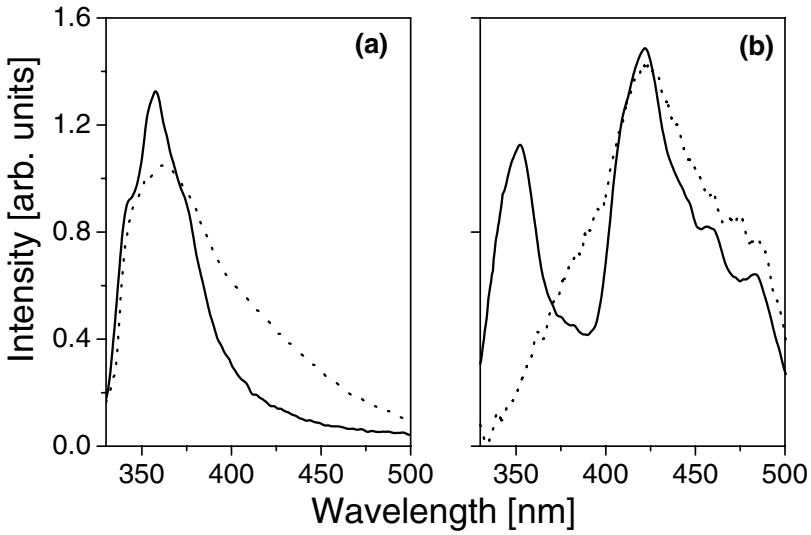

Fig. 41. Steady-state fluorescence spectra of complex D1b (dotted lines) and D1d (solid lines). The measurements are performed on solution (figure left) and on free-standing films (figure right). The excitation wavelength is 293 nm. Reprinted with permission from Macromolecules 1999;32:7414 © American Chemical Society [60].

spectra in Fig. 41 are normalized to equal intensity at 370 nm. The fluorescence intensity at 420 nm is found to be much higher for complex D1b (dotted line) than for complex D1d (solid line). Further, the monomeric emission at about 350 nm is higher for D1d than for D1b. From this it is concluded that in diluted solution the formation of conventional excimers is favored for complex D1b, whereas for complex D1d the uncorrelated, i.e. monomeric emission is predominant. Therefore, at a high degree of complexation (complex D1d, 98 mol%), the tendency to excimer formation is lower than at a lower degree of complexation (complex D1b, 40%). This behavior is found to be even more pronounced for free-standing complex films (Fig. 41(b)). In the spectrum of complex D1b (dotted line), most of the intensity is due to the 'sandwich like' excimer, the monomer emission is negligible. The spectrum of complex D1d (solid line) is even dominated by the emission of the sandwich like excimer, but the emission of the monomer is still present to a considerable degree.

2.2.2. Structures and wetting of ultra-thin films [63]

The subject of this section is the wetting behavior of diazosulfonate polymer complexes in ultra-thin films and on the nanostructures of the films. The diazosulfonate polymers are the same as in Section 2.2.1, but the fluorinated ammonium surfactant has a longer fluorinated tail. The surfactant is commercially available (Fluorad FC135), and the charge density of the polymers is in the range 20–100 mol%. Mixing equimolar amounts of polyelectrolyte (see Fig. 42, structure D2a to D2d) and a fluorinated surfactant resulted in complexes which precipitated immediately. After purification by washing with water, the complexes have been dried in a vacuum, subsequently dissolved in trifluoroethanol and then cast onto wafers to form transparent films.

2.2.2.1. Thermal properties. The thermal behavior of the complexes has been investigated by DSC and TGA. Typical DSC thermograms are shown in Fig. 43. It is found that all the complexes show glass

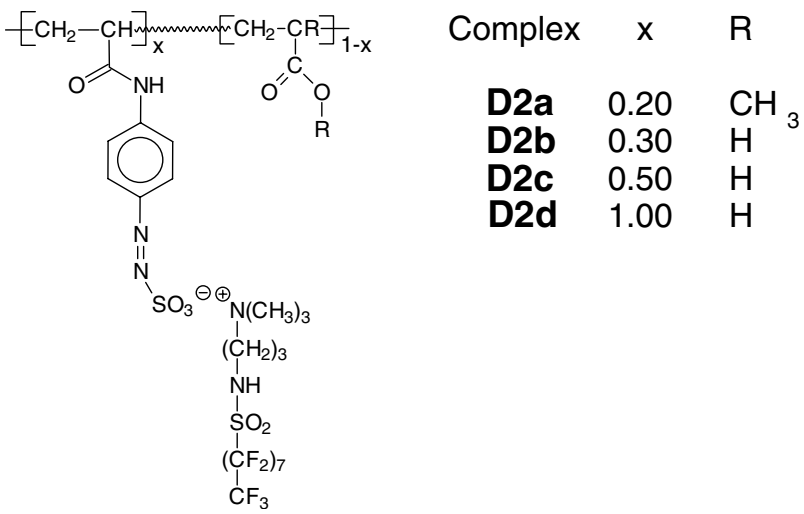

Fig. 42. Complexes of poly[(acrylamidophenyldiazosulfonate)-*co*-(methacrylate)] (D2a) and poly[(acrylic acid)-*co*-(acrylamidophenyldiazosulfonate)] (D2b) to (D2d). Reprinted with permission from Macromolecules 2000;33:5665 © American Chemical Society [63].

transitions at 71 ± 3 °C. This result is somewhat surprising because one would have expected the glass transition to depend on the composition of the polymer. In accordance with the general properties of polyelectrolytes, no glass transitions are found for the pristine diazosulfonate polymers before the decomposition of the diazo groups taken place.

Above the glass transition of all complexes, no further thermal transitions have been detected. From this it is concluded that the complexes are stable up to 180 °C. TGA measurements show that no significant weight loss of any of the complexes can be observed below 180 °C, which confirms the DSC

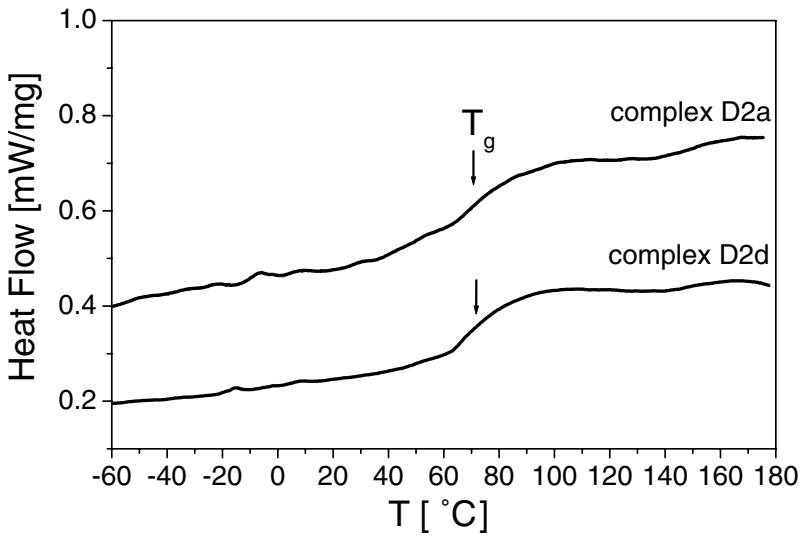

Fig. 43. DSC thermograms of the complexes of D2a and D2d during heating (second heating cycle). Reprinted with permission from Macromolecules 2000;33:5665 © American Chemical Society [63].

results. It is found that significant decomposition starts only above 200 °C, and further, that the maximum decomposition rate of the complexes occurs in the range 230–240 °C. It is found that the complexes with higher charge densities are slightly more stable than the complexes with lower charge densities. The decomposition process is regarded as the thermal decomposition of the azo groups. This assumption is supported by an investigation of the thermal decomposition of diazosulfonate containing polymers and surfactants [61]. Therefore, it is concluded that the thermal stability of the complexes is predominantly determined by the stability of the polymer.

2.2.2.2. Structure in the bulk material. The molecular and supramolecular structures of the complexes have been examined using wide- and small-angle X-ray scattering methods. In the wide-angle scattering diagram of all complexes one single broad peak is found. The peak maxima of all complexes correspond to a Bragg spacing of 0.52 nm. This is attributed to the amorphous packing of the fluorinated chains (C_8F_{17}), in powder, as well as in film samples, which is similar to the packing of shorter chains (C_6F_{13}) in complexes described in Section 2.2.1. By contrast a number of sharp reflections are found in the wide-angle scattering diagram of the pure surfactant which proves that it is a crystalline material. As for different types of complexes described earlier, it is concluded that the crystallization of the surfactant can be strongly reduced as a result of the complexation. The reason for this is that any movement of the surfactant in the complex is accompanied by a rearrangement of the polymeric backbone via the ionic bonds. It is found that a high charge density and a C_9F_{19} chain of the fluorinated moieties is necessary to produce a side-chain crystalline structure in the complex (Section 2.1.3).

The presence of sharp reflections in the small-angle scattering curves of the complexes proves that the charge density of all diazosulfonate polymers is sufficiently high for the formation of periodic nanostructures. This confirms that a charge density of at least 25% is necessary to form ordered complex structures (Section 2.1.3) The width of the most intense reflection is smaller for the complexes of medium charge densities (D2b, D2c) than it is for the complexes with either a low or a high charge density (D2a and D2d). For the former, reflections of a higher order are present with relative positions of 1:2:3. Together with the results from the wide-angle scattering and the DSC, it is concluded that the complexes are isomorphous with a lamellar structure of a smectic A type. From the reflex positions, the long periods have been determined to be 4.4 nm (D2a), 3.8 nm (D2b), 3.9 nm (D2c), and 4.0 nm (D2d). This is in agreement with a multilayer structure of alternating fluorinated and ionic sheets. From the integral width of the first-order reflection, the correlation lengths [64] of the complexes have been determined to be 10 nm (D2a), 30 nm (D2b), 45 nm (D2c), and 11 nm (D2d). Therefore, the complexes D2b and D2c, which have medium charge densities of 30 and 50%, are better ordered than the complexes with the lowest and highest charge densities (D2a and D2d). Probably, the steric constraints within the structure of the complexes are reduced to an optimum at a charge density of about 50 mol% for the diazosulfonate groups.

2.2.2.3. Ultra-thin films. Thin complex films on silicon wafers can be prepared by the spin-coat technique from complex solutions and investigated by X-ray reflectivity. Examples of reflectivity curves of ultra-thin films are shown in Fig. 44. Well-defined double-layer stacks are developed within a few seconds simply as a result of the deposition of droplets of the complex solution.

It has been found that complex D2c, which has the highest correlation length in the bulk material, forms also the best ordered films. In Fig. 44(a), the presence of Kiessig fringes indicate a smooth complex film. A thickness of 4.0 ± 0.5 nm has been calculated from the angular position of the fringes

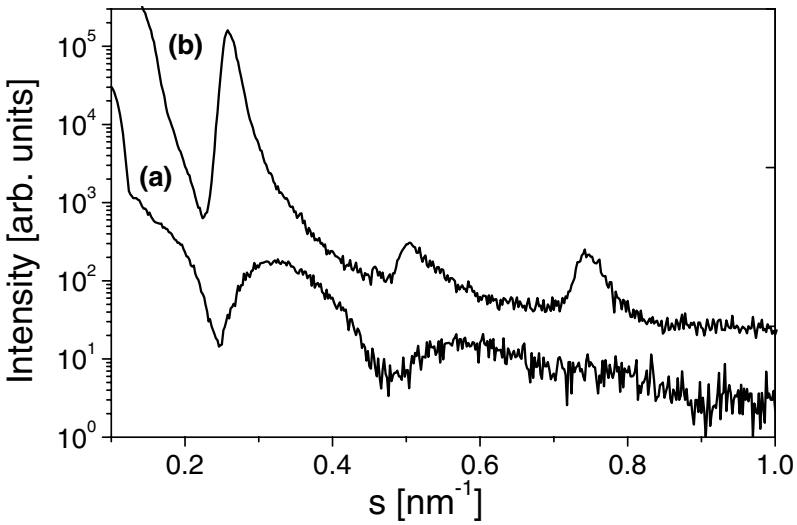

Fig. 44. X-ray reflectivity curves of thin films of complex D2b on silicon wafer surfaces. The film thicknesses are 4 nm (curve a) and about 40 nm (curve b). Reprinted with permission from Macromolecules 2000;33:5665 © American Chemical Society [63].

[51]. In the diagrams of films of larger thickness, three equidistant Bragg peaks appear. The peak positions result in lamellar spacings which are equal, or slightly larger than, that of the complexes in the materials in bulk form. As an example, Fig. 44(b) shows the scattering curve of a film of complex D2c with a lamellar spacing of 4.0 nm and a correlation length between 36 and 40 nm. Because the same nanostructure has been developed in a slow film forming process (solvent casting) and in a fast film forming process (spin coating), it is concluded that the time which is necessary for the formation of the mesophase is shorter than the time necessary for the formation of the films. The latter is in the order of 1 s.

The structure of a film producing a scattering curve such as that in Fig. 44(b) can be explained as consisting of multi-layers aligned parallel to the wafer surface. The macroscopic orientation of complexes to multi-layers with a variability of about two orders of magnitudes in their thicknesses is described in detail in Section 2.1.7. Such polymer multilayers produced in a single-step procedure are of interest in the formation of self-assembled organic multilayer films.

In order to determine the elemental composition at the film surfaces X-ray photo-electron spectroscopic (XPS) measurements are carried out. In this surface spectroscopic experiment, the sample of interest is irradiated with Mg Kα X-rays. The kinetic energy of the emitted photoelectrons are measured. Since the mean free path of the ejected photoelectron controls the analysis depth, an analysis of the outer 5 nm of the polymeric surface can be obtained by changing the angle of the sample surface relative to the collection aperture of the spectrometer. The complex coated silicon wafers are examined using this approach and they are compared with the average complex composition in the bulk material. The results are shown in Table 11. It can be seen there that the fluorine content at the surface of all the complexes is higher than that of the calculated average bulk composition. Furthermore, the fluorine content depends strongly on the take-off angle. The take-off angle is defined as the angle between the sample surface and the detector. At the lower take-off angle of 45°, which corresponds to the lower sampling depth of roughly 3 nm, the detected amount of fluorine increases from 41 to 46 at% in the

Table 11
XPS data for complex coated silicon wafers

Complex	Exit angle	Atom%									
		Experimental					Theory[a]				
		C	F	N	O	S	C	F	N	O	S
D2a	90	45.1	28.6	4.9	17.9	3.5	53.1	20.9	6.2	17.3	2.5
	45	38.2	41.4	4.1	13.4	2.9					
D2b	90	47.0	33.4	5.7	11.8	2.1	46.4	26.3	7.7	16.5	3.1
	45	38.9	43.0	4.6	11.0	2.5					
D2c	90	44.7	33.4	5.7	13.7	2.5	44.8	29.3	8.6	13.8	3.5
	45	39.2	42.4	4.6	11.3	2.5					
D2d	45	37.4	46.2	4.7	9.0	2.7	43.4	32.1	9.4	11.3	3.8

Reprinted with permission from Macromolecules 2000;33:5665 © American Chemical Society [63].
[a] Values represent the bulk composition of a stoichiometric complex.

series from complex D2a to D2d. These values are significantly higher than the average values of the fluorine content of the complexes, which increase from 21 to 32 at%, and indicate an enrichment of the fluorine groups at the complex surfaces.

High-resolution spectra have been collected in the region of the carbon 1s in order to estimate the CF_2/CF_3 ratios. Typical examples for take-off angles of 90 and 45° are given in Fig. 45 for complex D2b. Discrete peaks at binding energies of 292 and 294 eV are assigned to the CF_2 and CF_3 functional groups and show clearly the $(CF_2)_7-CF_3$ chains at the air/complex interface. The ratios of the CF_3 to CF_2 groups are about 0.24 and 0.35 for take-off angles of 90 and 45°, respectively. Both values are significantly higher than the value calculated for the average composition (0.14). This confirms the assumption that the fluorinated chains are oriented towards the air/complex surface. It is found that the polymer

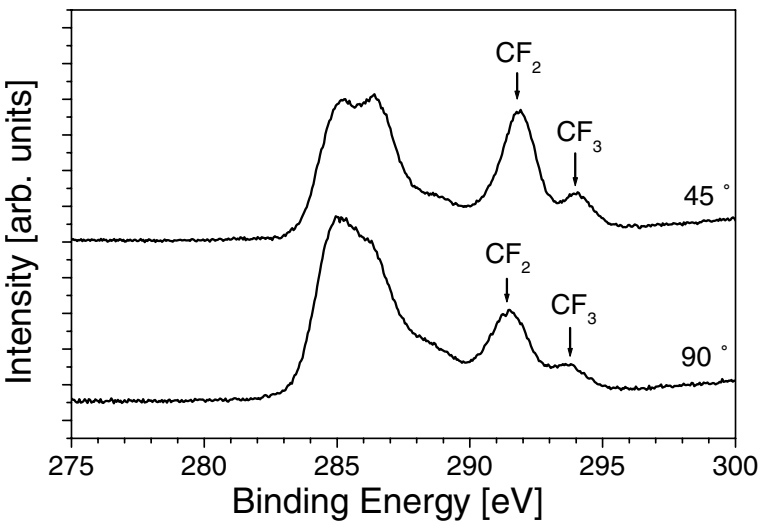

Fig. 45. XPS carbon 1s core-level spectra of complex D2b films on silicon wafer. The take-off angles are 90° (lower curve) and 45° (upper curve). Reprinted with permission from Macromolecules 2000;33:5665 © American Chemical Society [63].

complexes decompose significantly when irradiated with a Mg Kα X-ray in a high vacuum during the XPS measurements. Therefore, it is not possible to perform angle-dependent high-resolution measurements of high accuracy in order to determine the differences of the complexes in respect of their enrichment of CF_3-groups at the surface. The radiation-induced decomposition of fluorinated polymers is well known, for example, in the XPS investigation of perfluorinated polyethers [65]. An indirect method which supplies information about the surface composition is the determination of the surface energy by contact angle measurements.

2.2.2.4. Wetting. Films of the complexes D2a to D2d, prepared by solvent casting and by spin coating, are investigated by using dynamic contact angle measurements [20]. It is found in particular that all non-polar liquids, which spread readily on uncoated surfaces, show high contact angles on complex-coated surfaces. In addition, no significant difference is found between the contact angles of solvent cast films and spin coat films. This observation is in agreement with the fact that the structure formation of the complexes is faster than the film forming process in the procedures used. The surface energies have been calculated using the Neumann and Li equation [19] and range from 10.6 to 13.1 mN/m for the homologue series of alkanes used as test liquids with surface tensions in the range 18.4–27.6 mN/m.

It is found that the complexes with the higher supramolecular ordering (D2b and D2c) possess lower surface energies than the complexes with the lower ordering (D2a and D2d). This is probably due to the influence of the lamellar ordering within the bulk material on the alignment of the CF_3-groups at the air/complex interface. Zisman plots result in critical surface tensions of 6.9 mN/m (complex D2b) to 11.4 mN/m (complex D2d). Together with the X-ray results, the complexes are similar to a smectic A side-chain polymer. By contrast, the fluorinated chains are not bound covalently but ionically. Considering the critical surface energy data and the results from the XPS measurements, it can be concluded that the complex surfaces are strongly enriched with closely packed CF_3-groups.

The wettability data are also used to determine the dispersion force component of the surface energy by using the Girifalco–Good–Fowkes–Young equation [27–29]. Girifalco–Good–Fowkes–Young plots are used to determine γ_s^d values. Linear fits result in dispersive surface energies of $\gamma_s^d = 12.2 \pm 0.1$ mN/m (complex D2a), 11.4 ± 0.2 mN/m (complex D2b), 10.6 ± 0.3 mN/m (complex D2c), 13.1 ± 0.3 mN/m (complex D2d). All results are summarized in Table 12. As shown in the earlier sections, the contact angles of water (the most polar test liquid, with $\gamma_l = 72.7$ mN/m) are relatively low. Again, the surface energies calculated using the Neumann and Li equation [19] are higher for the complexes with the lower degrees of order in the bulk material (39.2 mN/m (D2a) and 32.9 mN/m

Table 12
Zisman critical surface energies γ_c and the dispersive surface energies γ_s^d according to the Girifalco–Fowkes–Young equation of complex films on glass

Complex	γ_c (mN/m)	γ_s^d (mN/m)
D2a	8.9 ± 0.9	12.2 ± 0.1
D2b	6.9 ± 1.2	11.4 ± 0.2
D2c	7.8 ± 1.0	10.6 ± 0.3
D2d	11.4 ± 1.6	13.1 ± 0.3

Reprinted with permission from Macromolecules 2000;33:5665 © American Chemical Society [63].

(D2d)) than for the complexes with the higher degrees of order (23.0 mN/m (D2b) and 24.8 mN/m (D2c)).

The low surface energies determined for non-polar liquids are reproduced, even when the complex coated surfaces are dried after exposure to water. This indicates a reversible surface reconstruction of the complex surface after it has been in contact with water. The surface reconstruction of the complex when in contact with water seems to be very fast as shown by the static constant contact angle of water which adjusts to an equilibrium within a few seconds. The degree and speed of surface reconstruction is assumed to be dependent on several factors, such as the number of polar groups within a distance of about 1 nm from the surface. Taking into account the correlation lengths, there seems to be an optimum at a content of about 30–50 mol% of charged monomers in forming low energy surfaces and in forming ordered structures. Thin coatings of the complexes seem to be promising for the development of surfaces which can be switched irreversibly from ultra-low energy surfaces to a high energy surfaces by using a laser beam.

2.3. Polyelectrolyte–silicon–surfactant complexes [66]

Many silicon compounds are able to reduce the surface energy of materials, which is responsible for many applications. The origins of these unusual and useful properties are closely related to silicons' unique chemistry [67]. Silicon-containing surfactants have been successfully used as auxiliaries in the manufacturing and processing of paints and coatings [68,69]. They are also valuable as surface-active ingredients in the textile and fiber industries, acting as emulsifiers, softeners, etc. [70].

The aggregation behavior of silicon-containing surfactants has been investigated in detail by small-angle neutron and static light scattering, where, for example, hexagonal and lamellar mesophases are found in concentrated aqueous solution [71]. Nothing has yet been reported on the formation of ordered structures, on a nanometer scale, in solid polyelectrolyte–silicon–surfactant complexes. Comparable complexes of fluorine-containing surfactants and polyelectrolytes have been described in Sections 2.1.1–2.2.2.

This section reports on the properties of the complexes PD-Sa and PD-Sb, which are formed using the cationic polyelectrolyte, poly(diallyldimethylammonium chloride) (PD), the anionic surfactants isopropylammonium 6-(trimethylsilyl)-*n*-hexyl sulfate (Sa) and isopropylammonium [3-(1,1,3,3,5,5,5-heptamethyltrisiloxan-1-yl)hexyl-1-sulfate] (Sb). The complex formation is schematically shown in Fig. 46. Polyelectrolyte PD has been chosen because it has already been used successfully for various solid complexes, e.g. with lipids [72], amphiphilic drugs [73], and fluorinated surfactants [12]. The silicon surfactant with only one trimethyl group has been chosen for different reasons. First, salts of sulfatic esters have excellent surfactant properties combined with good hydrolysis stability [74], and second, it is known that the chemical and physical behavior of silicon compounds, e.g. their high flexibility, is different from that of their carbon analogous. The experience with non-silyl-containing complexes can be transferred to silicon-containing surfactants if the influence of silicon is not predominant. Additionally only atoms at, or near, the film/air interface are responsible for the surface energy. A perfect alignment of $(CH_3)_3Si$ groups at the film surface interface results in a surface energy significantly lower than that found for high molecular weight poly(dimethylsiloxane) (24 mN/m) [67]. In principle, one trimethylsilyl moiety at the tail of the surfactant may be enough to form a low-energy surface material. For example, sodium methyl siliconate ($CH_3Si(OH)_2ONa$) is used successfully in the hydrophobizing of walls while maintaining permeability for moisture [75]. The trisiloxanylhexamethyl

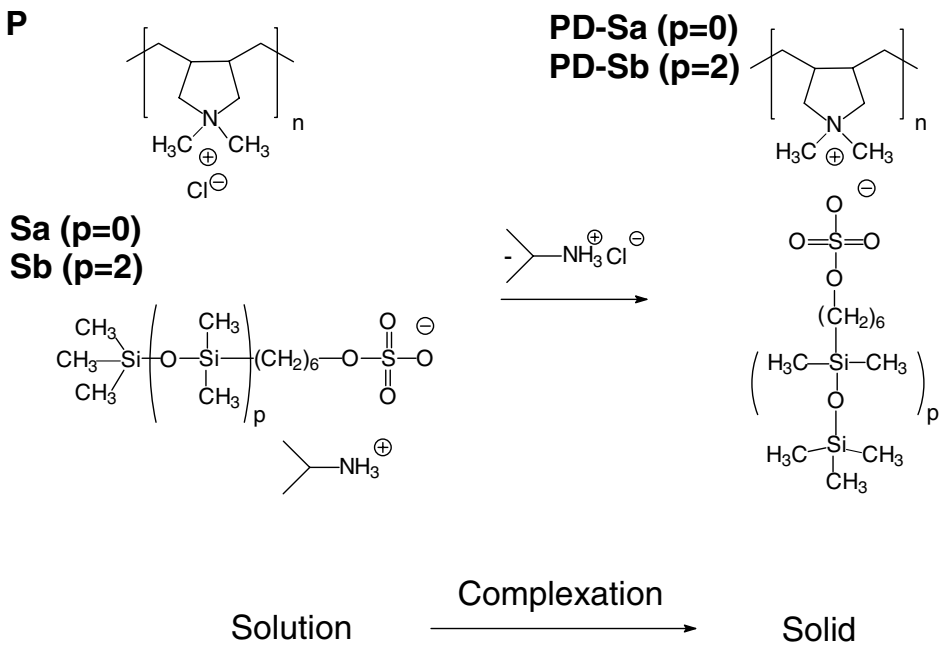

Fig. 46. Sketch of complex formation: (PD) poly(diallyldimethylammonium chloride); (S) isopropylammonium 6-(trimethylsilyl)-*n*-hexyl sulfate ($p = 0$, Sa) isopropylammonium [3-(1,1,3,3,5,5,5-heptamethyltrisiloxan-1-yl)hexyl-1-sulfate] ($p = 2$, Sb); (PD-Sa and PD-Sb) stoichiometric polyelectrolyte–silicon–surfactant complexes. Reprinted with permission from Langmuir 1998;14:6220 © American Chemical Society [66].

sulfate Sb has been synthesized in order to compare the influence of a single silyl group Sa with a trisiloxane in the structure and surface energy of equivalent complexes.

The complexation of PD with Sa and Sb produces the ionic complexes PD-Sa and PD-Sb (Fig. 46). The complexes are processed as transparent and flexible films by solvent casting and spin coating. Free-standing films with thicknesses down to 50 μm are produced by the solvent cast procedure. Because of their physicochemical relationship to the polyelectrolyte–fluorosurfactant complexes, self-assembled structures are expected for the complexes PD-Sa and PD-Sb.

2.3.1. Nanostructures

To study the mesomorphic character of the complexes, small-angle X-ray scattering experiments have been conducted (powder and films). The resulting scattering curves are shown in Fig. 47. In the scattering curves of both complexes, an intense maximum that confirms the assumption of a microphase-separated system is found. The reflex positions and widths revealed further that complex PD-Sb has a larger, less ordered structure than that of PD-Sa. No reflections of a higher order are present, which does not allow the precise assignment of the phase structure. To obtain this information, a more detailed evaluation of the data has to be carried out. For determining the long period, the smearing effect of the camera has to be taken into account (Section 2.2.1.1). To determine the corrected reflex positions s_h and widths b, Eq. (1.1) is used resulting in $d_a = 1/s_a = 2.63$ nm, $d_b = 1/s_b = 3.57$ nm, $b_a = 0.086$ nm^{-1}, and $b_b = 0.140$ nm^{-1} (Fig. 47), where a corresponds to complex PD-Sa and b to complex PD-Sb. The results obtained from the refined evaluation of the X-ray data have been confirmed by molecular modeling calculations.

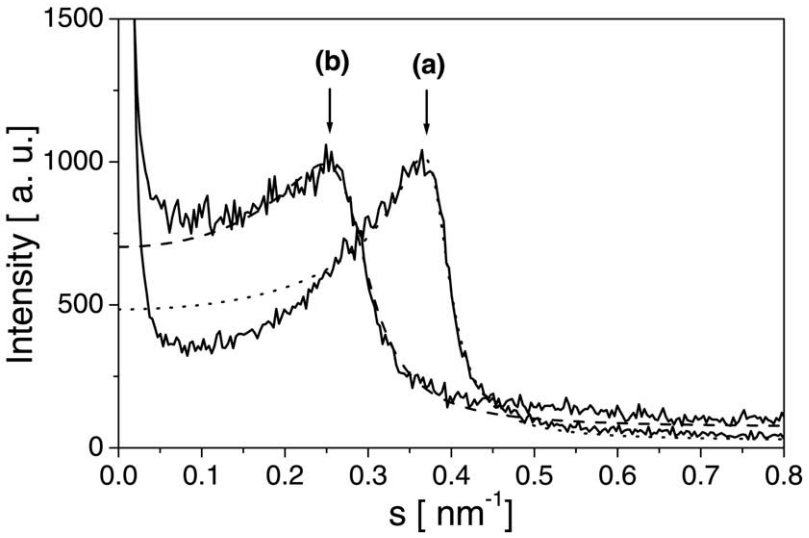

Fig. 47. Small-angle X-ray curves of complexes PD-Sa (a) and PD-Sb (b) and fits according to Eq. (1.1). Reprinted with permission from Langmuir 1998;14:6220 © American Chemical Society [66].

Calculating a lamellar, smectic A-like structure consisting of alternating polyelectrolyte and surfactant layers gives ca. 2.6 nm for PD-Sa and ca. 3.5 nm for PD-Sb. From the s_h and b values, it is assumed that PD-Sa and PD-Sb are isomorphous but that PD-Sb has a larger and less perfect structure than PD-Sa. Further information about the structures is obtained from the asymptotic decrease of the scattering curves. At values in the range 0.5–0.8 nm^{-1}, the scattered intensity decreases with the third power of the scattering vector. This is in accordance with Porod's law (Section 2.2.1.1), a strong

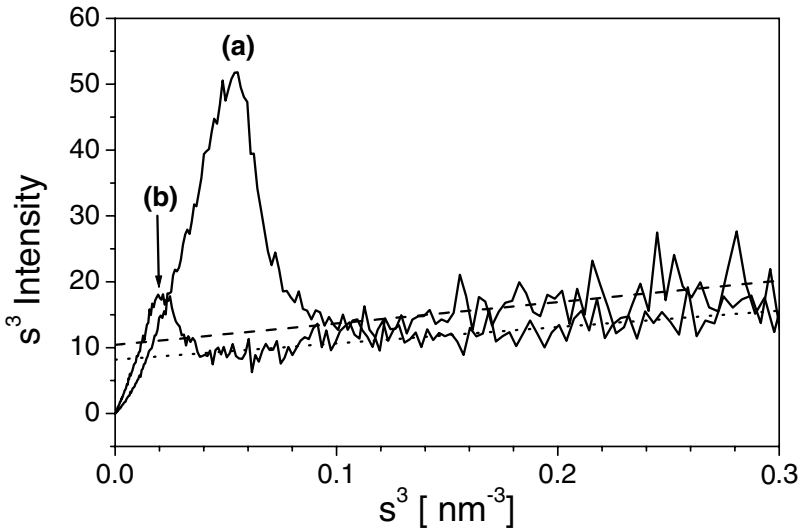

Fig. 48. $s^3J–s^3$ plots of the small-angle X-ray scattering of complexes PD-Sa (a) and PD-Sb (b) and their ideal behavior according to Porod's law for PD-Sa (dashed line) and PD-Sb (dotted line). Reprinted with permission from Langmuir 1998;14:6220 © American Chemical Society [66].

indication for a two-phase system with sharp interface boundaries. The main source of error in the range of validity of Porod's law is the scattering due to density fluctuations and the width of the domain boundary [6]. The linear behavior of the scattering curve in a $s^3J(s)-s^3$ plot (Fig. 48) proves that the only deviation from Porod's law is a three-dimensional homogeneous density fluctuation, which is given by the slope of the straight line. A broader transition of a statistical structuring of the domain boundary, as is typically observed for microphase-separated block copolymers [7] can be excluded. Small deviations from a sharp boundary would lead to strong and significant deviations from Porod's law (Section 1.4.2). Therefore, it is concluded that the phase boundaries of both complexes are in the order of 1 or 2 atomic distances. Using Eq. (1.5), the average chord lengths are calculated to be 1.23 nm (complex PD-Sa) and 1.27 nm (complex PD-Sa). It should be noted that the values for the average cord length of both complexes are similar, although the d values are very different. The complexes are microphase separated, constructed of a smaller ionic phase (polyelectrolyte plus sulfonate head groups) and a larger non-ionic phase (hydrophobic moieties). Regarding the definition of the cord length, it becomes clear that the smaller distances are much more highly weighted than the larger.

From the similarity of both cord lengths, it is concluded that the ionic phases PD-Sa and PD-Sb are nearly identical. In the special case of a lamellar two phase system, the parameter $l_{p>}$ is in the range of $0 \leq l_p \leq (d_1 + d_2)/2 = L/2$ (Section 1.4.3). From experimental analysis the long period of PD-Sa is 2.63 nm; the maximum value, $l_{p,max}$, is theoretically 1.32 nm. Other mesophases show smaller maximum values of l_p. Therefore, although no higher order reflexes are observed in the small-angle X-ray scattering curve, a lamellar mesophase structure and flat lamellar surfaces are assumed to be very likely for complex PD-Sa. This is different from the highly undulated lamellae found for polyelectrolyte–lipid complexes reported previously [72,76].

In contrast to the complexes with undulated surfaces, the silicon surfactant Sa is monodisperse, has a very short alkyl chain, and, in addition to a bulky head group [SO_4^-], also has a large tail group [Si-$(CH_3)_3$]. The same considerations for PD-Sb do not allow an unambiguous determination of the mesophase of this complex. The long period of a lamellar system d is given by $d = d_1 + d_2$, where d_1 and d_2 are the thicknesses of the two lamellae. Their values are determined by calculating the interface distribution function (Section 1.1.3). In Fig. 49 the interface distribution functions computed from the scattering curves and the best fits using the stack model are plotted. For complex PD-Sa, this results in $d = 2.58$ nm, $d_1 = 1.03$ nm, and $d_2 = 1.55$ nm. For complex PD-Sb the values are $d = 3.34$ nm, $d_1 = 1.03$ nm, and $d_2 = 2.31$ nm. The smaller lamellar type for both complexes have the same thickness. These 1.03 nm-thick lamellae are formed by polyelectrolyte chains and sulfate groups, which are very likely to be identically structured for both complexes. The 1.55 nm-thick lamellae of PD-Sa consist of $-(CH_2)_6Si-(CH_3)_3$ groups, and the 2.31 nm-thick lamellae of PD-Sb consist of $-(CH_3)_6Si(CH_3)_2$-$OSi(CH_3)_2OSi(CH_3)_3$ groups. In addition to the lamellar thickness, the curvature of the interface between ionic and non-ionic domains is an important feature for the description of the morphology of the complexes. A measure of the planarity of the interface is obtained from the ratio $S/S_0 = (2d_1d_2)/(dl_p)$ (Section 1.1.3). The surface ratio is calculated to be 1.01 for PD-Sa and to be 1.12 for PD-Sb. It is concluded that the lamellar surface of PD-Sa are perfectly planar (see Fig. 49 inset) and those of PD-SB show only small undulations. Obviously, the surfaces of these complexes show almost no curvature and, therefore, have a low curvature energy. This finding stands in contrast to those polyelectrolyte–lipid complexes, for example, some of whose lamellar mesophases show high undulations with S/S_0 values up to 1.38 [72]. The lipids of the complexes described there have a broad alkyl chain length and head group distribution. Further, Antonietti et al. have shown that the undulations of

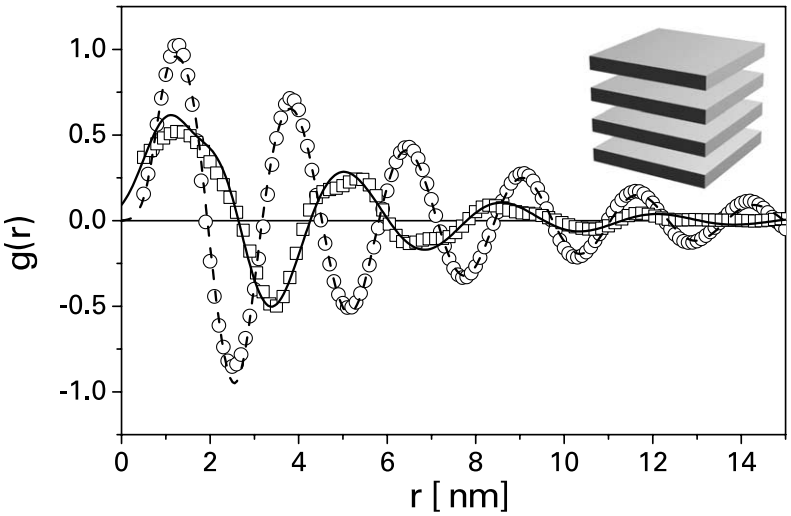

Fig. 49. Interface distribution functions computed from the experimental values for complexes PD-Sa (squares) and PD-Sb (circles). The solid line is the theoretical curve for complex PD-Sa with lamellar thicknesses of $d_1 = 1.03$ nm and $d_2 = 1.55$ nm. The dashed line is the theoretical curve for complex PD-Sb with $d_1 = 1.03$ and $d_2 = 2.31$ nm. The inset shows a model of the layer structure. The polyelectrolyte phase is plotted gray. Surfactant molecules fill the space between the polyelectrolyte phases (not drawn). Reprinted with permission from Langmuir 1998;14:6220 © American Chemical Society [66].

poly(styrenesulfonate)-alkyltrimethylammonium surfactant complexes increase with increasing alkyl chain length. The lack of undulations of complex PD-Sa is attributed to the small hydrophobic chain length and an appropriate charge density of the polyelectrolyte PD. The small undulations of PD-Sb can be explained by the packing disorder of the bulky siloxane groups.

As is frequently observed for solid polyelectrolyte–surfactant complexes, wide-angle X-ray scattering measurements confirm that the complexes PD-Sa and PD-Sb are non-crystalline. The absence of crystallinity in the complexes is confirmed by DSC. The glass transitions are at − 10 °C (PD-Sa) and − 56 °C (PD-Sb). These low glass transitions explain the high flexibility of the films at room temperature. The lower glass transition of PD-Sb compared to PD-Sa is due to the high flexibility of the siloxane segments of the surfactant.

2.3.2. Wetting

Surface energies of films of the complexes PD-Sa and PD-Sb are determined by contact angle measurements with different test liquids: water, glycerol, and methylene iodide. The use of the Neumann and Li equation [19] results in surface energies in the range 36–39 mN/m for complex PD-Sa and 20–22 mN/m for complex PD-Sb (Table 13).

In contrast to the fluorinated complexes of the Sections 2.3.1 liquids with low polarity, e.g. decane, are rapidly adsorbed and spread on surfaces of both complexes. The surface energies calculated for PD-Sb are close to those of the dimethylsiloxane surfaces (21–23 mN/m) [67]. The surface energy of PD-Sb approximates that of a relatively closed packed array of methyl groups. The surface energy of PD-Sa is significantly higher that that of PD-Sb comparable, for example, with values reported for poly(ethylene terephthalate) surfaces (35–36 mN/m) [19]. It has been explained that both complexes are well-ordered

Table 13
List of contact angles of different test liquids on polyelectrolyte–silicon–surfactant complexes

Liquid	γ_l (mN/m)	Complex	Stationary contact angle (°)	γ_s (mN/m)
Water	72.7	PD-Sa	74 ± 7	39
		PD-Sb	105 ± 5	20
Glycerol	63.1	PD-Sa	65 ± 8	38
		PD-Sb	94 ± 4	21
Methylene diiodide		PD-Sa	50 ± 8	36
		PD-Sb	79 ± 6	22

γ_s is the surface energy calculated by using the Neumann and Li equation [19]. Reprinted with permission from Langmuir 1998;14:6220 © American Chemical Society [66].

lamellar structures, but only PD-Sb, for a number of reasons, forms low energy surfaces. Obviously, it is not enough to have intrinsically surface-active pendant groups, but they must also be correctly oriented. It might be that a perfect alignment of trimethylsilyl groups causes problems with a dense packing of methylene groups among silyl and sulfate moieties. Further, the carbon–silicon bond shows a dipole moment with a partially negative charge located at the carbon atom. A perfect alignment of trimethylsilyl groups on the surface results in an energetically unfavorable alignment of the dipoles.

In contrast to the unfavorable packing conditions of PD-Sa, the siloxane backbone of Sb is an extended flexible chain with the available methyl groups adopting the lowest surface energy orientation. It should be stressed that the surfaces of the complexes PD-Sa and PD-Sb show a tendency to swell when in contact with water. This phenomenon is commonly known for poly(dimethylsiloxane) coatings. A surface energy of about 24 mN/m is found only for annealed poly(dimethylsiloxane). Without annealing the surface energies are significantly higher [67]. The flexibility of the siloxane chains allows water molecules to penetrate the film. The heat treatment may cross-link molecules in the film so that the methyl groups cannot reorient themselves when in contact with water. Therefore, effective silicon water-repellent coatings are cross-linked. The decomposition of the PD backbone at higher temperatures makes it impossible to adopt this common heat treatment for the complexes PD-Sa and PD-Sb.

2.4. *Polysiloxane–fluorosurfactant complexes [77]*

In Section 2.1 a strategy for preparing polyelectrolyte–surfactant complexes with fluorinated surfactants on the basis of self-organization is described. Here, it will be shown that the self-assembly concept can be expanded to functionalized polysiloxanes complexed with fluorinated surfactants. A commercially available polysiloxane is complexed with perfluorododecanoic acid resulting in a rubber-like material with surface energies as low as the lowest values encountered up to date. Further, the cross-linking of the complex is greatly enhanced without the need of an additional catalyst.

An effective strategy to reduce the surface energy effectively is the fluorination of siloxanes. Critical surface energies of about 15 mN/m have been found [78]. In a number of patents the preparation of oil-repellent materials using perfluoroalkyl groups covalently bonded to the polysiloxane backbone has been described [79]. Such polymers have a wide range of applications, from textile applications to non-toxic anti-fouling coatings. At present toxic anti-fouling systems are in use but, in situations where the

use of biocides is restricted, silicone elastomeric coatings are accepted as a viable alternative to traditional anti-fouling treatment [80,81].

In view of present political demands [82], effective non-toxic anti-fouling coatings will play a technologically key role in the near future, especially for the protection of ship hulls. An important factor which influences the performance and effectiveness of such silicone coatings is their surface energy. For example, measurement of liquid barnacle repellent indicates that coatings with a surface free energy lower than 12 mN/m are required to prevent attachment [83]. This value is very much lower than that found for standard low energy surfaces made of polytetrafluoroethylene (19 mN/m) [84] or high molecular weight polysiloxanes (24 mN/m) [67]. Only surfaces highly enriched with CF_3-groups can achieve such surface energies.

2.4.1. Wetting

To prepare water-stable ultra-low energy surfaces an amino-functionalized polydimethylsiloxane (PDMS) is used for complexation (Fig. 50). PDMS is a commercially available silicone oil, widely used to give textile fabrics a softer texture [85]. For a good adhesion of PDMS on a textile fabric, about 0.6–2.4 mol% of its monomer units are functionalized with aminoethyl aminopropyl groups. The polysiloxane is end capped with hydroxyl functions by which it can be condensed. For complexation, perfluorododecanoic acid, dissolved in a 2-butanol/methanol mixture, is added to PDMS, resulting in a transparent complex solution. To reduce the viscosity of the polysiloxane and for the homogeneity of the mixture, the PDMS is diluted with hexane. By removing the solvent in a vacuum, highly viscous films with smooth surfaces are formed.

At elevated temperatures, in the range from 120 to 200 °C, the films are cross-linked. To be sure that traces of weakly bound acid are removed, the films are immersed in large volumes of water for 24 h. Then, dynamic contact angles, θ of test liquids with different surface tensions are measured by means of the sessile drop method [20]. Data are given for complexation degrees of 100, 50 and 0%, which correspond to the ratios of amino to carboxylic acid groups of 1:1, 1:0.5 and 1:0 (Table 14). Surfaces of the pure polysiloxane are hydrophobic ($\theta = 98°$) but not oleophobic, i.e. decane and dodecane spread on the polysiloxane surface. By contrast, with increasing fluorine content, the complex surfaces become

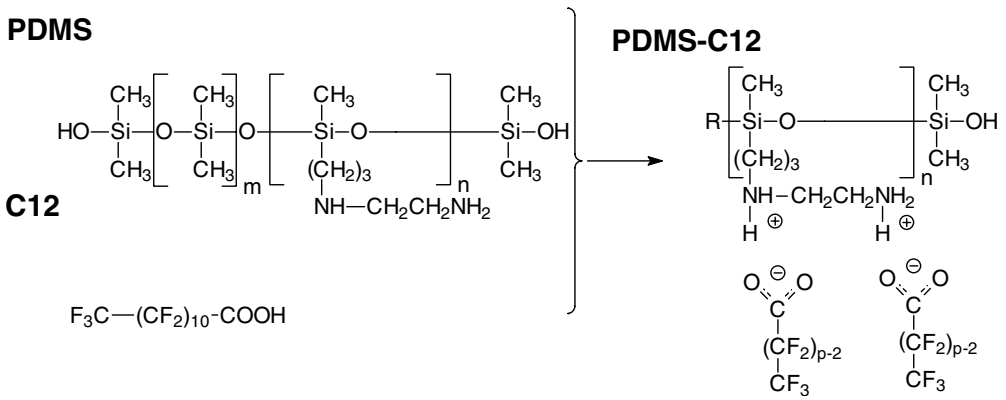

Fig. 50. Sketch of complex formation: (PDMS) amino-functionalized polysiloxane with hydroxyl end groups. The monomers of 0.6 mol% contain aminoethyl aminopropyl groups; (C12) perfluorododecanoic acid; (PDMS–C12) stoichiometric polysiloxane–surfactant complex. Reprinted with permission from J Mater Chem 2001;11:381 © The Royal Society of Chemistry [77].

Table 14
Contact angles of different test liquids of WR1100-C12 film cured for 12 h at 125 °C

Complexation degree		0	50%				100%
Fluorine content (w/w)		0%	4.58%				8.76%
Storage condition		Water	Water	SDS	Methanol	NaCl	Water
Test liquid	γ_l (mN/m)	θ (γ_s) (°) (mN/m)	θ (γ_s) (°) (mN/m)	θ (γ_s) (°) (mN/m)	θ (γ_s) (°) (mN/m)	θ (γ_s) (°) (mN/m)	θ (γ_s) (°) (mN/m)
Decane	23.9	0	75 (9.9)	70 (11.2)	61 (13.5)	69 (11.2)	78 (9.2)
Dodecane	25.4	0	79 (9.6)	75 (10.6)	69 (12.2)	73 (11.2)	82 (8.8)
Hexadecane	27.6	19 (26.3)	84 (9.2)	83 (9.4)	80 (10.2)	76 (11.4)	85 (8.9)
CH_2I_2	50.0	71 (25.5)	115 (6.7)	107 (9.4)	103 (11.0)	107 (9.4)	114 (7.0)
Water	72.7	98 (24.3)	130 (6.8)	127 (8.1)	122 (10.5)	125 (9.1)	131 (6.4)
Surface energy component γ_s^d (mN/m)		–	9.0 ± 0.3	9.9 ± 0.5	11.5 ± 0.9	10.8 ± 0.1	8.4 ± 0.1

Film thickness is 1 mm. The ratio of amino functions to carboxylic groups is 1:0, 1:0.5 and 1:1. Reprinted with permission from J Mater Chem 2001;11:381 © The Royal Society of Chemistry [77]. The error of measurement for the advancing contact angles θ is about 1°. The surface energies γ_s are calculated from the advancing contact angles using the Neumann and Li equation [19].

more hydrophobic and reach a maximum of water- and oil-repellency at a complexation degree of about 50%. It can be seen that the contact angles of water are 130° for a complexation degree of 50% and 131° for 100%. The corresponding values of hexadecane are 84 and 85°, those for decane are 75 and 78°. For an adsorbed monolayer of perfluorododecanoic acid Zisman reported values of 105° for water (which is erratic because of dissolution) 78° for hexadecane and 70° for decane. Obviously, the contact angles of the different liquids on complex surfaces are larger than on the corresponding monolayer surfaces.

To be sure that the high contact angles found for complex PDMS-C12 surfaces are not due to roughness, the surfaces are investigated by scanning electron microscopy. It is found that all polysiloxane complex surfaces are very smooth on length scales in the range from several millimeters down to values lower than a micrometer. Therefore, roughness can be excluded as being responsible for the high contact angles of the complex surfaces, and dynamic contact angles are considered meaningful as a measure of the surface energy. The surface energies are calculated using the Neumann and Li equation [19] (Table 14). The values, as calculated for the different test liquids, range between 6.8 and 9.9 mN/m for a complexation degree of 50 and 100%, which is very much lower than that of the non-complexed polysiloxane (24.3–26.3 mN/m). Second, using the procedure introduced by Zisman [26], an extremely low critical surface tensions of about 6 mN/m is found for a complexation degree of 50% as well as that for 100%. These values are determined after an immersion time of 24 h in water to be sure that any slightly adsorbed acid have been removed. The Girifalco–Good–Fowkes–Young equation [27–29] is used to determine the dispersion force component of the surface energy, γ_s^d. Nearly identically low values are determined for complexation degrees of 50% ($\gamma_s^d = 9.0$ mN/m) and for 100% (8.4 mN/m). This may be interpreted as a saturation of the complex surface by CF_3-groups even at a complexation degree of 50%.

As a test of the complex stability, the complex surfaces are immersed, while stirring, for 24 h in different solvents of practical relevance: 1% aqueous surfactant solution (sodium dodecyl sulfate), in methanol and in 3% aqueous sodium chloride solution. The latter has an ionic strength about equal to that of seawater. The contact angles after immersion in surfactant and salt solution are only slightly reduced compared to that of the pristine surfaces. For the complex surface stored in methanol solution a larger reduction of contact angles is found. But compared with the non-complexed silicon, the contact angles are strongly enhanced. The surface energies using the Neumann and Li equation [19] are in the range between 8.1 and 13.5 mN/m (Table 14). Values of γ_s^d range between 9.9 and 11.5 mN/m. From the low surface energy values, it is concluded that the complex surfaces are still highly enriched with CF_3-groups after immersion. Neither surfactant nor salt solution removes the perfluorododecanoic acid from the complex. Methanol is able to detach minor amounts of the fluorinated acid (Fig. 51). This relatively good stability against solvents is an important advantage of the complex compared to surfaces of perfluorododecanoic acid on platinum. When in contact with water, films of non-complexed perfluorododecanoic acid are dissolved readily [26]. In contrast films of PDMS-C12 are stable enough to withstand even polar solvents.

The sensitivity of contact angles to the chemical composition of PDMS-C12 extends to only a few atomic layers on and near the surface, with polar liquids showing a greater sensing depth than non-polar liquids [38]. In order to measure the surface-near element composition XPS measurements have been carried out. The analysis depth of this method is less than 5 nm for a low take-off angle (20°). It has been found within this surface-near region, that the element composition deviates considerably from the average composition of the complex. A remarkable excess of fluorine at the surface has been detected

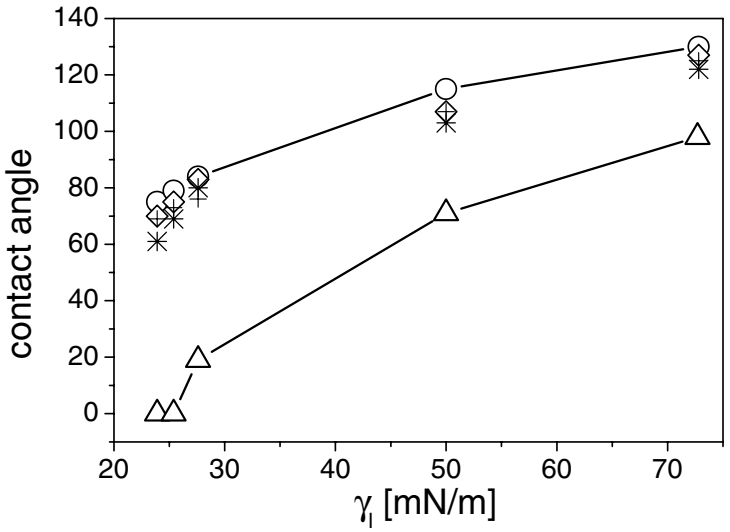

Fig. 51. Advancing contact angles of various kinds of liquid on cross-linked polysiloxane surfaces plotted against the surface tension γ_l of the liquids. From left to right points are values obtained with (1) decane, $\gamma_l = 23.9$ mN/m; (2) dodecane, $\gamma_l = 25.4$ mN/m; (3) hexadecane, $\gamma_l = 27.6$ mN/m; (4) methylene iodide, $\gamma_l = 50.0$ mN/m; (5) water, $\gamma_l = 72.7$ mN/m. Contact angles are shown for a cross-linked complex with a complexation degree of 50% after immersion in water (circles), sodium dodecyl sulfate solution (diamonds), sodium chloride solution (crosses) and methanol (stars). For comparison, the values of the non-complexed polysiloxane are given (triangles). Reprinted with permission from J Mater Chem 2001;11:381 © The Royal Society of Chemistry [77].

with a relative atomic amount of 32.4%, which is a 5.2-fold above the bulk level, which is 6.2% of the total. Similarly high fluorine enrichments at polymer surfaces have been recently reported for carbon containing backbone polymers [86]. Because the depth of XPS analysis is larger than the length of the fluorinated chain (ca. 1.5 nm), even for a theoretical densely packed perfluorododecanoate monolayer at the surface, nitrogen and silicon are found. The surface-near atomic concentrations of nitrogen and silicon are 2.0 and 11.4%, respectively, whereas the corresponding values for the bulk composition are 0.5 and 22.1%. The higher nitrogen content found in the surface-near region is consistent with the complex structure, i.e. the migration of fluorinated chains to the surface is accompanied by the movement of an equimolar amount of ammonium carboxylate ion pairs. Obviously, the predominant part of the ions is not located directly on the surface, otherwise much lower contact angles than the ones observed would be found. As expected, the enrichment in fluorine at the surface is accompanied by a decrease of silicone.

2.4.2. Cross-linking

The cross-linking of the complexes to films with rubber-like properties has been performed without catalysts. Cross-linking of the complex could even be carried out at a temperature where no significant cross-linking is observed for the pure polysiloxane (125 °C). Further, non-stoichiometric complexes contain free amino functions that cross-link faster than stoichiometric or over-complexed PDMS-C12. From this it can be concluded that cross-linking is not only due to the addition of acid.

An optimum amount of perfluorododecanoic acid for a high reaction rate of cross-linking is found to be at a complexation degree of about 50%. In order to determine quantitatively the reaction rate of cross-linking, time-dependent isochronal dynamic-mechanical measurements at constant temperatures are carried out. As shown in Fig. 52 (dotted line), the shear modulus of the non-complexed polysiloxane increases only slowly at 125 °C. After 7×10^4 s the value of the sheer modulus is as low as 3×10^3 Pa. By contrast, in the presence of 2% dibutyltin dilaurate, an effective cross-linking catalyst, the modulus increases steeply within the first 0.5×10^4 s due to a high cross-linking rate (Fig. 52, dashed line). A constant modulus of 1.4×10^5 Pa is reached within about 2×10^4 s. The modulus of the complexed polysiloxanes shows a similar high cross-linking reaction rate as found for the heavy metal catalyst (Fig. 52, solid line). The modulus of the complex increases steeply within the first 10^4 s, levels off and reaches a constant value of about 1.2×10^5 Pa within 3×10^4 s. Although not as good as heavy metal compounds, the ammonium perfluorododecanoate moieties can be considered as effective catalytic entities for cross-linking.

3. Optically functionalized complexes

The nanostructures and the optical properties of self-assembled complexes are described in this section. These are in particular the fluorescence and the electroluminescence of complexes that contain polyelectrolytes with a conjugated backbone such as poly(*p*-phenylene)s (PPP) and poly(*p*-phenyleneethynylene)s (PPE). Section 3.1 contains a description of a mesomorphous columnar complex with interesting fluorescent properties, which are prepared from a rigid-rod-like polyelectrolyte and a fluorinated surfactant. Section 3.2 describes the random layer nanostructure and optical properties of a highly fluorescent PPE complex. In Section 3.3 lamellar structured complexes of PPE will be

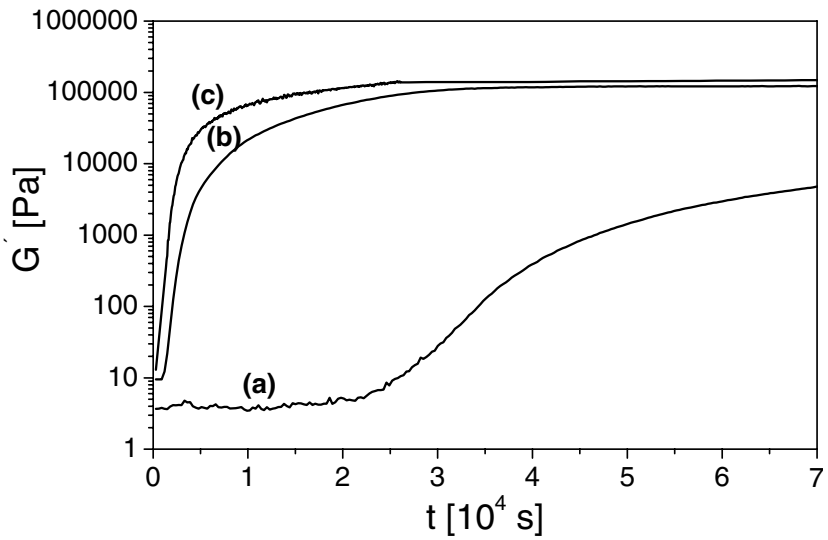

Fig. 52. Time-dependent isochronal shear modulus of amino-functionalized polysiloxane at $T = 125$ °C. The moduli rise due to cross-linking reactions. The modulus of a non-complexed amino-functionalized polysiloxane (curve, a) rises slowly. At the end of the experimental time (7×10^4 s), no plateau is reached. The modulus of a complexed polysiloxane with a complexation degree of 50% (curve b), increases steeply within 10^4 s and reaches a constant value of 1.2×10^5 Pa at about 4×10^4 s. For comparison of the cross-linking rate an effective cross-linking catalyst, dibutyltin dilaurate (2% w/w), is used for the non-complexed polysiloxane. Then the modulus increases steeply within 0.5×10^4 s and reaches a constant value of 1.4×10^5 Pa at about 2×10^5 s (curve c). The frequency of measurements was 1 Hz. Reprinted with permission from J Mater Chem 2001;11:381 © The Royal Society of Chemistry [77].

described and it will be demonstrated that the optical properties of single-layer light emitting diodes (LEDs) of the PPE complexes depend on the nature of the counter ions.

3.1. Rigid-rod complex [87]

Substituted rigid-rod-like polymers with conjugated backbones are interesting building blocks for photonic devices. They facilitate the control of microscopic order as well as a predictable and defined molecular alignment [88]. Poly- and oligo(*p*-phenylene)s are typical representatives of this class of molecule. Blue photoluminescence with a quantum yield of 30% in the solid state is the reason for using *p*-phenylenes in organic LEDs [89–91]. There have been numerous studies dedicated to trying to understand the electronic properties of these highly luminescent materials [92,93]. Theoretical and experimental findings on short-chain model compounds in the solid state show that the planarity of *p*-phenylenes, and therefore the optical properties, are affected by hydrostatic pressure and temperature [94]. The orientation and diffusion dynamics as well as the aggregation behavior of poly(*p*-phenylene)s and their dependence on concentrations and the amount of added salt have been investigated in detail by Wegner et al. [95–97]. It has been shown that ultra-thin films made of poly(*p*-phenylene)s display a complicated dependence on the underlying substrate, the degree of polymerization and the preparation conditions [98]. Further, negatively charged poly(*p*-phenylene)s with hydrophobic moieties show a complex association behavior in solution which depends on their hydrophobic hydrophilic balance [99].

The structures obtained are considered to represent the behavior of biogenic materials with respect to the formation of well-defined superstructures.

The complexation of the cationic poly(*p*-phenylene) PPP with perfluoro-1-octane sulfonate F8 is performed in aqueous solution resulting in the polymeric complex PPP–F8, which is obtained as a yellow-brownish precipitate. A schematic view is given in Fig. 53.

Films of PPP–F8 are prepared from complex solution in methanol by the common solvent casting procedure [100]. Their structure is investigated by wide- and small-angle X-ray scattering. A number of sharp reflections can be seen in the wide-angle diagram of F8, which is a highly crystalline compound,

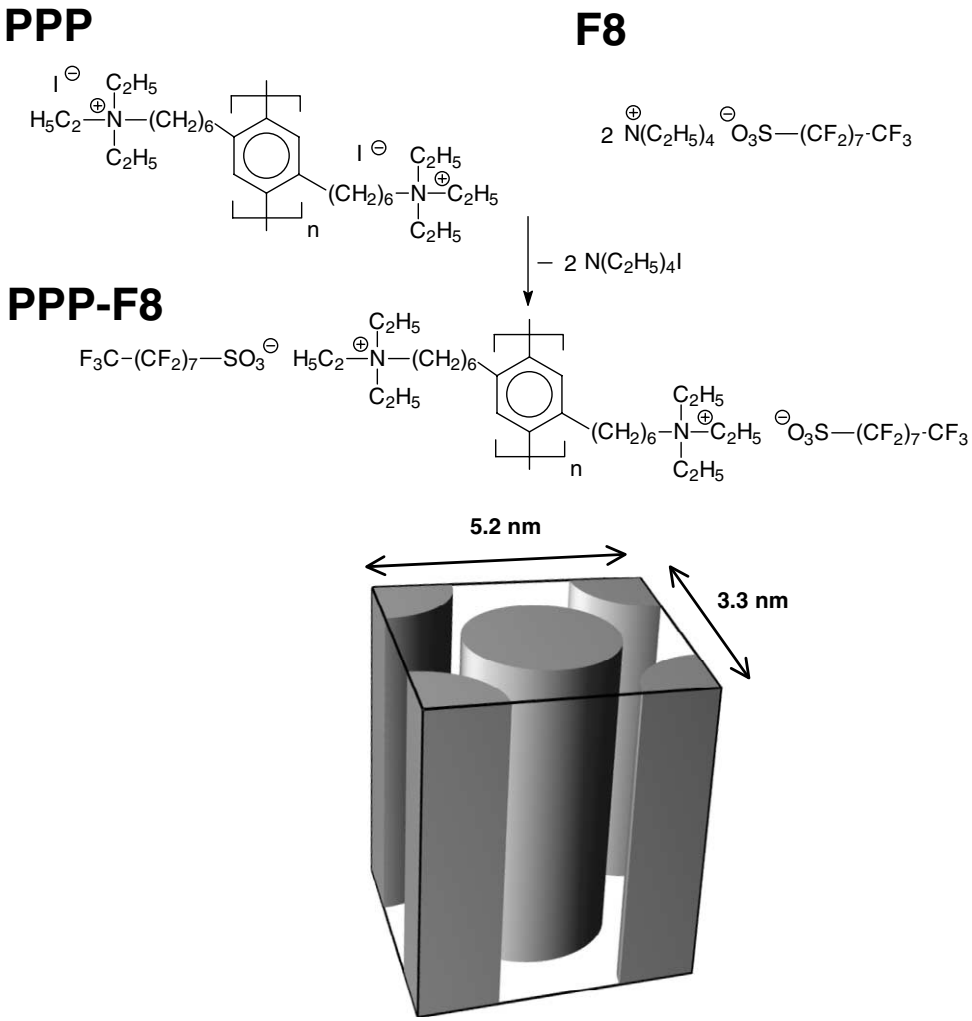

Fig. 53. Complex formation: (PPP) cationic poly(*p*-phenylene) as iodide; (F8) perfluoro-1-octane sulfonic acid tetraethylammonium salt; (PPP–F8) stoichiometric complex. The degree of polymerization is $P_n = 11$. The lower sketch shows a model of the proposed complex structure, which contains two columns per unit cell ordered in a centered two-dimensional unit cell. The columns are formed by strands of poly(*p*-phenylene) molecules which are embedded in an amorphous matrix of fluorinated alkyl chains (not drawn). Reprinted with permission from Macromolecules 2000;33:2124 © American Chemical Society [87].

while no sharp reflections are present in those of PPP or PPP–F8. This proves that neither PPP nor PPP–F8 is partially crystalline materials. The broad reflection centered at 2 nm^{-1} in the diagram of PPP–F8 is interpreted as resulting from the scattering of the fluorinated chains with a short-range order and with an average chain-to-chain distance of about 0.5 nm [21].

PPP–F8 is ordered on a length scale of several nanometers. This is confirmed by small-angle X-ray scattering measurements of the solid sample. In Fig. 54 it can be seen that a number of reflections are present in the small-angle diagrams at temperatures of 20, 100 and 150 °C, and that the reflex positions which are determined by fitting Lorentzian profiles to the scattering curves are essentially identical. Obviously, there should be a thermal expansion of the material when the temperature is raised to 150 °C. However, this effect changes the values of the cell lattice by only about 1–2%. For example, the position of the most intense reflection corresponds to Bragg spacings of 2.59 nm (20 °C), 2.60 nm (100 °C) and 2.63 nm (150 °C). Only the background, due to thermal fluctuations, and the widths of the reflections increase with increasing temperature. The correlation lengths of the mesomorphous structures are found to decrease in the series 50 nm (20 °C), 35 nm (100 °C), 30 nm (150 °C).

A model that describes the scattering pattern sufficiently is represented by an arrangement of flattened cylinders in a two-dimensional lattice (Fig. 53). The cell dimensions of the unit cells are 5.2 and 3.3 nm with two columns per unit cell. Each column contains three to four poly(*p*-phenylene) strands which are embedded in a matrix of fluorinated alkyl chains. Each strand is bound ionically to the matrix. The most probable orientation of the main axes of the poly(*p*-phenylene) molecules is perpendicular to the two-dimensional unit cell. A tilted orientation of the complexed molecules cannot be excluded. The absence of 00*l* reflections can be explained as a result of the polydispersity of PPP which prevents an arrangement of the strands of complexed molecules in a three-dimensional ordered superstructure. For complexes of

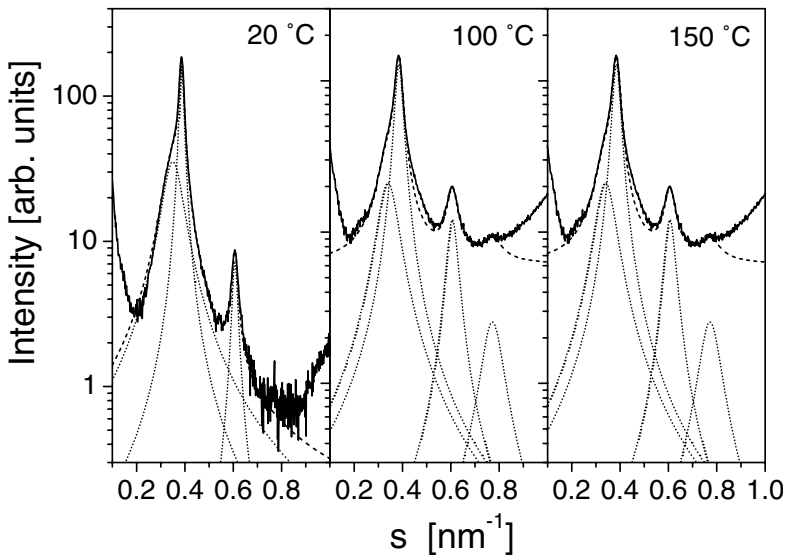

Fig. 54. Small-angle X-ray scattering of the solid complex PPP–F8 at different temperatures. The solid lines represent the scattering data and the dashed lines are the curve fits, which are superpositions of Lorentzian peak profiles. For clarity of the position and width of the peak profiles the individual peaks are given (dotted lines). Reprinted with permission from Macromolecules 2000;33:2124 © American Chemical Society [87].

monodisperse poly(*p*-phenylene) molecules a three-dimensional order such as a smectic H structure is expected.

By differential calorimetry it has been confirmed that the two-dimensional columnar structure is stable over a wide range of temperatures. It is found in the DSC traces that two phase transitions are present for F8, a weak endothermic transition at 173 °C and a strong one at 191 °C. The former is probably a solid/solid phase transition from one crystalline phase α to a second crystalline phase β. The latter is the melting transition of the β phase. By contrast no transition is found in the range −50–300 °C for PPP–F8. The first and the second heating traces are identical. Together with the results from the small-angle scattering it is concluded that the supramolecular structure of the complex is stable within this remarkably large range of temperatures.

3.2. A fluorescent complex with a layered nanoarchitecture [101]

In the past decade, conjugated organic polymers have found many applications such as emitting layers in LEDs [88,102], 'plastic' lasers [103], light-emitting electrochemical cells [104], to name just a few. In contrast to the strictly crystalline inorganic semiconductors with their well-defined long-range order, conjugated polymers, as organic semiconductors, can display a wide variety of different morphologies and solid-state structures with changes in their optical properties and band gaps, even if the same backbone is employed. Recently, Bunz et al. [105] produced evidence of the aggregate formation for dialkylpoly(*p*-phenyleneethynylene)s in solution using fluorescence investigations.

A recently developed synthetic route makes the synthesis of poly(phenyleneethynylene) without diine defects possible [106]. On the basis of such well-defined polymers, Schnablegger et al. [107] found a three-step hierarchy of structures. For example, potassium poly(1,4-phenylene-ethynylene carboxylate) forms aggregates similar to cylinders in a first step. In a second step, the cylinders form fibrils of a higher order and in a third step bundles of fibrils are transformed into globular clusters. The polymer can perform a structure transition into double layers when adsorbed onto substrate materials. An earlier study considers a polyelectrolyte–surfactant complex of dihexadecyldimethylammonium–poly(1,4-phenylene-ethynylene carboxylate) which forms an undisturbed lamellar mesophase in the solid state and can be used for a blue LED with a low turn-on point [119].

This section reports on a polyelectrolyte complex with a random layer structure formed by dimethylditetradecylammonium-poly(1,4-phenylene-ethynylene carboxylate). A sketch of the complex formation is given in Fig. 55.

3.2.1. Nanostructure

Information about the molecular packing of the complex PPE-$^{2}C_{14}$ in bulk material is obtained by wide-angle X-ray scattering. Only a broad maximum is present in the wide-angle region whose position corresponds to a Bragg spacing of 0.45 nm. This value is typical for long alkyl chain polyelectrolyte–surfactant complexes [100] and slightly larger than that found for dihexadecyldimethylammonium-poly(1,4-phenylene-ethynylene carboxylate) (0.43 nm) [119].

By contrast, numerous sharp reflections are present in the pattern of the pristine crystalline surfactant. This proves that PPE-$^{2}C_{14}$ contains neither side-chain crystalline regions nor crystalline impurities of non-complexed surfactant or sodium bromide. The absence of crystallinity is verified by differential calorimetry. Within a temperature range of −100 to 250 °C a glass-transition is found in the thermograms at −47 °C, but no melt transitions are present. This is in contrast to a homologue complex

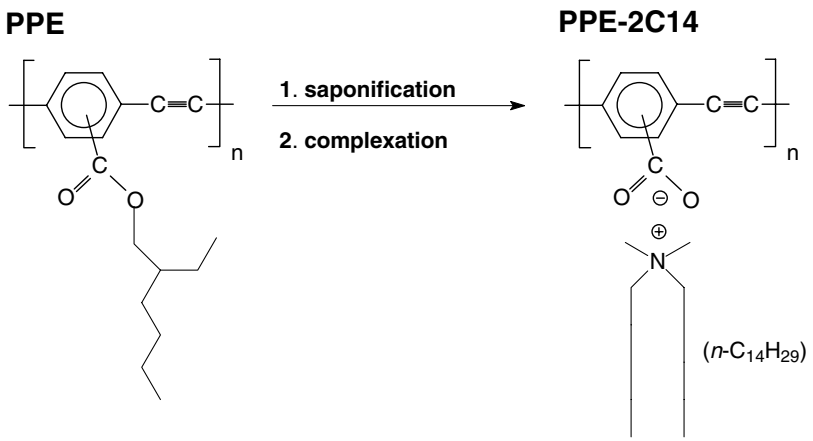

Fig. 55. Sketch of complex formation: poly(2-ethylhexyloxycarbonyl-1,4-phenyleneethynylene carboxylate) PPE. It is saponified and then complexed with dihexadecyldimethylammonium bromide to dimethylditetradecylammonium poly(1,4-phenyleneethynylene carboxylate) PPE-$^{2}C_{14}$. Reprinted with permission from Langmuir 2000;16:3221 © American Chemical Society [101].

with longer alkyl chains, dihexadecyldimethylammonium-poly(1,4-phenylene-ethynylene carboxylate) which shows, in addition to a glass-transition ($T_g = -41$ °C), side-chain crystallinity. About 10% of the alkyl chains are crystalline at temperatures below − 16 °C. Therefore, it can be concluded that the transition between a non-crystalline to a side-chain crystalline complex lies between a chain length of C14 and C16.

The small-angle scattering pattern of PPE-$^{2}C_{14}$ in the form of bulk material is characteristic (Fig. 56). In addition to three sharp symmetric reflections at higher angles with relative positions of 1:2:3 two asymmetric reflections at lower angles are present with relative positions of $1:3^{1/2}$. The latter two show a

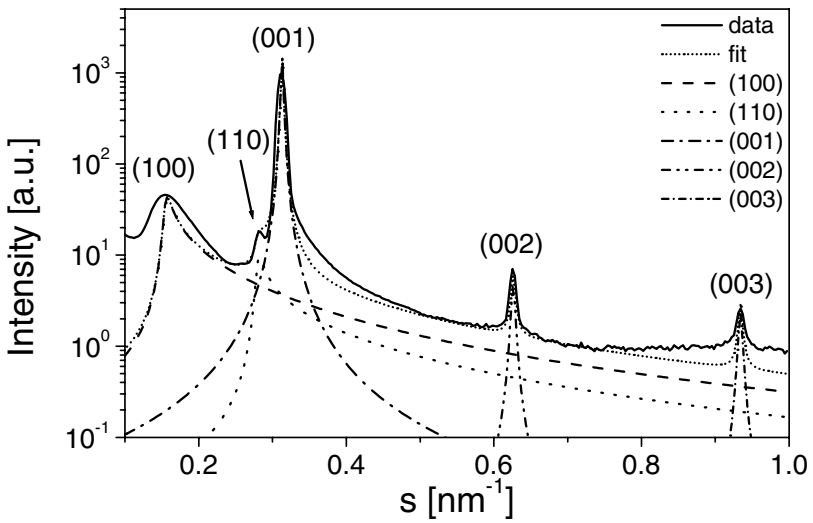

Fig. 56. Small-angle X-ray scattering diagram of (PPE-$^{2}C_{14}$) (solid line) and a fit (dotted line) which is a superposition of two random layer profiles according to Eq. (3.1) with the indices (100) and (110) and three equidistant Lorentzian peak profiles indexed as (001), (002), (003). Reprinted with permission from Langmuir 2000;16:3221 © American Chemical Society [101].

steep decrease in the direction of their low-angle side and a slow decrease towards their high-angle side. Such a scattering pattern is typical for stacks of random layers. This X-ray pattern is due to stacks consisting of alternating ionic layers which are formed by the polyelectrolyte and the ionic head groups, and non-ionic layers which contain the alkyl surfactant tails. From the positions of the (001), (002) and (003) reflections, the long period is determined to be 3.20 nm and from their width the correlation length is given in the range 300–500 nm. A fit of the lamellar reflections with Lorentzian profiles is shown in Fig. 56. The large values of the correlation length must result from a good stacking order and is the highest value observed to date for polyelectrolyte–surfactant complexes.

For the determination of the layer thicknesses, the 'stacking model' is used [7,108] in which the statistics of the lamellar stacks is determined by the distributions $h_1(d_1)$ and $h_2(d_2)$ of the thicknesses of the two lamellae d_1 and d_2. These distributions are considered to be statistically independent, i.e. there is no correlation between the two variances ${\sigma_1}^2$ and ${\sigma_2}^2$. The period d is given by $d = d_1 + d_2$. For a randomly oriented two-phase system with sharp boundaries and normalized distributions $h_1(d_1)$ and $h_2(d_2)$, the scattering intensity for the stacking model is given by

$$I(s) = \frac{k}{4\pi^3 s^4} \mathrm{Re}\left[\frac{(1 - H_1(s))(1 - H_2(s))}{1 - H_1 H_2(s)} \right], \tag{3.1}$$

where H_n is the one-dimensional Fourier transformation of h_n, which is $\exp(-2\pi \mathrm{i} {\sigma_i}^2 s^2 - 2\pi \mathrm{i} d_i s)$, and Re stands for the 'real part'. A fit of Eq. (3.1) to the scattering curve results in $d_1 = 1.30 \pm 0.05$ nm and $d_2 = 1.9 \pm 0.05$ nm (not shown). From the volume fractions of polyelectrolyte and surfactant d_1 are ascribed to the thickness of the ionic layers and d_2 to the non-ionic layers. The random layer profiles are interesting details, which may be caused by hexagonal undulations or perforations.

Both periodic undulations and periodic perforations within the layers represent two-dimensional lattices which lead to additional reflections. If the undulations of different layers are not correlated, the peak profiles are asymmetric. In the event of truly random orientations of the two-dimensional layers no 00l reflections would be produced but in the great majority of cases the layers tend to stack together into parallel-layer groups as might be expected [109]. These structures posses no interlayer order other than the parallelism and degree of separation of the layers. Therefore (00l) and (hk0), but no mixed (hk$l$) reflections are present. The scattering of random-layer (turbostratic) structures have been dealt with in detail by Ruland [110,111]. For a Lorentzian intensity distribution $\{I_\mathrm{h}\} = L/(1 + \pi^2 L^2 s^2)$ normal to an hk reciprocal lattice rod an exact solution is given as

$$I(s) = \frac{1}{4s} \sqrt{\frac{L}{\pi s}} F\left[\frac{\pi L}{2s} \left(s^2 - {s_\mathrm{h}}^2 - \frac{1}{\pi^2 L^2} \right) \right], \tag{3.2}$$

where

$$F(z) = \sqrt{\frac{\sqrt{(z^2 - 1) + z}}{z^2 + 1}}, \tag{3.3}$$

and L is defined as the integral width of $\{I_\mathrm{h}\}$. Peak profiles of Eq. (3.2) are shown in Fig. 56. From the peak positions of the (100) and (110) reflections, given by Eq. (3.2), a distance of the perforations or undulations of 7.5 nm is calculated. It must be stressed here that it is not possible on the basis of the scattering data to distinguish between an undulated and a perforated structure. This distinction has to be made by further experiments (e.g. by gas permeation measurements). Therefore, a model with hexagonal undulated ionic layers is proposed as is shown in Fig. 57.

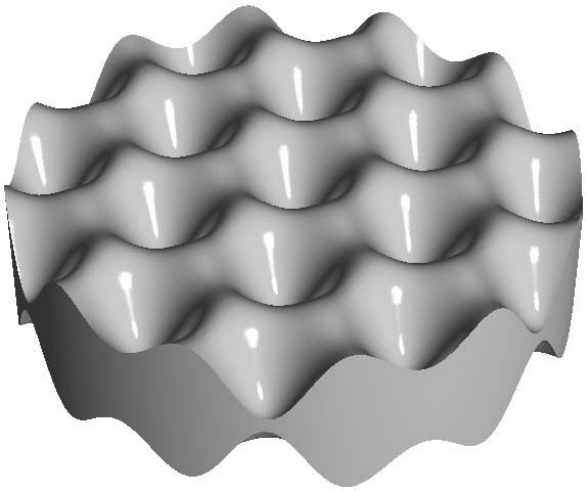

Fig. 57. Model proposed for the interpretation of the random layer profiles of the small-angle scattering curves of PPE-$^{2}C_{14}$ with hexagonal undulations of the ionic layers. Alkyl chains in an amorphous state fill the space between adjacent layers. Reprinted with permission from Langmuir 2000;16:3221 © American Chemical Society [101].

Regular undulations of a polyelectrolyte–surfactant complex are first proposed by Antonietti et al., and called 'mattress' phase [100]. In the bulk structure of the dimethylhexadecylammonium polystyrenesulfonate complex, the mattress ripples of alternating layers are correlated. Recently, quadratically undulated lamellar bilayers, stacked in a rotational disordered way, have been proposed for the structure of surfactant bilayers after polyelectrolyte addition [112]. In contrast to the water-free structure described here, this quadratically undulated lamellar phase exists as a highly diluted phase in water with repeat units of 200 nm. In earlier studies polyelectrolyte–lipid complexes are described which show highly but non-periodic undulations [72] which are considered to be 'plastic membranes' as well as periodic superstructures of quadratic order of an egg-carton shape [76]. In both cases the fine-tuning of the structure is achieved by a variation in the ionic head groups.

The period of the undulations of complex PPE-$^{2}C_{14}$ (7.5 nm) is very close to that calculated in terms of bending elasticity by Goetz and Helfrich for periodically curved membrane superstructures (ca. 7 nm) [113]. Probably, the undulations are preliminary stages of regular pores within the complex layers such as simulated by Müller and Schick for polymeric bilayers, which originate from peristaltic fluctuations of the bilayer thickness [114]. In addition, undulation on length scales only somewhat larger than the bilayer thickness plays a part in the interpretation of the physical properties of lipid membranes [115].

3.2.2. Ultra-thin films

Thin complex films on silicon wafers are prepared by the spin-coating technique from complex solutions. The film structure is then investigated by X-ray reflectivity. Typical examples are shown in Fig. 58. Surprisingly well-defined double-layer stacks in the range 14–140 nm are developed within seconds simply by the deposition of droplets of a complex solution. In Fig. 58 the presence of Kiessig fringes indicate a smooth complex film. From the angular positions of the fringes [51] a thickness of 14 ± 0.5 nm is calculated. The intensity of the fringe around 0.3 nm^{-1} is significantly enhanced compared to that expected of a single layer film. This can be understood as a multilayer structure

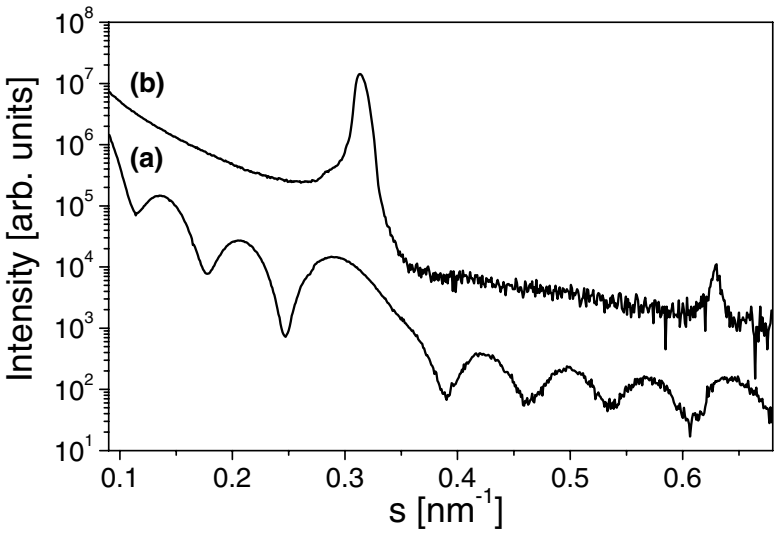

Fig. 58. X-ray reflectivity curves of thin complex films on silicon wafers. Curve a results from a film of complex PPE-$^2C_{14}$ with a thickness of 14 nm consisting of four double layers plus one ionic layer at the wafer/complex interface. The thickness was determined from the position of angular positions of the Kiessig fringes. Curve b results from a film of about 140 nm thickness (determined by a surface profiler). The peaks correspond to the first and second Bragg reflection of the lamellar stacking. Reprinted with permission from Langmuir 2000;16:3221 © American Chemical Society [101].

consisting of alternating ionic and non-ionic layers with the same repeat unit as in the bulk material. Assuming this, the reflectivity curve can be explained as resulting from four double layers (ionic–non-ionic) plus an ionic layer at the complex/wafer interface. For a film of about 140 ± 20 nm thickness—determined by a surface profiler—two sharp Bragg reflections with equidistant position are found (Fig. 58(b)). From their positions, a lamellar spacing of 3.18 ± 0.02 nm is calculated. Within the experimental error this value is identical to that determined for the complex in bulk material (3.2 nm). From the integral width of the reflections a correlation length of about 140 nm is determined. This is of the same order of magnitude as the film thickness. Therefore, it can be concluded that the complex layers are oriented almost perfectly parallel to the wafer surface.

The strong depression of the asymmetric reflections—only a weak shoulder is present at about 0.28 nm^{-1}—is probably due to boundary effects of the underlying wafer surface, which prevent undulations of the lamellae. In order to prove this assumption, visualization of the complex surfaces is achieved by AFM. The film surface is smooth at a micrometer scale, whereas defects at the edges of the wafer can be found on a nanometer level (Fig. 59(a)). These defects have the form of plate islands consisting of terraces of different heights. Each terrace has a height of about 3 nm, which is in good agreement with the lamellar repeat unit. As expected from the reflectivity measurements no regular undulations on the surface are found in addition to defects.

At elevated temperatures (40 °C) self-dewetting of the complex films sets in and finally results in symmetric complex droplets with sizes in the range 50–500 nm in diameter and heights in the range 30–300 nm (Fig. 59(b)). Therefore, it can be concluded that the flat lamellar complex structures are metastable when oriented macroscopically onto a wafer surface. Such instabilities of thin films have not been reported for polyelectrolyte–surfactant complexes elsewhere but they are well known for typical polymers. For example, Reiter et al. have shown that even dispersion forces of less than 1 Pa are capable

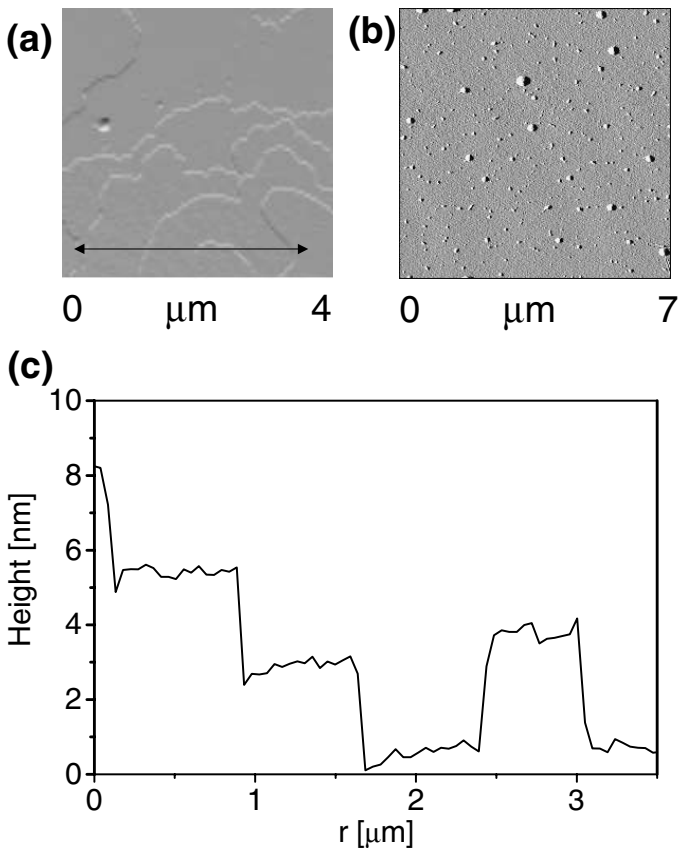

Fig. 59. AFM images of a complex PPE-$^{2}C_{14}$ surface coated on a silicon wafer. Defects are found as terraces of different heights (a). The final stage of the self-dewetting process (2 weeks at 40 °C) are symmetric complex droplets (b). The lower figure (c) shows the height profiles of the terraces from a section of (a, straight line). The height of the steps is about 3 nm. Reprinted with permission from Langmuir 2000;16:3221 © American Chemical Society [101].

of destroying 100 nm thick polymer films of polydimethylsiloxane [116]. Vandenbrouck et al. have shown that liquid crystal films show a dewetting of thin films while thick ones remain stable. They interpreted this behavior as a competition between elasticity and van der Waals forces [117]. Further, Möller et al. investigated the self-dewetting of smectic A side-chain liquid crystalline polymers and discussed it in terms of a progressive disordering of the side-chains with increasing distance from the substrate [56]. Similar to the polymers described by these authors, the dewetting phenomena of complex PPE-$^{2}C_{14}$ films have an important influence for any possible thin film applications of such complexes.

3.2.3. Optical properties

Neher [88] has pointed out that morphology plays a crucial role in the manipulation of the optical properties of conjugated polymers, and recently Bunz et al. produced evidence of lamellar, nematic and sanidic crystalline structures of alkylated poly(*p*-phenyleneethynylene)s which have been proposed to allow an improved design of optical devices based on these organic semiconductors [118]. As Bunz showed for the side-chain crystalline polymers a strong influence of the nanostructure of the complex on

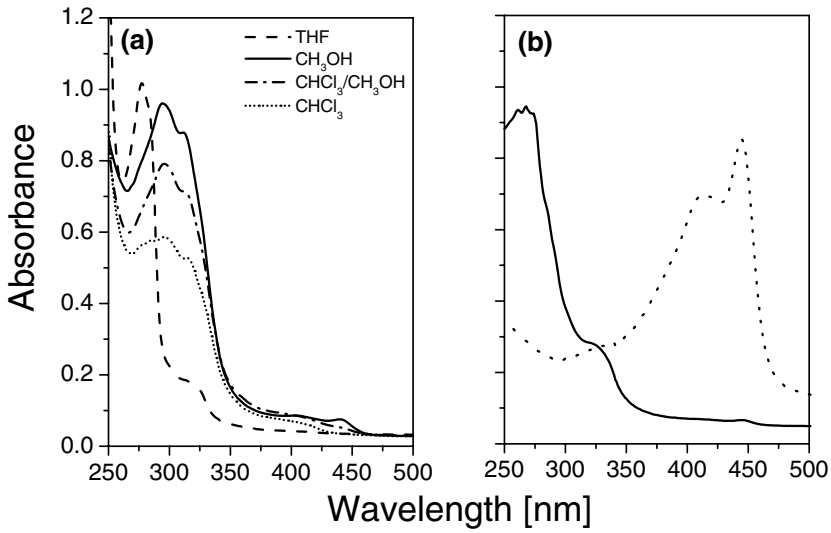

Fig. 60. Absorption spectra of complex PPE-$^{2}C_{14}$ in different solvents (0.1%) (a) and in the solid state (b, solid line). The dotted line of (b) is the absorption spectrum of poly(2-ethylhexyloxycarbonyl-1,4-phenyleneethynylene). Reprinted with permission from Langmuir 2000;16:3221 © American Chemical Society [101].

its optical properties is to be expected. In order to prove this assumption UV–Vis and fluorescence measurements on the complex in solution and in the solid state are performed.

The absorption spectra of complex solutions in tetrahydrofuran, methanol, methanol/chloroform (1:1) mixture and chloroform are shown in Fig. 60(a). It can be seen there that the complex PPE-$^{2}C_{14}$ is a strong solvatochromic compound. In chloroform three transitions at 277, 296 and 315 nm are present. In a 1:1 mixture of methanol and chloroform the higher energetic transition is reduced and in methanol clear maxima at 294 and 311 nm are present. The maximum at 277 nm is absent. In a solution of tetrahydrofuran a strong band at 278 nm dominates the spectrum. Only a weak maximum is present at 315 nm. It is assumed that the complex in all the solutions has at least three different possible transitions in the UV–Vis region (277, 296 and 315 nm). The solvent may have an influence on the conformational state of PPE-$^{2}C_{14}$ which influences the absorption spectrum. In Fig. 60(b) it can be seen that the absorption spectrum of the complex in the solid state with a strong transition at 268 and a weak transition at 326 nm resembles that of a complex solution in tetrahydrofuran, but shows a stronger absorbance at lower wavelengths.

By contrast, the absorbance of PPE is dominated by a first maximum at 413 nm and a second at 444 nm. The latter is similar to that observed by Bunz for aggregates of alkylated poly(1,4-phenyleneethynylene) [105]. He interpreted the first maximum as the absorbance of the undisturbed polymer and the second maximum as the result of aggregates, which form excimers. From the similarity of the UV–Vis spectrum of the aggregates observed by Bunz in solution and that of PPE-$^{2}C_{14}$ as a thin film it can be concluded that the molecular orders within aggregates and within the complex films are probably similar. Bunz showed further that the fluorescence emission spectra depend on the polarity of the solvent, the higher the amount of methanol in a chloroform/methanol mixture, the higher is the excimer intensity. It can be seen in Fig. 61(a) that the emission spectrum of PPE-$^{2}C_{14}$ in tetrahydrofuran also depends significantly on the polymer concentration. The emission maximum at 428 nm shifts from 428 nm at a concentration of 10^{-4}% (w/w) and 431 nm at 10^{-3}% (w/w) to 435 nm at 10^{-2}% (w/w).

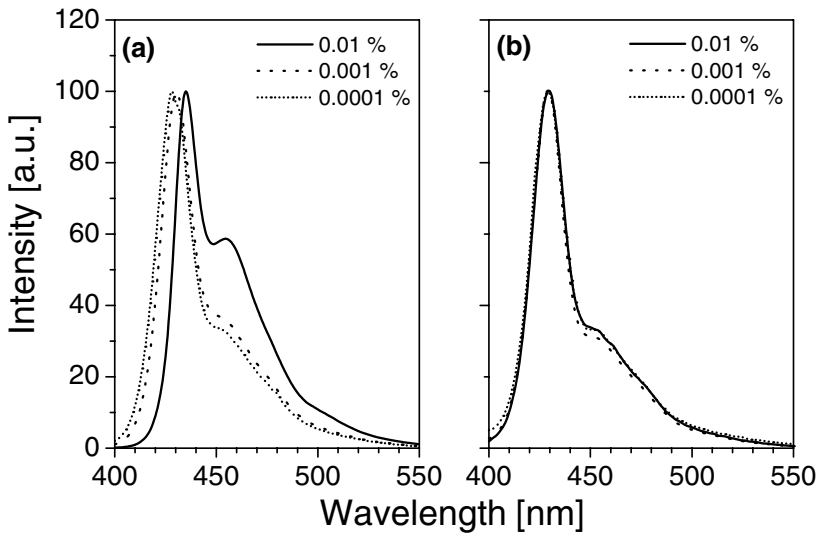

Fig. 61. Emission spectra of poly(2-ethylhexyloxycarbonyl-1,4-phenyleneethynylene) (b), and the complex PPE-$^{2}C_{14}$ in tetrahydrofuran (b) at different concentrations (the excitation wavelength is 380 nm). Reprinted with permission from Langmuir 2000;16:3221 © American Chemical Society [101].

Within this series the amount of excimer emission (455 nm) increases considerably. Obviously the aggregate formation depends strongly on the polymer concentration and already sets in at very low concentrations. This observation is consistent with the work of Schnablegger et al. [107] who found a complicated aggregation behavior of PPE. By contrast, no concentration dependence of the emission spectrum is found in the same range of concentration for the complex PPE-$^{2}C_{14}$. It can be seen in Fig. 61(b) that the relative intensities of the emission maxima at 430 and 453 nm do not depend on the concentration within the same range of concentration. From this it can be concluded that aggregates are present in the solution of PPE and PPE-$^{2}C_{14}$ but the aggregates of PPE-$^{2}C_{14}$ are constant in their composition over a large range of concentrations of at least three decades, while the aggregate composition of PPE depends strongly on its concentration.

A direct comparison of the fluorescence properties of PPE and PPE-$^{2}C_{14}$ at higher concentration is shown in Fig. 62. In a 0.1% solution of tetrahydrofuran the excitation of the complex (Fig. 62(a) solid line) and that of the alkylated polymer (Fig. 62(a), dashed line) have a maximum at 393 nm. The spectra differ slightly in the region of lower wavelengths. In the emission of the complex (Fig. 62(a), solid line) a strong maximum is found at 429 nm and a weak maximum at 455 nm (excimer). Compared to that the emission spectrum of PPE the PPE-$^{2}C_{14}$ shows a slight red-shift of the intense maximum (435 nm) and an increased intensity of the second maximum which indicates a higher amount of excimers. Apart from these details the emission in solution of PPE and PPE-$^{2}C_{14}$ shows the same characteristics. The excitation spectrum of PPE in the solid state has maxima at 400 and 439 nm; that of PPE-$^{2}C_{14}$ at 408 and 445 nm (Fig. 62(b)). The band at a higher wavelength is more intense for PPE-$^{2}C_{14}$ than for PPE.

The emission spectra of both compounds differ strongly. That of PPE is structureless with a broad and intense maximum at 498 nm and a weak maximum at 420 nm, whereas the emission spectrum of PPE-$^{2}C_{14}$ is highly structured with maxima at 425, 458, 486, 496, 520 and 575 nm (Fig. 62(b)). This

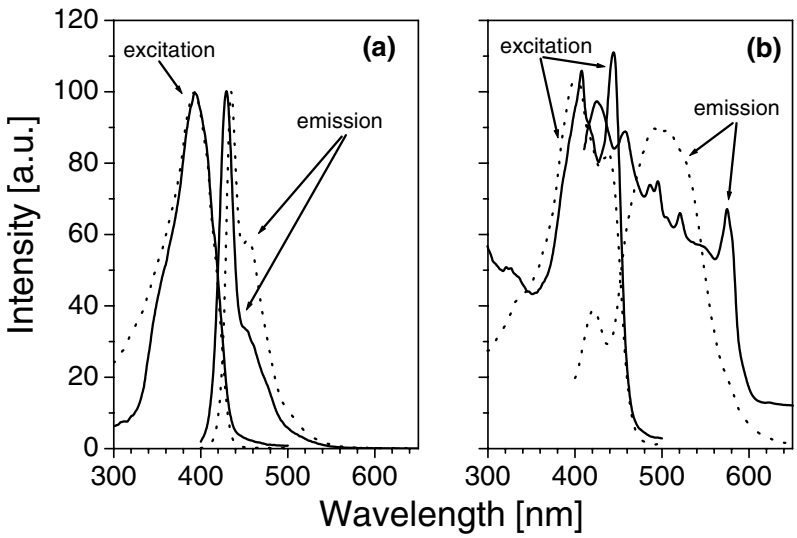

Fig. 62. Fluorescence excitation and emission spectra of PPE and PPE-$^{2}C_{14}$ in solutions of 0.1% (w/w) tetrahydrofuran (a) and as solid-state materials (b). The dotted lines correspond to PPE and the solid lines to PPE-$^{2}C_{14}$. The excitation wavelength are 380 nm, the emission wavelength is 550 nm. Reprinted with permission from Langmuir 2000;16:3221 © American Chemical Society [101].

observation is unexpected and its origin is as yet not clear. For a first interpretation it is assumed that the structure of the emission results from the regularity of the undulations of the lamellar structure, which may lead to a number of definite emission bands. But more detailed work has to be done in order to clarify the relation between the mesomorphous ordering and the optical properties of fluorescent polyelectrolyte–surfactant complexes.

In summary it has been demonstrated that the optical properties of the highly fluorescent alkylated polymer PPE can be changed to a considerable degree by its conversation to an ionic polymer complex PPE-$^{2}C_{14}$. The effect of complexation is pronounced in the solid state where the emission properties of PPE is structureless, while those of PPE-$^{2}C_{14}$ show a detailed structuring. The solid-state structure of PPE-$^{2}C_{14}$ is lamellar with a hexagonal in-plane order of undulations but with no plane-to-plane correlation. The complex can be prepared as a highly ordered multilayer film in a single step procedure which makes it, in principle, superior because it is faster compared to established methods for the formation of thin multilayer films.

3.3. Electroluminescent polyelectrolyte complexes [119,151]

Conjugated polymeric materials have been subjects of intense academic and industrial research for their use in LEDs in the last decade. The work on organic LEDs has been summarized in a number of reviews [102,120–124]. Typically, polymers in organic LEDs have a conjugated backbone and normally they are non-ionic. On the other hand, it has been shown that polyelectrolytes such as polyaniline (in its form as an emeraldine salt) increase the hole transport via the indium tin oxide electrode. As a result, the light-emitting characteristics of the LEDs are strongly improved [125]. It has been shown recently that polyelectrolytes are useful in forming stepped and graded electronic profiles

leading to remarkably efficient single-layer polymeric LEDs [126]. In addition, complexes of polyelectrolytes and surfactants form interesting nanostructured materials in the solid state [9,10]. The first example of the combination of a rigid-rod-like polyelectrolyte and a surfactant into a material which is useful for the production of LEDs has been given by Neher et al. [91]. Further, a nanostructured PPE complex, dihexadecyldimethylammonium-poly(1,4-phenyleneethynylene carboxylate) has been described. This material displays blue electroluminescence in single-layer LEDs with low turn-on-points [119].

In this section, complexes of PPE with a number of different counter ions will be introduced. The molecular structures of the compounds are given in Fig. 63. The emphasis is on the solid-state structures of the complexes and their optical properties.

3.3.1. Thermal properties

The thermal properties of the complexes have been investigated by using DSC. It is found that none of the complexes show a glass transition, which is probably due to the high ionic character of the materials in combination with the rigid-rod-like polymeric backbone. Melting peaks are found for alkyl chain lengths higher than 12 in the series of the double-chain surfactant containing complexes. The complex PPE-$^{2}C_{14}$ displays a melt transition at -27 °C, PPE-$^{2}C_{16}$ at 5 °C and PPE-$^{2}C_{18}$ at 20 °C (Fig. 64). The endothermic transitions are attributed to a melting of crystalline side-chains, which are represented by the alkyl tails of the surfactants. In the way recommended in the literature [127] the amount of crystalline CH_2 groups have been calculated to be 8% (PPE-$^{2}C_{14}$), 15% (PPE-$^{2}C_{16}$) and 20% (PPE-$^{2}C_{18}$). They are present in the structures below the individual melt transition of each complex. The complex PPE-Py_{16} displays a melt transition at 18 °C and an amount of about 10% crystalline CH_2 groups. No crystallinity has been detected for the other complexes in the temperature range -100 to 150 °C.

3.3.2. Nanostructures

Wide- and small-angle X-ray measurements are undertaken in order to complement the information

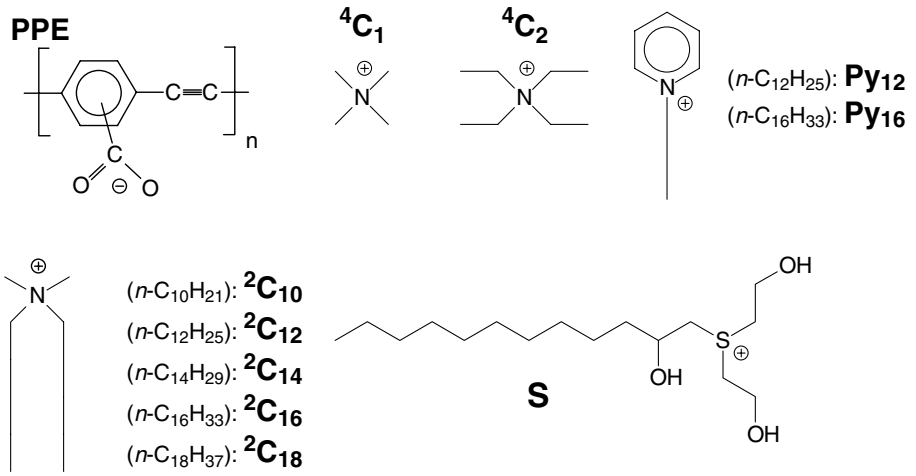

Fig. 63. The molecular structures of the compounds used for complexation: poly(*p*-phenyleneethynylene carboxylate) (PPE), tetramethylammonium ($^{4}C_1$), tetraethylammonium ($^{4}C_2$), dialkyldimethylammonium ($^{2}C_{10}$, $^{2}C_{12}$, $^{2}C_{14}$, $^{2}C_{16}$, $^{2}C_{18}$), alkylpyridinium (Py_{12}, Py_{16}), 2-hydroxy-S,S(bis(2-hydroxyethyl)dodecylsulfonium) (S). Reprinted with permission from Langmuir 2001;17:5098 © American Chemical Society [151].

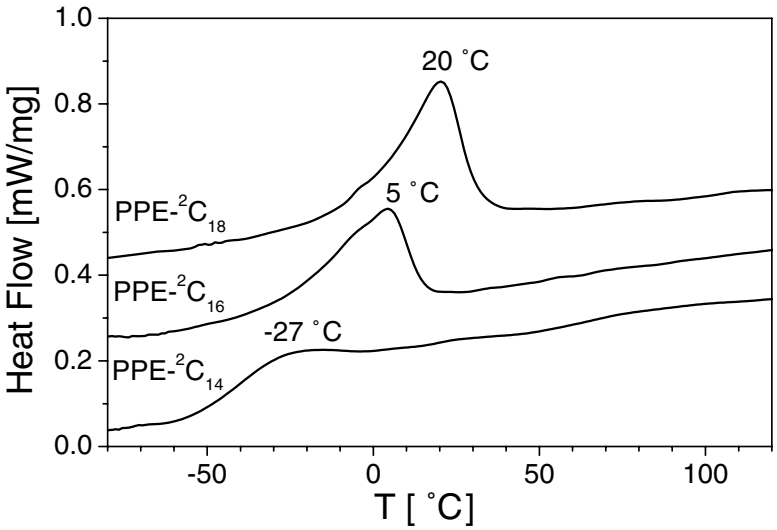

Fig. 64. The DSC traces of PPE-^{2}C$_{14}$, PPE-^{2}C$_{16}$ and PPE-^{2}C$_{18}$. Reprinted with permission from Langmuir 2001;17:5098 © American Chemical Society [151].

on the molecular and supramolecular structures of the complexes. The wide-angle diagrams of the complexes reveal that only two of the 10 complexes, PPE-^{2}C$_{18}$ and PPE-Py$_{16}$, contain crystalline side-chains at temperatures below 16 °C. It can be seen, for example, that an amorphous halo is found in the wide-angle diagram of PPE-^{2}C$_{16}$ (Fig. 65(a), upper curve) while, in addition to this, an intense reflection is found in the wide-angle diagram of PPE-^{2}C$_{18}$ (Fig. 65(b), upper curve). By contrast, a number of sharp reflections are present in the diagrams of the surfactants ^{2}C$_{16}$ and ^{2}C$_{18}$ (see lower curves in Fig. 65(a) and (b)). Both surfactants are highly crystalline compounds at room temperature. It is a typical property of

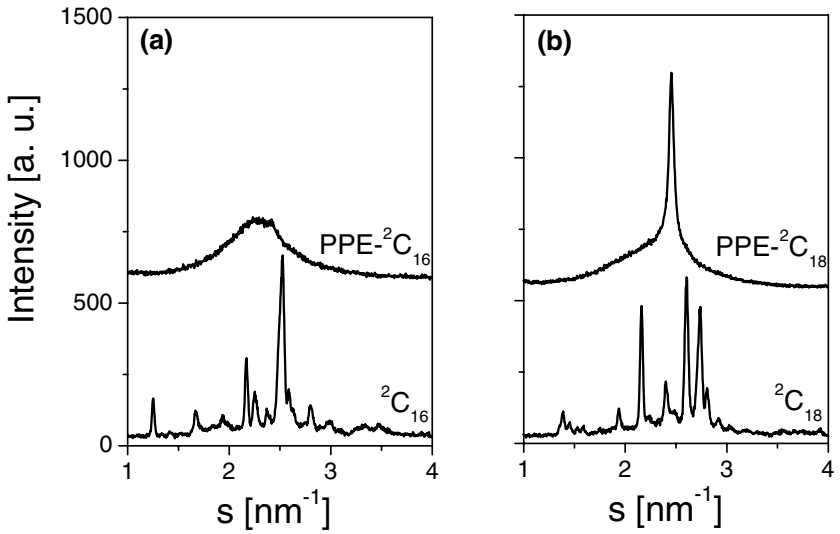

Fig. 65. The wide-angle X-ray scattering diagrams of ^{2}C$_{16}$, PPE-^{2}C$_{16}$ (a) and ^{2}C$_{18}$, PPE-^{2}C$_{18}$ (b). Reprinted with permission from Langmuir 2001;17:5098 © American Chemical Society [151].

polyelectrolyte–surfactant complexes that crystallinity in these complexes is absent or strongly reduced compared to the surfactants [128]. No reflections are found in the small-angle scattering diagrams of the two complexes with the non-amphiphilic counter ions (PPE-$^{4}C_{1}$ and PPE-$^{4}C_{2}$).

In combination with the results from differential calorimetry and wide-angle scattering, it can be concluded that these complexes are amorphous materials in the temperature range −100 to 150 °C. By contrast, reflections of equidistant positions are present in the small-angle diagrams of the other eight complexes, which contain the amphiphilic counter ions. Examples are shown in Fig. 66. The scattering diagrams of these complexes are interpreted as resulting from lamellar mesophases.

The long periods of the complexes are summarized in Table 15. It can be seen that the long periods vary from 2.38 nm (PPE-$^{2}C_{10}$) to 4.27 nm (PPE-Py_{18}). As expected it can be observed that the repeat unit increases with the increasing chain length of the complexed surfactant. But the increase is not strictly linear as would be expected for a series of isomorphous lamellar structures. This can be seen in Fig. 67 (triangles) for the series of the double-chain surfactant containing complexes. The increase of the long period is almost linear for PPE-$^{2}C_{10}$, PPE-$^{2}C_{12}$, and PPE-$^{2}C_{14}$. Then the increase from PPE-$^{2}C_{14}$ to PPE-$^{2}C_{16}$ reduces, and the long period of PPE-$^{2}C_{16}$ is even smaller than that of PPE-$^{2}C_{18}$. For comparison, the theoretical values of the long period with increasing alkyl chain length is given in Fig. 67 (squares). It can be seen that the experimental values are slightly smaller than the theoretical values for the complexes containing the shorter alkyl chains (10, 12, 14 and 16).

The scattering curves of the complexes are interpreted as resulting from lamellar structures with the surfactants in a double-layer arrangement with the alkyl chains in a liquid-like order. The lamellar structures are similar to those of the polystyrene sulfonate alkyl ammonium complexes, described by Antonietti et al. [100]. They are the first to demonstrate that modifications of the lamellae such as periodically undulations can be produced by varying the alkyl chain lengths.

The presence of undulations may be an explanation for the deviation of the linear increase of the long period. In the case of PPE-$^{2}C_{14}$ it has been shown that its lamellar mesophase consists of alternating

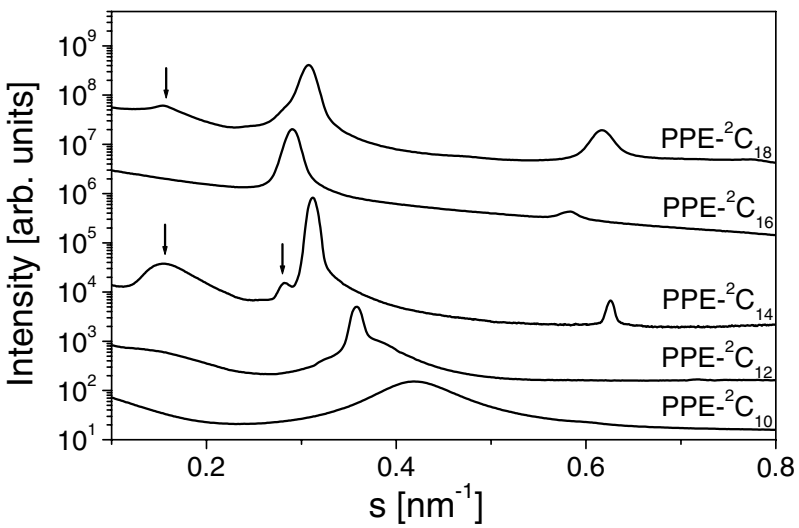

Fig. 66. The small-angle X-ray scattering diagrams of the PPE complexes with double-chain surfactants: PPE-$^{2}C_{10}$, PPE-$^{2}C_{12}$, PPE-$^{2}C_{14}$, PPE-$^{2}C_{16}$ and PPE-$^{2}C_{18}$. The arrows indicate the non-lamellar reflections attributed to periodic undulations of the lamellae. Reprinted with permission from Langmuir 2001;17:5098 © American Chemical Society [151].

Table 15
Structural properties of the PPE complexes as determined from X-ray measurements and the positions of the maxima of the electroluminescence

Complex	Long period (nm)	Correlation length (nm)	Structure	Maximum in the electroluminescence (nm)
PPE-$^4C_1$	–[a]	–[a]	Amorphous	430
PPE-$^4C_2$	–[a]	–[a]	Amorphous	430
PPE-$^2C_{10}$	2.38	11 ± 2	Smectic A	440–450
PPE-$^2C_{12}$	2.80	70 ± 5	Smectic A	440–450
PPE-$^2C_{14}$	3.20	170 ± 10	Smectic A	480
PPE-$^2C_{16}$	3.45	65 ± 5	Smectic A	440–450
PPE-$^2C_{18}$	3.25	60 ± 5	Smectic B	440–450
PPE-Py_{12}	3.24	14 ± 2	Smectic A	470
PPE-Py_{18}	4.27	50 ± 5	Smectic B	480
PPE-S	3.33	≈10	Smectic A	515

Reprinted with permission from Langmuir 2001;17:5098 © American Chemical Society [151].
[a] No reflections are found in the small-angle scattering diagrams.

ionic layers (1.3 nm) and non-ionic layers (1.9 nm) with periodic undulations of a hexagonal symmetry and a maximum-to-maximum distance of 7.5 nm (Section 3.2.1). The positions of the undulations in adjacent layers are not correlated. Reflections resulting from undulations are marked by arrows in Fig. 66. It is found that the structures do not follow a simple correlation in the series form PPE-$^2C_{10}$ to PPE-$^2C_{18}$. For example, for PPE-$^2C_{14}$ it is possible to show a high probability of the existence of undulations. No indications of undulations are present in the scattering curve of PPE-$^2C_{16}$, while a weak reflection with a Bragg distance of about 6 nm in the curve of PPE-$^2C_{18}$ indicates that this complex also

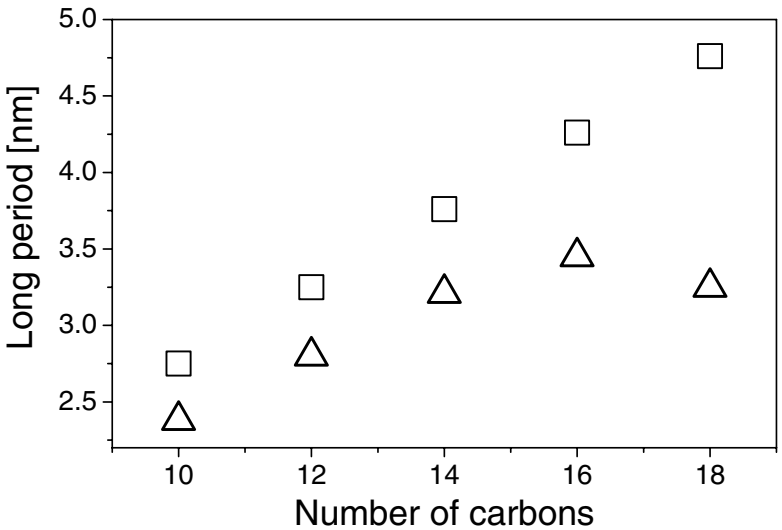

Fig. 67. The long periods of the double-chain containing surfactant complexes depend on the number of carbon atoms in the surfactant chains. The triangles represent the values determined by small-angle scattering measurements and the squares represent values that were calculated for a double-layer arrangement of the surfactant with extended alkyl chains. Reprinted with permission from Langmuir 2001;17:5098 © American Chemical Society [151].

has undulations. If the possibility of undulations is ignored, even though it is an interesting detail of the lamellar structures of the complexes, then the structures at 16 °C are classified into three structural categories: amorphous (PPE-$^{4}C_{1}$, PPE-$^{4}C_{2}$), smectic A (PPE-$^{2}C_{10}$, PPE-$^{2}C_{12}$, PPE-$^{2}C_{14}$, PPE-$^{2}C_{16}$, PPE-Py_{12}, PPE-S) and smectic B (PPE-$^{2}C_{18}$, PPE-Py_{16}). Above the melt transition of the side-chains at 20 and 18 °C, respectively. It is assumed that PPE-$^{2}C_{18}$ and PPE-Py_{16} undergo an order–order transition from smectic B to smectic A.

The correlation lengths of the complexes are calculated in order to compare their degree of order. This is done by using the widths of the (001) reflections [64]. It can be seen in Table 15 that the correlation lengths are in the range 10–170 nm. The trend that the correlation lengths of the complexes with the shorter alkyl chains are lower than that of the complexes with the longer chains can be seen. For example, 14 nm are found for PPE-Py_{12} and 50 nm PPE-Py_{18}. But there is an exception: PPE-$^{2}C_{14}$, which has the highest correlation length (170 nm). Probably, this results from its additional ordering in the plane of the lamellae.

3.3.3. Optical properties

The optical properties of a number of poly(1,4-phenyleneethynylene)s in solution are found to depend strongly on the concentration of the polymer solution, which is interpreted as the result of the aggregation behavior of these polymers [105]. By contrast, it is found that the photoluminescence of the complexes depends on the type of the counter ions but it is widely independent of their concentrations. The emission spectra of thin films are given in Fig. 68 as an example. The excitation wavelength is 380 nm.

The positions of the emission maxima of the complexes depend on the nature of the head group. They shift in the line PPE-$^{4}C_{1}$ (470 nm), PPE-$^{2}C_{18}$ (490 nm), PPE-Py_{16} (510 nm) and PPE-S (515 nm). The same sequence is found in the electroluminescence diagrams of single layer LEDs, which contain the complexes in the form of thin films (140 nm) as the active layer. It can be seen in Fig. 69 that the shift of

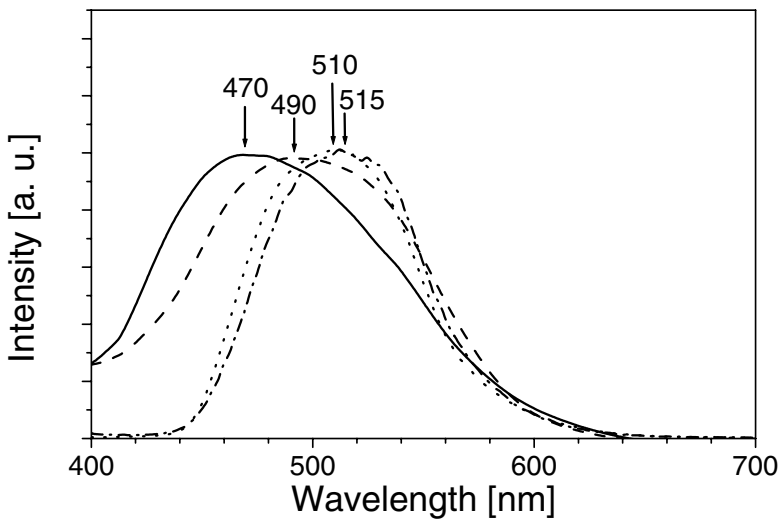

Fig. 68. Fluorescence emission spectra of PPE-$^{4}C_{2}$, (solid line), PPE-$^{2}C_{18}$ (dashed line), PPE-Py_{16} (dotted line) and PPE-S (dash-dotted line). The emission maxima are indicated by arrows. The excitation wavelength is 380 nm. Reprinted with permission from Langmuir 2001;17:5098 © American Chemical Society [151].

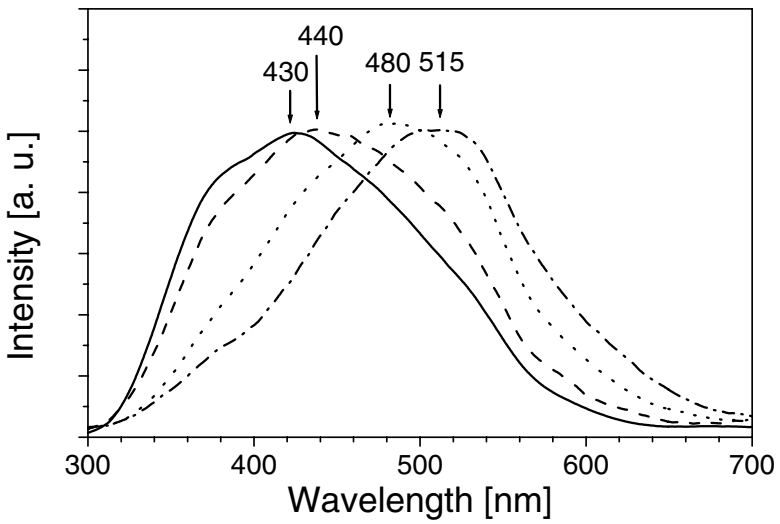

Fig. 69. Electroluminescence spectra of single-layer LEDs of PPE-$^{4}C_{2}$, (solid line), PPE-$^{2}C_{18}$ (dashed line), PPE-Py_{16} (dotted line) and PPE-S (dash-dotted line). The emission maxima are indicated by arrows. Reprinted with permission from Langmuir 2001;17:5098 © American Chemical Society [151].

the maxima of the electroluminescence is larger than in the photoluminescence (85 nm instead of 45 nm). The curves of PPE-$^{4}C_{1}$ (430 nm), PPE-$^{2}C_{18}$ (440 nm), PPE-Py_{16} (480 nm) and PPE-S (515 nm) are displayed. The values of the position of the electroluminescence maxima are summarized in Table 15. Further it is found that the positions of the maxima of the double-chain containing complexes do not depend on the chain length; they are between 440 and 450 nm. PPE-$^{2}C_{14}$ is an exception. Its maximum in the electroluminescence spectra is found at 480 nm. This possibly results from the parallel alignment of the polymeric chains in the plane of the lamellae, which leads to an increase in the conjugation lengths of the polymeric backbone. Despite this exception it can be concluded that the optical properties of the complexes are largely independent of the length of the alkyl chains, but they depend on the nature of the ionic head group to a great extent. Tentatively this shift of the fluorescence maxima can be interpreted as resulting from the polarizability of the ionic head group. Within the HSAB concept the ammonium group is the hardest and least polarizable; it is followed by the pyridinium group and the sulfonium group, which is the softest and most polarizable group. Therefore, under the condition that the type of the mesomorphous structure is the same, it is concluded that the electroluminescence spectra shift to higher wavelengths when the counter ions become more polarizable. The counter ions seem to influence the effective conjugation length of the polymeric backbone: hard counter ions result in its increase, whereas soft counter ions result in its decrease.

From a material science point of view, it is interesting that the emission properties of a conjugated polymer can be shifted simply by exchanging the counter ions. It is conceivable that red, green and blue LEDs could be produced by using one conjugated polymer; only the counter ions have to be changed. Appropriate candidates for this may be cationic and anionic derivatives of poly(*p*-phenylenes) [48,129,130] Current–voltage diagrams of the LEDs from the PPE complexes are recorded in order to determine the voltage where the LEDs start emitting light (turn-on point). It is found that the turn-on points of LEDs from all the complexes are around 6 V when the thickness of the active layer is 140 ± 20 nm. A typical current–voltage curve is shown in Fig. 70. This finding is surprising because it is normally

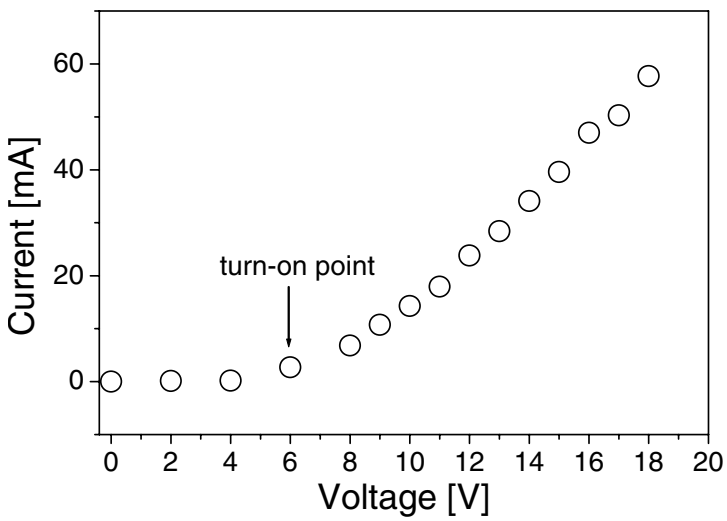

Fig. 70. Current–voltage curve of single-layer LED with PPE-$^{2}C_{14}$ as the active layer. The layer thickness is 140 nm. Reprinted with permission from Langmuir 2001;17:5098 © American Chemical Society [151].

expected that the turn-on point also depends on the nature of the counter ion. It is known that the turn-on point of similarly prepared LEDs using the pristine polymer with covalently bound side groups, poly(2-ethylhexyloxycarbonyl-1,4-phenyleneethynylene), is around 21 V with an emission maximum at 557 nm [131]. The much lower turn-on point of the complexes compared with the covalent analogue polymer is probably due to the highly ionic character of the complexes. Normally such low turn-on points need the support of an additional charge transport layer [102] which, concerning the complexes, is obviously built in.

In conclusion, it has been demonstrated that the optical properties of single-layer LEDs of PPE complexes depend on the nature of the counter ions. The maximum of the electroluminescence can by shifted from 430 nm, when using hard counter ions, to 515 nm when using soft counter ions. It is suggested that it is, in principle, possible to produce single-layer LEDs which cover the entire visible spectrum by using only one polymer. The turn-on points of the LEDs are around 6 V for layer thicknesses of 140 nm. The complexes of PPE with amphiphilic counter ions are either smectic A or smectic B at room temperature, with repeat units of 2.38–4.27 nm, while the complexes with non-amphiphilic counter ions are amorphous. The correlation lengths of the lamellar structures vary between 10 and 170 nm.

4. Columnar discotic complexes

There is currently much interest in polycyclic aromatic materials which show strong $\pi-\pi$ interactions and form columnar mesophases [132–136]. Apart from the beauty of their structures, potential applications such as vectorial charge transport layers in xerography, electrophotography and molecular electronic devices are under discussion. It has been observed, e.g. that *peri*-condensed hexabenzocoronenes show diode-like current–voltage signals for single molecules [137] and a rapid charge transport along self-assembled columns with high carrier mobilities. For an oriented layer with a thickness of

1 μm and an applied potential of 1 V the drift time of charges across such a layer is calculated to be less than 1 ms [138]. The one-dimensional nature of the charge transport makes these molecular structures promising as nanowires in molecular electronic devices. Section 4.1 reports on a hexa-peri-hexabenzocoronene, functionalized with a carboxylic acid group, which is complexed with a hydrophobically modified polyethyleneimine.

In comparison to the non-complexed discotic material the complex is found to be more elastic over a wide range of temperatures. The intra-columnar ordering of the complex, which is an essential characteristic for a one-dimensional conductivity, is better than in the hexa-peri-hexabenzocoronene. Further, an important general property of mesophases formed by polyelectrolyte–surfactant complexes compared with typical liquid crystalline phases is the absence or reduction of sharp dislocations in their optical textures [12,72]. This indicates the presence of smoother domain boundaries in their nanostructures than those present in their surfactant liquid crystalline phases. It is expected that highly extended columns in a polymer complex of an amphiphilic hexabenzocoronene could be useful molecular nanowires. Section 4.2 reports on a complex which is formed by an alkylated, *peri*-condensed hexabenzocoronene, functionalized by a carboxylic acid group, and an amino-functionalized polysiloxane.

4.1. Polyethyleneimine hexa-peri-hexabenzocoronene [139]

In this section, the phase behavior and mechanical properties of a hexabenzocoronene (HBC) which is functionalized by a carboxylic acid group and that of its complex with hydrophobic modified polyethyleneimine (PEIC22–HBC) will be described. The structures of the compounds are shown in Fig. 71.

4.1.1. Nanostructures

Analogously to polyelectrolyte–surfactant complexes of the previous sections, HBC is treated as an surfactant and the PEIC22 as a polyelectrolyte. Due to the insolubility of HBC in water, its complexation with PEIC22 is carried out in chloroform using an equimolar amount of HBC with respect to amino and carboxylate functions. The resulting complex HBCC22-PEI is solvent-cast as films and analyzed by IR-spectroscopy, DSC, X-ray scattering and dynamic-mechanical measurements. A comparison of the IR-spectra of HBC and HBCC22-PEI shows that the carboxylic acid vibration found for HBC at 1710 cm^{-1} is absent for HBCC22-PEI. Instead of the sharp carboxylic acid band in the spectrum of HBC a broad diffuse band between 1500 and 1760 cm^{-1} is present in HBCC22-PEI resulting from ionic carboxylate-ammonium structures. In both spectra the C=C stretch vibration at 1610 cm^{-1} and the CH_2 bending vibrations at 1466 and 1456 cm^{-1} are identical. From this it is concluded that, within the experimental error, all of the carboxylic acid functions of HBC form acid–base pairs with the amino functions of PEIC22, resulting in a stoichiometric PEIC22–HBC complex.

In the wide-angle X-ray diagram of PEIC22 at 20 °C, sharp reflections are found at a scattering vector of $s = 2.39$ and 2.63 nm^{-1}. This is attributed to a side-chain crystallinity of PEIC22, in which the docosylic chains crystallize. For determination of the lattice parameters, the data are compared with that found for orthorhombic polyethylene [140] with lattice constants of $a = 0.7417$ nm, $b = 0.4945$ nm and $c = 0.2547$ nm. Assuming the same lattice for PEIC22, the indexing of the upper reflections is (110) and (200) giving lattice constants $a = 0.76$ nm and $b = 0.50$ nm. In the unit cell the alkyl chains are oriented perpendicular to the a–b plane and the average area per chain is 0.19 nm^2, which is slightly larger than that for polyethylene (0.183 nm^2). Neither HBC nor the complex PEIC22–HBC shows sharp reflections

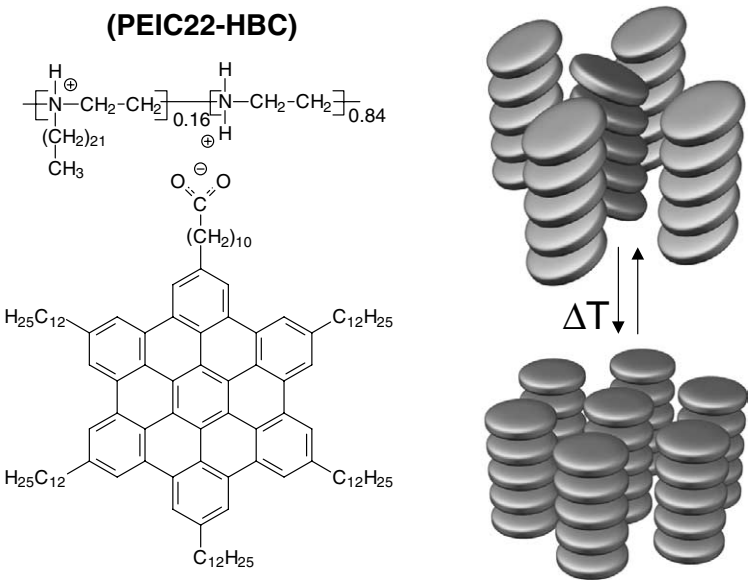

Fig. 71. The molecular structure of an ionically bound complex (PEIC22–HBC) formed by a hydrophobic modified polyethyleneimine (PEIC22) and a hexa-peri-hexabenzocoronene (HBC). PEIC22 and HBC are not drawn. Sixteen percent of the amino functions of PEIC22 are alkylated by *n*-decoys chains, HBC is functionalized by a carboxylic acid function which serves as an anchor group. The sketch on the right illustrates the columnar mesophases formed by HBC and PEIC22–HBC. For clarity only the aromatic cores of HBC are drawn. At room temperature a rectangular centered lattice is found for both. The aromatic cores are tilted with respect to the column axis. At higher temperatures the columns are oriented in a hexagonal columnar mesophase. Reprinted with permission form J Mater Chem 1999; 9:1055 © The Royal Society of Chemistry [139].

in the wide-angle region of the scattering curves, proving the absence of crystallinity in the structures. The absence of crystallinity in PEIC22–HBC is also indicative of a stoichiometric complex.

The DSC curve of PEIC22 shows a melting peak at 59 °C with an enthalpy of 73 J/g. Under the usual assumptions made for the calculation of crystallinity [141], the amount of crystalline side-chains of PEIC22 is determined to be in the range 40–50%. In the DSC trace of HBC an endothermic transition is found at 93 °C for heating and at 62 °C for cooling. For PEIC22–HBC an endothermic transition is found at 70 °C for heating and at 52 °C upon cooling. The different values found for the hysteresis, 18 °C PEIC22–HBC and 31 °C HBC, may be interpreted as a consequence of a faster relaxation to an equilibrium state of PEIC22–HBC. Considering the absence of crystalline reflections in the X-ray diagrams of HBC and PEIC22–HBC, the exothermic transitions can be assigned to liquid crystalline phase transitions. This assumption is proven by optical polarization microscopy and by small-angle X-ray scattering.

Both compounds show strong birefringence when observed between crossed polarizers and a texture change at transition temperatures found by DSC. Unfortunately, the textures do not allow an unambiguous determination of the liquid crystalline phases. Therefore, small-angle X-ray scattering diagrams are recorded at 20 and 110 °C. As shown in Fig. 72, at 20 °C seven reflections are found in the small-angle scattering curve of HBC. This pattern is interpreted as a columnar structure with a two-dimensional centered superstructure (Fig. 71). The columns are aligned parallel, where the aromatic cores of HBC form stacks and are tilted with respect to the column axis. The indices of the reflections and the observed and calculated reflex positions are given in the literature [139]. On the basis of these

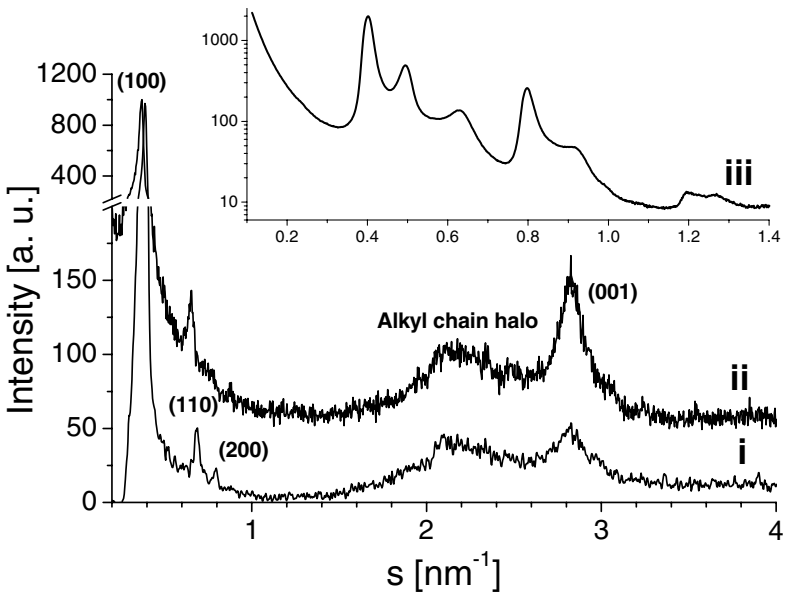

Fig. 72. The X-ray diffraction of HBC (curve i) and that of complex PEIC22–HBC (curve ii) in the hexagonal mesophase at 110 °C. The (001)-reflection of PEIC22–HBC is more intense than that of HBC indicating a higher stacking order of aromatic cores for PEIC22–HBC than that of HBC. The inset shows the small-angle X-ray scattering of compound HBC at 20 °C (curve iii), which is due to a rectangular centered columnar phase. Reprinted with permission form J Mater Chem 1999; 9:1056 © The Royal Society of Chemistry [139].

values the lattice parameters are determined to be 4.04 and 3.18 nm, giving an inter-columnar distance of 2.57 nm. A tilt angle between the plane normal to the aromatic cores aligned and the column direction is calculated to be about 38°. The SAXS diagram of complex PEIC22–HBC shows a reflection pattern very similar to that of HBC, but with broader reflections.

It can be concluded that both materials have the same liquid crystalline rectangular columnar structure at room temperature, although differing in the lateral packing of the columns, which appears to be better in HBC compared to PEIC22–HBC. At a temperature of 110 °C, in the small-angle X-ray region of HBC and PEIC22–HBC three reflections are found with relative positions of $1{:}\sqrt{3}{:}2$. This can be interpreted as an ordered columnar structure with a hexagonal superstructure as is found is alkylated non-functionalized hexa-*peri*-hexabenzocorones [142]. From the reflex positions, inter-columnar distances of 3.00 nm (HBC) and 3.12 nm (PEIC22–HBC) are determined. Again, the small-angle reflections observed for PEIC22–HBC are broader than for HBC, but the (001) reflection located in the wide-angle region is significantly smaller for the complex than for the free acid (Fig. 72). The inter-columnar distances derived from the (001) reflection for both are the same ($d_{\text{intra}} = 0.354$ nm). This value is nearly the same as found earlier for non-functionalized hexa-*peri*-hexabenzocoronene [142] and indicates an effective $\pi-\pi$-overlap of the adjacent cores [138].

For quantification of the difference between the inter-columnar ordering and intra-columnar ordering of HBC and PEIC22–HBC, the correlation lengths are calculated from the widths of the (100) and the (001) reflections. The correlation lengths of (HBC) are 45 and 3.7 nm for the inter- and intra-columnar long-range ordering, respectively. For PEIC22–HBC the corresponding values are 33 and 5.7 nm. Thus, the inter-columnar order in the pure compound is higher than in the complex, whereas the intra-columnar

long-range order of the pure substance is lower than in the complex. For a desired rapid charge transport along the columns, the π–π-overlaps and the intra-columnar long-range ordering are essential properties. Since the π–π-overlap of HBC and PEIC22–HBC are equal, but the intra-columnar long-range order of PEIC22–HBC is better, a higher charge transport may be expected for PEIC22–HBC than for HBC.

4.1.2. Mechanical properties

In addition to the control of the mesomorphic structure, the mechanical properties play a key role in estimating the potential of HBC and HBC-PEI as promising materials. It is known for many polyelectrolyte–surfactant complexes that the mechanical properties are significantly improved by the polymeric compound [143]. Hence such an improvement for the complexation of HBC can also be expected.

The shear modulus G of films, prepared by solvent casting of HBC and PEIC22–HBC, is determined by temperature-dependent dynamic-mechanical measurements. It is found for the pure substance and the complex that the shear modulus of the rectangular columnar phase is one order of magnitude higher than that of the hexagonal columnar phase. Below the phase transition, values of G in the range between 1 and 10 MPa are measured for HBC and PEIC22–HBC. Above the phase transition, G is about 0.1 MPa. The different behavior of loss-angle δ as shown in Fig. 73 is different. It can be seen that δ increases from 5 to 40° in the range from 20 to 130 °C for HBC, whereas δ increases only from 10 to 20° in the same temperature range for PEIC22–HBC. This means that HBC is more elastic at room temperature and viscous at higher temperatures. On the other hand, PEIC22–HBC shows an approximately constant elasticity over the whole temperature range. This may be explained by considering PEIC22 as a kind of cross-linker, which forms a flexible three-dimensional network bound ionically to HBC.

In conclusion it is found that the carboxylic acid functionalized hexabenzocoronene HBC forms two columnar liquid crystalline structures. At room temperature a rectangularly centered symmetry is found,

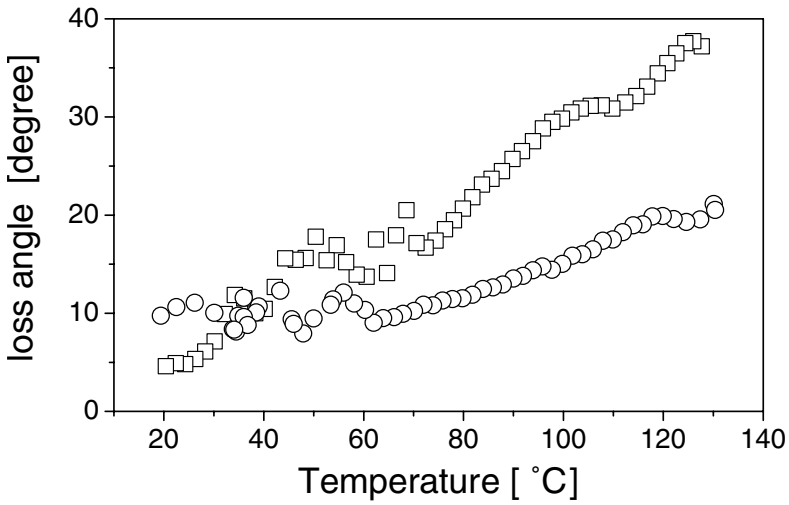

Fig. 73. Temperature dependent loss-angle determined by dynamic-mechanical measurements of (b) (squares) and of (c) (circles). The shear rate is 0.1 s^{-1}. Reprinted with permission form J Mater Chem 1999; 9:1056 © The Royal Society of Chemistry [139].

which changes to a hexagonal ordered columnar structure at temperatures higher than 93 °C. In addition the complexation of HBC in chloroform with a hydrophobic modified polyethyleneimine gives a stoichiometric complex similar to solid waterborne polyelectrolyte–surfactant complexes. For the stoichiometric complex of PEIC22 and HBC resulting in PEIC22–HBC, the same columnar liquid crystalline phases are present, but with a lower phase-transition temperature (70 vs. 93 °C) and a lower hysteresis (18 vs. 31 °C), observed for the phase-transition temperature between heating and cooling. Furthermore, the intra-columnar order of the complex is higher than that of the non-complexed specimen, whereas the inter-columnar order is lower. From the temperature dependence of the loss-angle, it is concluded that the elasticity of HBC can be improved by complexation, probably without the danger of reducing its high carrier mobilities.

4.2. Polysiloxane hexa-peri-hexabenzocoronene [144]

This section reports on a complex which is formed by HBC and an amino-functionalized polysiloxane. The complexation of the aminoethylaminopropyl functionalized polysiloxane PDMA with the hexa-*peri*-hexabenzocoronene HBC to complex PDMS-HBC is schematically shown in Fig. 74 and has been monitored by IR-spectroscopy. A strong carboxylic acid vibration band at 1710 cm^{-1} is present in the sum of the FTIR spectra of PDMS and HBC, while it is absent in the spectrum of PDMS-HBC. The other vibrations of both spectra are identical and identified as the C=C stretch vibrations around

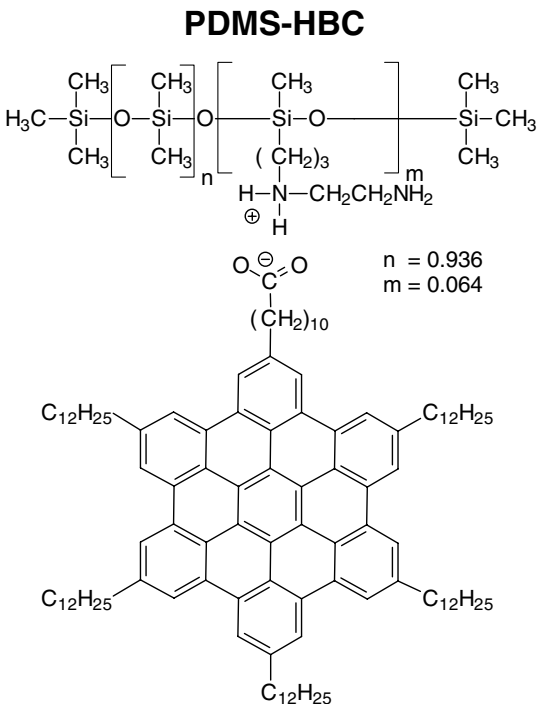

Fig. 74. The molecular structure of an ionically bound complex PDMS–HBC formed by an aminoethylaminopropyl functionalized polysiloxane (PDMS) and a hexabenzocoronene (HBC). PDMS and HBC are not drawn. HBC is functionalized by a carboxylic acid function which serves as an anchor group. Reprinted with permission form J Mater Chem 2000;10(6):1326 © The Royal Society of Chemistry [144].

1600 cm^{-1}, the CH_2 symmetric (scissors) and the CH_3 asymmetric deformation vibrations are located at 1460 cm^{-1}. Further, the CH_3 symmetric (umbrella) deformation is at 1260 cm^{-1}. From this it is concluded that, within the experimental error, all of the carboxylic acid functions of HBC form acid–base pairs with the amino functions of PDMS in the complex.

4.2.1. Nanostructures

ten Brinke et al. [145] have reported on lamellar structures of comb copolymer-like systems obtained by hydrogen bonding between polymers containing basic moieties and surfactants. Their complexes are similar to PDMS-HBC with respect to their molecular interactions. In the previous section, it is shown that the HBC form columnar polymer complexes, which contain about 9% (w/w) of a hydrophobically modified polyethyleneimine [139]. Here, the polymer content of PDMS-HBC is much higher (46% (w/w)). Therefore, new columnar morphologies of PDMS-HBC, compared to those of the earlier complex, should be expected. Temperature-dependent small-angle X-ray diffraction has been used to investigate its supramolecular ordering. As expected, a number of reflections are present in the scattering curves (Figs. 75 and 76), but it is surprising that more and sharper reflections are found at 120 °C (Fig. 76) than at 20 °C (Fig. 75). Obviously a hexagonal columnar phase, which is typical for hexa-peri-hexabenzocoronene compounds [146], can be excluded.

The most simple models which explain the reflection positions and their relative intensities are two-dimensional oblique lattices of columnar phases: Col_1 which is stable at room temperature and Col_2 which is stable at higher temperatures. For the lattice constants $a = b = 5.0$ nm and $\gamma = 112°$ for Col_1 are calculated and $a = b = 5.5$ nm and $\gamma = 108°$ for Col_2. The areas of the unit cells are 23.2 nm^2 (Col_1) and 28.8 nm^2 (Col_2). It is striking that the scattering intensity of the reflections at lower scattering

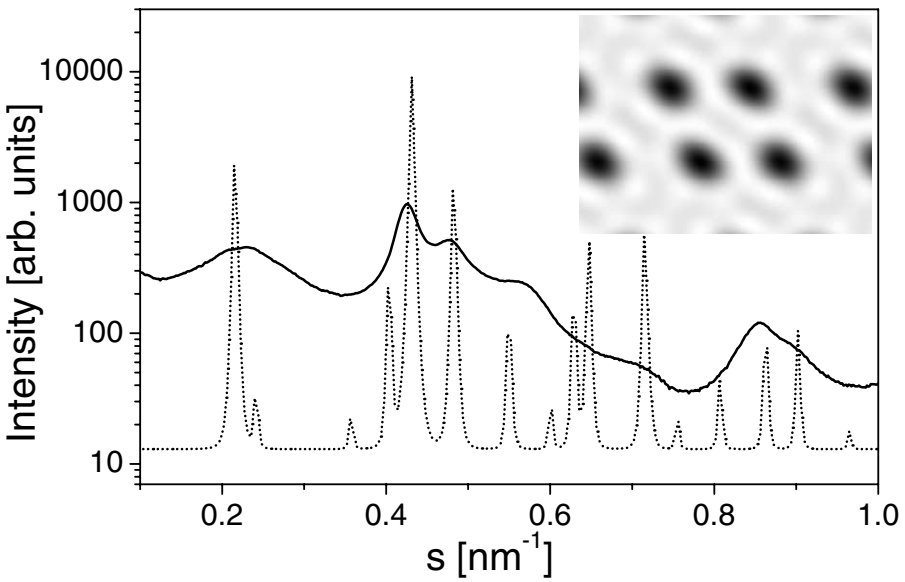

Fig. 75. Small-angle X-ray scattering of compound PDMS–HBC in the Col_1 phase at 20 °C (solid line). The dashed line is a calculated scattering curve of the columnar phase, which corresponds to the calculated density profile of the inset with four columns per unit cell. The cell parameters are $a = b = 5.0$ nm and $\gamma = 112°$. The discs have a tilt angle of about 45° in relation to the column axis. Reprinted with permission form J Mater Chem 2000;10(6):1326 © The Royal Society of Chemistry [144].

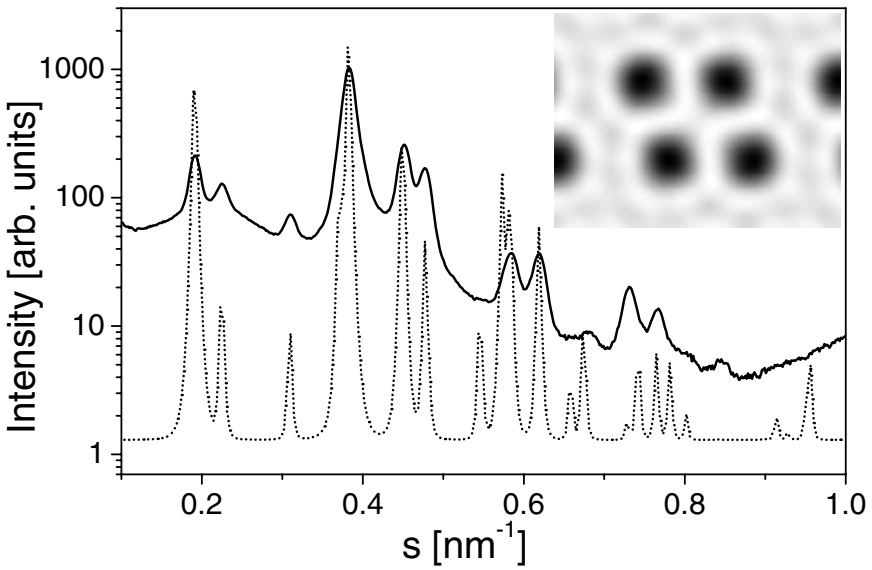

Fig. 76. Small-angle X-ray scattering of compound PDMS–HBC in the Col_2 phase at 120 °C (solid line). The dashed line is a calculated scattering curve of the phase, which corresponds to the calculated density profile of the inset with four columns per unit cell. The cell parameters are $a = b = 5.5$ nm and $\gamma = 108°$. The discs are not tilted. Reprinted with permission form J Mater Chem 2000;10(6):1327 © The Royal Society of Chemistry [144].

vectors (around 0.2 nm^{-1}) is lower than that of the group of reflections around 0.4 nm^{-1}. This is explained by an arrangement of four columns per unit cell, which group around the center of the unit cell (see insets of Figs. 75 and 76: The corresponding analytical scattering curves are shown as dashed lines). Lists of the measured and calculated reflex positions and Miller indices are given in the literature [144]. The normals of the aromatic planes within Col_1 are tilted with respect to the column axes. The tilt angle is about 45° which gives an axis ratio of 1:0.7 for the in-plane projection. Within the Col_2 phase the normals of the column axis are aligned parallel to the column axis. It has been observed, for the complex of HBC with a polyethyleneimine, that the normals of the aromatic cores are tilted at lower temperatures but are parallel at higher temperatures (Section 4.1.1).

Explanations for the reduced symmetry of Col_1 and Col_2 compared to the expected hexagonal and rectangular structures may be packing constraints, because the carboxylic acid function is linked ionically to the polysiloxane and it reduces the molecular symmetry from D_{6h} to C_{2v}. Further the alkylated chains and the siloxane chains are not miscible and therefore, together with the aromatic cores, the complex contains three incompatible elements, which lead to micro-segregation. The situation may be considered to be similar to that of triblock copolymers where the formation of mesomorphous structures is controlled by the relative incompatibilities of the three polymeric components of the block copolymers [147]. It is surprising that, from the widths of the reflex positions, the supramolecular order of Col_2 is better than in Col_1. From the width of the most intensive reflection (index 200), the in-plane correlation length of Col_1 is about 50 nm (20 °C) and that of Col_2 is about 150 nm (120 °C). The reason for the better order within the higher temperature phase than in the lower temperature phase may be that the intra-columnar stacking order of the tilted arrangement is not as good as it is in the non-tilted case. In order to prove this assumption the molecular order has been investigated using wide-angle X-ray scattering. It can be seen in Fig. 77 (curve c) that, in addition to two broad reflections at $s = 1.32$ and

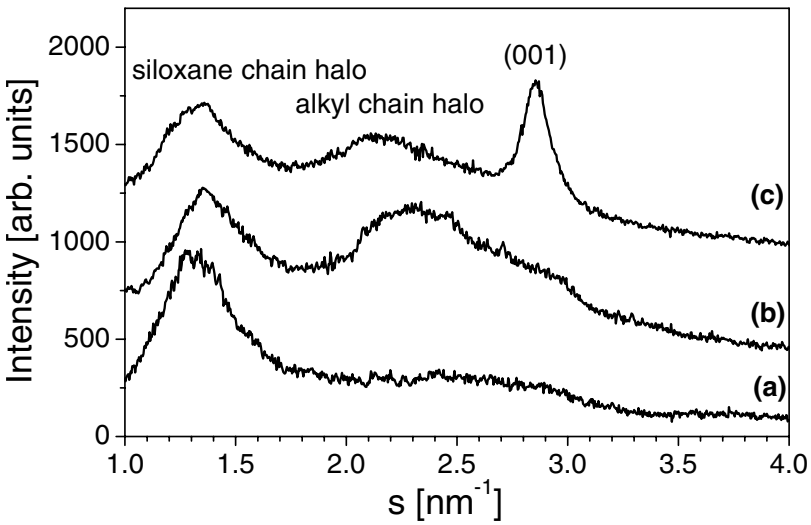

Fig. 77. Wide-angle X-ray scattering of the polysiloxane (curve a), the Col_1 phase at 20 °C (curve b) and the Col_2 phase at 120 °C (curve c). Reprinted with permission form J Mater Chem 2000;10(6):1327 © The Royal Society of Chemistry [144].

2.30 nm^{-1}, a relatively sharp reflection is present at $s = 2.86\ nm^{-1}$ in the diagram of Col_2 at 120 °C (Bragg distances are 0.76, 0.46 and 0.35 nm). The first reflection is attributed to the short-range order of the siloxane segments.

For clarity, the wide-angle scattering of the pristine siloxane is shown in Fig. 77 (curve a). It can be seen there that in the scattering curve of the siloxane only one reflection is present at about the same position (1.32 nm^{-1}) as the first wide-angle reflection of Col_1. The reflection at $d = 0.46$ nm is attributed to the scattering of the alkyl chains which is typically found in polyelectrolyte–surfactant complexes with a mesomorphous structure (e.g. the complexes of polystyrenesulfonate with alkyltrimethylammonium surfactants [100]). The relatively sharp reflection with $d = 0.35$ nm defines the intra-columnar distance. This value is the same as that of graphite (0.335 nm) and indicates a strong π–π overlapping of the adjacent hexa-*peri*-hexabenzocoronene discs in the Col_2 phase, which is consistent with the supramolecular model derived from the small-angle scattering data. In the wide-angle diagram of Col_1 two broad reflections are found at about the same position (1.35, 2.33 nm^{-1}) and with the same width as for Col_2 (Fig. 77, curve b). Therefore, Col_1 and Col_2 are very similar in the molecular order of their siloxane and alkyl chains, which is only of short-range. But in contrast to Col_2 only a weak reflection is present in the region around 3 nm^{-1} which is characteristic for an intra-columnar ordering. Therefore, it is concluded that the intra-columnar order within Col_1 is much weaker than within Col_2. From a curve fitting of Lorentzian profiles onto the scattering curves (not shown), the intra-columnar correlation length of Col_1 is 2 nm, whereas that of Col_2 is 8 nm. This agrees with the structure model of Col_1 with tilted discs (Fig. 75 inset) which shows a lower π–π-overlapping than within the columns of Col_2.

In order to confirm the proposed model of extended columns, the structure is visualized by electron microscopy [144, page 1328]. Patterns of dark and bright stripes are found in samples prepared in thin sections. The average distance of equal stripes is about 2.3 nm. The bright lines are attributed to columns of hexabenzocoronene and the dark ones to their surrounding matrix of polysiloxane, which has a higher electron density. The cut along the columns is explained as a result of the fact that these are the directions

with the lowest mechanical strength and that these are preferred because the siloxane matrix remains soft even at lower temperatures. Surprisingly, as a consequence of the complexation, the patterns are almost free of dislocations. And from the length of the stripes the average column height is estimated to be at least 200 nm. This is more than 100 times the column diameter (1.4 nm). Probably, their height is significantly larger. This remarkable height of defect-free columns results from the polysiloxane which prevents the columns from breaking off. In combination with the rapid charge transport of such materials [138] this seems to be very promising for electronic devices such as graphitic nanowires. Their electronic properties can, in principle, be modified by different substituents or by intercalation of low molecular weight molecules. Knowledge of graphite and carbon fiber intercalation compounds [148] can be used for the modification of the electrical properties of these quasi-graphitic nanowires. According to current knowledge, the complex of PDMS-HBC is capable of forming the highest known intra-columnar order of discotic mesophases reported to date. Very high correlation lengths of two-dimensional lattices in hexagonal columnar phases, greater than 400 nm, have already been described [149].

4.2.2. Thermal and mechanical properties

The thermal and the mechanical properties of PDMS-HBC are investigated by DSC and dynamic mechanical analysis. Typical DSC traces for heating and cooling scans, measured with a heating rate of 10 K/min, are given in Fig. 78. An exothermic transition with a maximum at 85 °C is found upon heating to have a width of 16 °C (lower temperature onset at 76 °C, higher temperature onset at 92 °C). After cooling the transition is found to be at a maximum at 57 °C and at a width of 16 °C (left onset at 46 °C, higher temperature onset at 62 °C). The large hysteresis of the transition at a width of 30 °C indicates that the bulky aromatic cores are involved in the transition, their reorientation is known to show slow kinetics [139].

This transition is assigned to the order–order transition from Col_1 to Col_2, which is similar to that reported on in the previous section on a complex of HBC with a hydrophobically modified

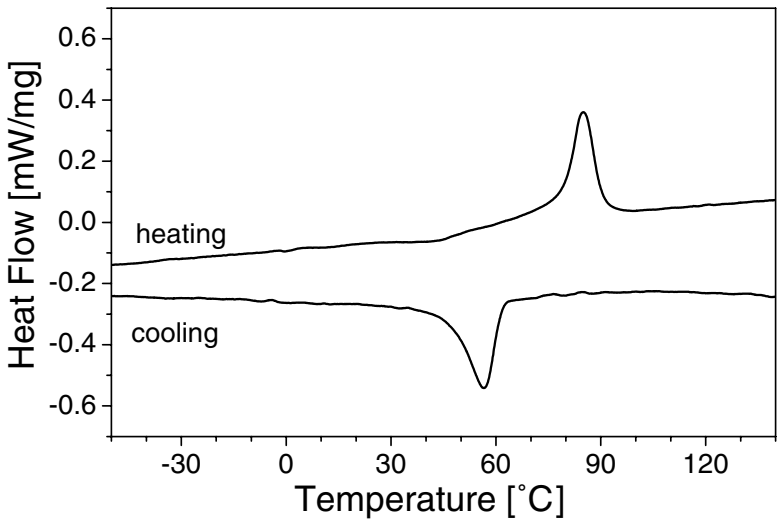

Fig. 78. DSC traces of complex PDMS–HBC while heating and cooling. The exothermic transition at 85 °C in the heating scan and the endothermic transition at 57 °C indicate a reversible order–order transition form a column phase Col_1 to a column phase Col_2. Reprinted with permission form J Mater Chem 2000;10(6):1328 © The Royal Society of Chemistry [144].

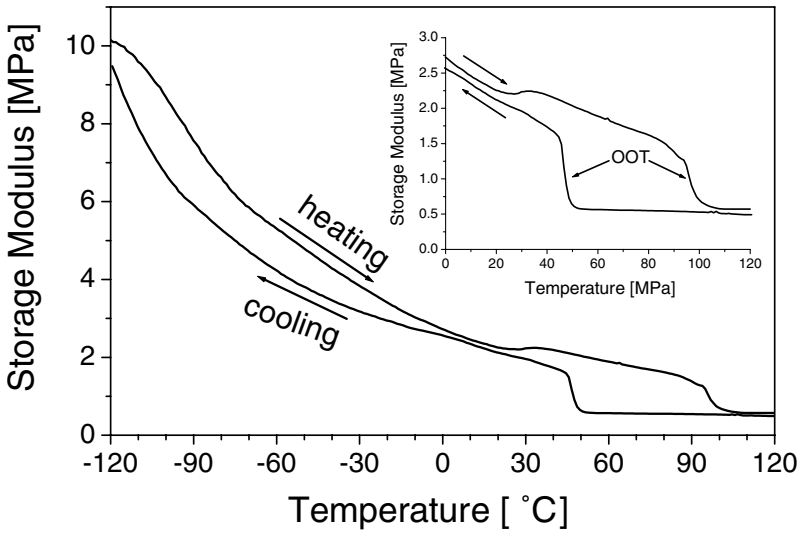

Fig. 79. Storage shear modulus of complex PDMS–HBC while heating and cooling. The inset shows a magnification in the region of the columnar order–order transition. Reprinted with permission form J Mater Chem 2000;10(6):1328 © The Royal Society of Chemistry [144].

polyethyleneimine [139]. The influence of the temperature on the storage shear modulus can be seen in Fig. 79. At − 120 °C the modulus is in the range 9–10 MPa, at 0 °C it is in the range 2.5–2.7 MPa and at 30 °C it is 2.0–2.2 MPa. During further heating a step-like decrease of the modulus from 1.5 to 0.6 MPa is found with the point of inflection at 95 °C. During heating a step-like increase of the same height can be seen whose point of inflection is at 46 °C.

The step-like decrease of the modulus during heating has the same position as the high temperature onset of the peak in the DSC heating trace (92 °C), and the step-like decrease during cooling has the position of the low temperature onset of the peak in the DSC curve (46 °C). From this it is concluded that the origin of the transition found in DSC is the same as in the shear modulus. Further from the positions of the transitions it is concluded that the transition from Col_1 to Col_2 must be almost thermally completed before it becomes mechanically effective. An origin of the small step seen in Fig. 79 on the heating scan at around 30 °C, which cannot be observed on the cooling scan or in the DSC curve, is not yet clear. The mechanical properties identify PDMS-HBC in the Col_1 phase as a highly flexible material whose modulus decreases smoothly to a factor of 5 in the range from − 120 to 90 °C. The Col_2 phase is even more flexible. The flexibility of the complex over a wide range of temperatures can be attributed to the relatively high polysiloxane content which acts as a soft segment in the mesophase. The mechanical properties of the material may be improved by cross-linking reactions, which have already been established in the chemistry of polysiloxanes. Examples of effective cross-linking catalysts are heavy metal compounds such as dibutyltin dilaurate.

In summary, it has been shown that the complexation of carboxylic acid functionalized hexa-*peri*-hexabenzocoronene with a commercially available polysiloxane results in a hybrid material which shows highly ordered columnar phases. The columns are remarkably long, and the structures are essentially free from defects. The material is highly elastic over a wide range of temperatures and could function well as a basic material for molecular nanowires.

5. Summary and outlook

It has been shown in this review that polyelectrolytes and surfactants can be used as versatile building blocks for the design of functionalized polyelectrolyte–surfactant complexes with a great variability of nanostructures. Useful surfactants are fluorinated surfactants and functionalized disk-shaped molecules. The nanostructures of these complexes in their forms as bulk material, ultra-thin films on surfaces, and nanoparticles are the result of the self-assembly of the complexes.

The use of fluorinated surfactants makes possible the design of complexes with different lamellar morphologies including flat, undulated and perforated lamellar structures with repeat units well below 10 nm. The perforation density within the lamellae can be controlled by the charge density of the polyelectrolyte. When the charge density increases, then the perforation density too increases. The polyelectrolyte–fluorinated surfactant complexes (PEFA) are capable of forming surfaces of low and ultra-low surface energies. Critical surface tensions as low as 6 mN/m are typical values for some of these complexes. Surfaces of these complexes show outstanding oil-repellent properties, which are independent of their thickness. In contact with water, the surfaces of PEFA complexes show a reversible surface reconstruction resulting in an increase of the surface energies to values of about 30 mN/m. Thin and ultra-thin films of PEFA complexes of high homogeneity can be formed in a single-step procedure. Their thickness ranges from about 370 down to 5.7 nm. These films are built from macroscopically oriented stacks of alternating ionic and non-ionic layers and their wetting behavior is almost independent of their thickness. Surface energies of complex films can be tuned in the range 9–19 mN/m by varying the length of the fluorinated moieties.

PEFAs with discotic columnar nanostructures can be produced by the complexation of long-chain fluorinated surfactants. Diazosulfonate functionalized polymers can be used to prepare super-strongly segregated lamellar nanostructures and ultra-low energy surfaces forming PEFA complexes. Thin films of these complexes may be useful as possible information storage systems if the pulse of a laser beam can switch the surface energy.

Nanoparticle systems of PEFAs have been designed for the preparation of waterborne PEFA surfaces. It has been demonstrated that PEFAs show internal nanostructures not only in their form as bulk materials, but also that nanoparticles of the PEFAs themselves, with sizes around 300 nm, contain internal lamellar smectic A-like structures with repeat units around 3 nm. A comparison of silicon surfactant containing complexes with the PEFA complexes revealed that both are capable of forming ordered nanostructures, but PEFAs are superior in their wetting properties. After changing the polymeric backbone from carbon to siloxane, it is possible to use their self-assembling properties to form a stable surface in a salt-solution that is both highly oil- and water-repellent.

For future developments such polysiloxane–fluorinated surfactant complexes and PEFAs may be prove useful in forming non-toxic anti-fouling and biocompatible surfaces that actively stabilize the secondary structure of blood proteins. Furthermore, nanoparticles of PEFA are shown to be able to dissolve amyloid plaques in animal cell tissues [150]. This opens a wide area of possible applications of PEFAs and polysiloxane–fluorinated surfactant complexes for medical, biological and pharmacological applications. In this context, it is worthwhile to mention that many of the self-assembled PEFA nanostructures resemble the structures of natural membranes. This analogy to biological systems is important for possible future applications. In the direct neighborhood of highly ionic segments, perfluorinated chains could play a key role in the development of attractive applications of PEFA complexes for life science purposes.

In the third part of this review, the use of polyelectrolytes with conjugated backbones of the poly(*p*-phenylene) and poly(phenyleneethynylene) type result in highly optically active complexes. As for PEFAs, the self-assembly of the complexes results in ordered nanostructures of the lamellar and of the columnar type. The nanostructures of the optically active complexes are formed in a single-step in both the bulk materials as well as in thin films. This is an advantage, from the material science point of view, when thinking about the use of new materials in optoelectronic devices such as LEDs. In contrast to the optically active complexes created here, other ordered nanostructures with optical activities, such as Langmuir–Blodgett films, have to be prepared in multi-step procedures. The Langmuir–Blodgett technique does, indeed, allow for a high control of the structure formation at every step of the layer deposition. It is, however, a time-consuming process that reduces the attractivity of Langmuir–Blodgett films for the development of optoelectronic devices. The same holds for other layer-by-layer deposition techniques. Therefore, the possibility of deposing strongly and super-strongly segregated multi-layers of optically active compounds in a single step procedure in a way that semiconductor and isolator layers are separated on a nanometer scale seems to be a very attractive feature for the development of smart optical materials.

The fourth part of this review has shown that it is possible to produce columnar discotic complexes of carboxylic acid functionalized hexa-*peri*-hexabenzocoronenes. The hexa-*peri*-hexabenzocoronene complexes of a hydrophobically modified polyethyleneimine and an amino functionalized polysiloxane are thermotropic liquid crystals. In comparison to the non-complexed hexa-*peri*-hexabenzocoronene, it has been seen that the height of the columns are greatly increased and also that the mechanical properties can be improved by the complexation. These columnar complexes could be used as organic nanowires.

Acknowledgments

It is my great pleasure to thank the director of the Max Planck Institute of Colloids and Interfaces, Markus Antonietti. His sound advice and our frequent discussions are of outstanding importance for this work.

My research would not have been possible without the generous financial support of the Max Planck Society, the ‘Deutsche Forschungsgemeinschaft’ (Grants TH633/2-1, Lo418/7-1 and JA555/6-1) and the Fraunhofer Society. I am deeply indebted to these organizations.

I am also most grateful to all former and present members of the polyelectrolyte–surfactant complexes research group at the Max Planck Institute of Colloids and Interfaces. I am pleased to acknowledge the contributions of Antje Wenzel, Susanne Henke, Carmen Remde, Jochen Beyermann, Dirk Ruppelt and Sascha General. I would also like to extend my thanks to Peter Cowap for carefully reading, correcting and helping to formulate the English language of the text before publication.

References

[1] Tomalia DA, Wang ZG, Tirrell M. Experimental self-assembly: the many facets of self-assembly. Curr Opin Colloid Interf Sci 1999;4(1):3–5.

[2] Tredgold RH. Order in thin organic films. Cambridge: Cambridge University Press; 1994.

[3] Ruland W. Private communication.

[4] Micha MA, Burger C, Antonietti M. Generalized phase diagram for microphase separated systems and its determination by small-angle scattering. Macromolecules 1998;31(17):5930–3.
[5] Stribeck N, Ruland W. Determination of the interface distribution function of lamellar two-phase systems. J Appl Cryst 1978;11:535–9.
[6] Siemann U, Ruland W. Determination of the width of the domain boundaries in polymer two-phase systems by X-ray small-angle scattering. Colloid Polym Sci 1982;260:999–1010.
[7] Wolff T, Burger C, Ruland W. Small-angle X-ray scattering study of lamellar microdomains in diblock copolymers in the weak segregation regime. Macromolecules 1994;27:3301–9.
[8] Ruland W. The evaluation of the small-angle scattering of lamellar two-phase systems by means of interface distribution functions. Colloid Polym Sci 1977;255:417–27.
[9] Ober CK, Wegner G. Polyelectrolyte–surfactant complexes in the solid state—facile building blocks for self-organizing materials. Adv Mater 1997;9(1):17–31.
[10] Antonietti M, Burger C, Thünemann A. Polyelectrolyte–surfactant complexes: a new class of highly ordered polymer materials. TRIP 1997;5:262–7.
[11] Antonietti M, Thünemann A. Polyelectrolyte–lipid complexes as membrane mimetic systems. Curr Opin Colloid Interf Sci 1996;1:667–71.
[12] Antonietti M, Henke S, Thünemann A. Highly ordered materials with ultra-low surface energies: complexes with fluorinated surfactants. Adv Mater 1996;8:41–5.
[13] Goddard ED. Polymer–surfactant interaction. Part II. Polymer and surfactant of opposite charge. Colloids Surf 1986;19: 301–29.
[14] Hayakawa K, Kwak JCT. Surfactant–polyelectrolyte interactions. 1. Binding of dodecyltrimethylammonium ions by sodium dextran sulfate and sodium poly(styrenesulfonate) in aqueous solution in the presence of sodium chloride. J Phys Chem 1982;86(16):3866–70.
[15] Hayakawa K, Kwak JCT. Study of surfactant–polyelectrolyte interactions. 2. Effect of multivalent counterions on the binding of dodecyltrimethylammonium ions by sodium dextran sulfate and sodium poly(styrenesulfonate) in aqueous solution. J Phys Chem 1983;87(3):506–9.
[16] Semenov AN, Nyrkova IA, Khokhlov AR. Polymers with strongly interacting groups—theory for nonspherical multiplets. Macromolecules 1995;28(22):7491–500.
[17] Thünemann AF. Nano-structured materials with low surface energies formed by polyelectrolytes and fluorinated amphiphiles (PEFA). Polym Int 2000;49:636–44.
[18] Lochhaas KH, Thünemann AF, Antonietti M. Polyelectrolyte–surfactant complexes with fluorinated surfactants: a new type of material for coatings. JOCCA—Surf Coatings Int 1999;82(9):451–5.
[19] Li D, Neumann AW. Contact angles on hydrophobic solid surfaces and their interpretation. J Colloid Interf Sci 1992; 148(1):190–200.
[20] Kwok DY, Neumann AW. Contact angle measurement and contact angle interpretation. Adv Colloid Interf Sci 1999; 81(3):167–249.
[21] Thünemann AF, Lochhaas KH. Self-assembly of perfluorodecanoic acid with cationic copolymers—ultra-low energy surfaces and mesomorphous structures. Langmuir 1998;14(17):4898–903.
[22] Thünemann AF, Lieske A, Paulke BR. Low surface energy coatings from waterborne nano-dispersions of polymer complexes. Adv Mater 1999;11(4):321–4.
[23] Information supplied by the manufacturer, BASF. Specialty chemicals. Ludwigshafen, Germany.
[24] Information supplied by the manufacturer, Hoechst AG, Frankfurt, Germany.
[25] Thünemann AF, Beyermann J, Ferber C, Löwen H. Immobilization of retinoic acid by polyamino acids: lamellar-structured nanoparticles. Langmuir 2000;16(2):850–7.
[26] Hare EF, Shafring EG, Zisman WA. Properties of films of adsorbed fluorinated acids. J Colloid Sci 1954;58:236–9.
[27] Girifalco LA, Good RJ. A theory for the estimation of surface and interfacial energies. I. Derivation and application to interfacial tension. J Phys Chem 1957;61:904–10.
[28] Fowkes FM. J Phys Chem 1962;66:382.
[29] Fowkes FM. Contact angle, wettability and adhesion. Adv Chem Ser, Am Chem Soc 1964;43:108.
[30] Wang J, Ober CK. Self-organizing materials with low surface energy—the synthesis and solid-state properties of semifluorinated side-chain ionenes. Macromolecules 1997;30(24):7560–7.

[31] Yasuda H, Okuno T, Sawa Y, Yasuda T. Surface configuration change observed for Teflon–PFA on immersion in water. Langmuir 1995;11(8):3255–60.
[32] Thünemann AF, Lochhaas KH. Surface and solid-state properties of a fluorinated polyelectrolyte–surfactant complex. Langmuir 1999;15(4):4867–74.
[33] Neinhuis C, Barthlott W. Characterization and distribution of water-repellent, self-cleaning plant surfaces. Ann Bot 1997;79(6):667–77.
[34] Barthlott W, Neinhuis C. Purity of the sacred lotus, or escape from contamination in biological surfaces. Planta 1997; 202(1):1–8.
[35] Onda T, Shibuichi S, Satoh N, Tsujii K. Super-water-repellent fractal surfaces. Langmuir 1996;12(9):2125–7.
[36] Thünemann AF, Lochhaas KH. Colloidal complexes of perfluorooctadecanoic acid with cationic copolymers. Langmuir 1999;15(2):6724–7.
[37] Thünemann AF, Schnablegger H. Monodisperse disk-shaped micelles of perfluorooctadecanoic acid. Langmuir 1999; 15(16):5426–8.
[38] Wagner R, Richter L, Wu Y, Weißmüller J, Kleewein A, Hengge E. Silicon-modified carbohydrate surfactants. VII. Impact of different silicon substructures on the wetting behaviour of carbohydrate surfactants on low-energy surfaces—distance decay of donor–acceptor forces. Appl Organomet Chem 1998;12(4):265–76.
[39] Hoffmann H. From micellar solutions to liquid crystalline phases. Ber Bunsenges Phys Chem 1984;88:1078–92.
[40] Holmes MC, Reynolds DJ, Boden N. Concentration–temperature dependence of the size and shape of the micelles in the cesium pentadecafluoroacetadecanoate/water system. J Phys Chem 1987;91:5257–62.
[41] Dombroski JP, Edwards PJB, Jolley KW, Boden N. Phase diagram of the tetramethylammonium heptadecafluorononoate (TMAHFN)D2O system as determined by H-2 and N-14 NMR. Liquid Cryst 1995;18(1):51–60.
[42] Herbst L, Hoffman H, Kalus J, Reizlein K, Schmelzer U, Ibel K. Small angle neutron scattering on nematic lyotropic liquid crystals. Ber Bunsenges Phys Chem 1985;89:1050–64.
[43] Thünemann AF, Kubowicz S, Pietsch U. Ultrathin solid polyelectrolyte–surfactant complex films: structure and wetting. Langmuir 2000;16(23):8562–7.
[44] Overberger CG, Menges G, Kroschwitz JI, 2nd ed. Encyclopedia of polymer science and engineering, vol. 1. New York: Wiley; 1985. p. 689.
[45] Augsburg A, Grundke K, Pöschel K, Jacobasch HJ, Neumann AW. Determination of contact angles and solid surface tensions of poly(4-*x*-styrene) films. Acta Polym 1998;49(8):417–26.
[46] Dessipri E, Tirrell DA, Atkins EDT. Fluorinated poly(alpha, L-glutamate)s. Macromolecules 1996;29(1):3545–751.
[47] Seperati CA. Physical constants of fluorpolymers, 3rd ed. New York: Wiley; 1996.
[48] Thünemann AF, Ruppelt D, Blaul J. Rigid-rod complex of a cationic poly(*p*-phenylene) and a fluorinated amphiphile. Macromolecules 2000;33(6):2124–8.
[49] Chen HL, Hsiao MS. Self-assembled mesomorphic complexes of branched poly(ethyleneimine) and dodecylbenzene-sulfonic acid. Macromolecules 1999;32(9):2967–73.
[50] Hwang MJ, Kim K. Poly(ethyleneimine) as a subphase stabilizer of stearic acid monolayers at the air water interface: surface pressure–area isotherm and infrared spectroscopy study. Langmuir 1999;15(10):3563–9.
[51] Holy V, Pietsch U, Baumbach T. Springer tracts in modern physics. High-resolution X-ray scattering from thin films and multilayers, vol. 149. Berlin: Springer; 1999.
[52] Parrat L. Surface studies of solid surfaces by reflections of X-rays. Phys Rev 1954;95:359.
[53] Thünemann AF. Complexes of polyethyleneimine with perfluorinated carboxylic acids: wettability of lamellar structured mesophases. Langmuir 2000;16(2):824–8.
[54] Schulman F, Zisman WA. The spreading of liquids on low-energy surfaces. V. Perfluorodecanoic monolayers. J Colloid Sci 1952;7:465–81.
[55] Höpken J, Möller M. Low surface energy polystyrene. Macromolecules 1992;25(5):1461–7.
[56] Sheiko S, Lermann E, Möller M. Self-dewetting of perfluoroalkyl methacrylate films on glass. Langmuir 1996;12(16): 4015–24.
[57] Fox HW, Zisman WA. The spreading of liquids on low energy surfaces. I. Polytetrafluorethylene. J Colloid Sci 1950;5: 514–31.
[58] Bunn CW, Howells ER. Structures of molecules and crystals of fluorocarbons. Nature 1954;174:549–51.

[59] Antonietti A, Kublickas R, Nuyken O, Voit B. Polyelectrolyte–surfactant complexes containing photolabile diazosulfonate chromophores. Macromol Rapid Commun 1997;18(4):287–94.
[60] Thünemann AF, Schnöller U, Nuyken O, Voit B. Self-assembled complexes of diazosulfonate polymers with low surface energies. Macromolecules 1999;32(22):7414–21.
[61] Stasko A, Erentova K, Rapta P, Nuyken O, Voit B. Investigation of the decomposition of compounds containing azo groups by EPR spectroscopy. Magn Reson Chem 1998;36(1):13–34.
[62] Grazulevicius JV, Soutar I, Swanson L. Photophysics of carbazole-containing systems. 3. Fluorescence of carbazole-containing oligoethers in dilute solution. Macromolecules 1998;31(15):4820–7.
[63] Thünemann AF, Schnöller U, Nuyken O, Voit B. Diazosulfonate polymer complexes: structure and wettability. Macromolecules 2000;33(15):5665–71.
[64] Klug HP, Alexander LE. X-ray diffraction procedures for polycrystalline and amorphous materials. New York: Wiley; 1974. p. 487.
[65] Pan FM, Lin YL, Horng SR. Decomposition of perfluorpolyethers during XPS measurements. Appl Surf Sci 1991;47: 9–16.
[66] Thünemann AF, Lochhaas KH. Self-assembly of solid polyelectrolyte–silicon–surfactant complexes. Langmuir 1998; 14(21):6220–5.
[67] Owen MJ. The surface activity of silicones: a short review. Ind Engng Chem Prod Res Dev 1980;19:97–103.
[68] Fink HF. Silicone surfactants. Part IV. Silicone surfactants as paint additives. Tenside Surfactants Deterg 1991;28: 306–12.
[69] Dams R. Fluortenside für farben und coatings. Tenside Surfactants Deterg 1993;30:326–7.
[70] Schmidt G. Silicone surfactants. Silicone surfactants. Part III. Organomodified polydimethylsiloxanes as surface active ingredients in textile and fibre industry. Tenside Surfactants Deterg 1990;27(5):324–8.
[71] Gradzielski M, Hoffmann H, Robisch P, Ulbricht W, Grüning B. The aggregation behaviour of silicone surfactants in aqueous solutions. Tenside Surfactants Deterg 1990;27(6):366–79.
[72] Antonietti M, Kaul A, Thünemann A. Complexation of lecithin with cationic polyelectrolytes—plastic membranes as models for the structure of the cell membrane. Langmuir 1995;11(7):2633–8.
[73] Thünemann A. Immobilization of retinoic acid by cationic polyelectrolytes. Langmuir 1997;13(23):6040–6.
[74] Klein KD, Schaefer D, Lersch P. Anionische silicontenside. Tenside Surfactants Deterg 1994;31:115–9.
[75] Falbe J, Regitz M. Römpp lexikon chemie. Stuttgart: Thieme; 1995.
[76] Antonietti M, Wenzel A, Thünemann AF. The egg-carton phase—a new morphology of complexes of polyelectrolytes with natural lipid mixtures. Langmuir 1996;12(8):2111–4.
[77] Thünemann AF, Kublickas RH. Low surface energy polysiloxane complexes. J Mater Chem 2001;11(2):381–4.
[78] Roitman JN, Pittman AG, Ward WH. Fabric oil repellency as related to the critical surface tension and stiffness of coating material. Textile Res J 1974;44:500–11.
[79] Patents: EP 0,472,215,A2; EP 0,380,972,A2; EP 0,567,969,A1; EP 0,757,081,A2; EP 0,745,604,A2; US 5,321,083; EP 0,744,443,A2; EP 0,690,088,A2; DE 40,22,443,A1.
[80] Swain GW, Nelson WG, Preedeekanit S. The influence of biofouling adhesion and biotic disturbance on the development of fouling communities on non-toxic surfaces. Biofouling 1998;12(1):257–69.
[81] Watermann B, Berger HD, Sönnichsen H, Willemsen P. Performance and effectiveness of non-stick coatings in seawater. Biofouling 1997;11(2):101–18.
[82] Richtlinie 98/8/EG des Europäischen Parlaments und des Rates vom 16. Februar 1998 über das Inverkehrbringen von Biozidprodukten.
[83] Lindner E. A low surface free energy approach in the control of marine biofouling. Biofouling 1992;6(2): 193–204.
[84] Fox HW, Zisman WA. The spreading of liquids on low energy surfaces. II. Modified polytetrafluoroethylene polymers. J Colloid Sci 1950;7:109.
[85] Wacker-Chemie GmbH, Burghausen, Germany.
[86] Thomas RR, Anton DR, Graham WF, Darmon MJ, Sauer BB, Stika KM, Swartzfager DB. Preparation and surface properties of acrylic polymers containing fluorinated monomers. Macromolecules 1997;30(10):2883–90.
[87] Thünemann AF, Ruppelt D, Schnablegger H, Blaul J. Rigid-rod complex of a cationic poly(*p*-phenylene) and a fluorinated amphiphile. Macromolecules 2000;33(6):2124–8.

[88] Neher D. Substituted rigid rod-like polymers—building blocks for photonic devices. Adv Mater 1995;7(8):691–702.
[89] Graupner W, Grem G, Meghdadi F, Paar CH, Leising G, Scherf U, Müllen K, Fischer W, Stelzer F. Electroluminescence with conjugated polymers and oligomers. Mol Cryst Liq Cryst 1994;256:549–54.
[90] Leising G, Tasch S, Graupner W. Handbook of conducting polymers, 2nd ed. New York: Marcel Decker; 1997. p. 847.
[91] Cimrova V, Schmidt W, Rulkens R, Schulze M, Meyer W, Neher D. Adv Mater 1996;8(7):585–8.
[92] Piaggi A, Lanzani G, Bongiovanni G, Mura A, Graupner W, Meghdadi F, Leising G. Emission properties of *para*-hexaphenyl polycrystalline films. Phys Rev B 1997;56(16):10133–7.
[93] Graupner W, Meghdadi F, Leising G, Lanzani G, Nisoli M, De Silvestri S, Fischer W, Stelzer F. Photoexcitation in *para*-hexaphenyl. Phys Rev B 1997;56(16):10128–32. and references therein.
[94] Guha S, Graupner W, Resel R, Chandrasekhar M, Chandrasekhar HR, Glaser R, Leising G. Planarity of *para*-hexaphenyl. Phys Rev Lett 1999;82(18):3625–8.
[95] Liu TB, Rulkens R, Wegner G, Chu B. Laser light scattering study of a rigid-rod polyelectrolyte. Macromolecules 1998; 31(18):6119–28.
[96] Petekidis G, Vlassopoulos D, Fytas G, Rülkens R, Wegner G. Diffusion dynamics of hairy-rod polymers in concentrated solutions. Macromolecules 1998;31(18):6129–38.
[97] Petekidis G, Vlassopoulos D, Fytas G, Rülkens R, Wegner G, Fleischer G. Orientation dynamics and correlations in hairy-rod polymers—concentrated regime. Macromolecules 1998;31(18):6139–47.
[98] Brunner S, Caseri WR, Suter UW, Hähner G, Brovelli D, Spencer ND, Vinckier A, Rau IU, Galda P, Rehan M. Preparation and characterization of ultrathin layers of substituted oligo- and poly(*p*-phenylene)s and mixed layers with octadecanethiol on gold and copper. Langmuir 1999;15(19):6333–42.
[99] Rulkens R, Wegner G, Thurn-Albrecht T. Cylindrical micelles of wormlike polyelectrolytes. Langmuir 1999;15(12): 4022–5.
[100] Antonietti M, Conrad J, Thünemann A. Polyelectrolyte–surfactant complexes: a new type of solid, mesomorphous material. Macromolecules 1994;27:6007–11.
[101] Thünemann AF, Ruppelt D. Layered nanoarchitecture of a fluorescent polyelectrolyte complex. Langmuir 2000;16(7): 3221–6.
[102] Kraft A, Grimsdale AC, Holmes AB. Electroluminescent conjugated polymers—seeing polymers in a new light. Angew Chem Int Ed 1998;37(4):402–28.
[103] Hide F, Diaz-Garcia MA, Schwartz BJ, Heeger AJ. New developments in the photonic application of conjugated polymers. Acc Chem Res 1997;30(10):430–6.
[104] Pei QB, Yu G, Zhang C, Yang Y, Heeger AJ. Semiconducting polymers—a new class of solid-state laser materials. Science 1995;269:1086–8.
[105] Halkyard CE, Rampey ME, Kloppenburg L, Studer-Martinez SL, Bunz UHF. Evidence of aggregate formation for 2,5-dialkylpoly(*p*-phenyleneethynylenes) in solution and thin films. Macromolecules 1998;31(25):8655–9.
[106] Häger H, Heitz W. Synthesis of poly(phenyleneethynylene) without diine defects. Macromol Chem Phys 1998;199(9): 1821–6.
[107] Schnablegger H, Antonietti M, Göltner C, Hartmann J, Cölfen H, Samori P, Rabe JP, Häger H, Heitz WJ. Morphological characterization of the molecular superstructure of polyphenylene ethynylene derivatives. Colloid Interf Sci 1999; 212(1):24–32.
[108] Hosemann R, Bagchi SN. Direct analysis of diffraction by matter. Amsterdam: North-Holland; 1962.
[109] Klug HP, Alexander LE. X-ray diffraction procedures for polycrystalline and amorphous materials, 2nd ed. New York: Wiley-Interscience; 1974.
[110] Ruland W. Fourier transform methods for random-layer line profiles. Acta Crystallogr 1967;22:615–23.
[111] Ruland W, Tompa H. The effect of preferred orientation on the intensity distribution of (*hk*) interferences. Acta Crystallogr 1968;24:93–9.
[112] Von Berlepsch H, Burger C, Dautzenberg H. Polyelectrolyte-mediated undulation of surfactant bilayers. Phys Rev E 1998;58(6):7549–52.
[113] Goetz R, Helfrich WJ. The Egg-carton theory of a periodic superstructure of some lipid membranes. Phys II Fr 1996; 6(2):215–23.
[114] Müller M, Schick M. Structure and nucleation of pores in polymeric bilayers—a Monte Carlo simulation. J Chem Phys 1996;105(18):8282–92.

[115] Goetz R, Gompper G, Lipowsky R. Mobility and elasticity of self-assembled membranes. Phys Rev Lett 1999;82(1): 221–4.
[116] Reiter G, Sharma A, Casoli A, David MO, Khanna R, Auroy P. Thin film instability induced by long-range forces. Langmuir 1999;15(7):2551–8.
[117] Vandenbrouck F, Valignat MP, Cazabat AM. Thin nematic films: metastability and spinodal dewetting. Phys Rev Lett 1999;82(13):2693–6.
[118] Kloppenburg L, Jones D, Claridge JB, Loye HC, Bunz UHF. Poly(*p*-phenyleneethynylene)s are thermotropic liquid crystalline. Macromolecules 1999;32(13):4460–3.
[119] Thünemann AF. Nanostructured dihexadecyldimethylammonium–poly(1,4-phenylene–ethinylene–carboxylate): an ionic complex with blue electroluminescence. Adv Mater 1999;11(2):127–30.
[120] Bradly D. Electroluminescent polymers: materials, physics and device engineering. Curr Opin Solid State Mater Sci 1996;1:789–97.
[121] Segura JL. The chemistry of electroluminescent organic materials. Acta Polym 1998;49(7):319–44.
[122] Grell M, Bradley DDC. Polarized luminescence from oriented molecular materials. Adv Mater 1999;11(11): 895–905.
[123] Kalinowski D. Electroluminescence in organics. J Phys D—Appl Phys 1999;32(24):179–249.
[124] Zhang XJ, Jenekhe SA. Electroluminescence of multicomponent conjugated polymers. 1. Roles of polymer/polymer interfaces in emission enhancement and voltage-tunable multicolor emission in semiconducting polymer/polymer heterojunctions. Macromolecules 2000;33(6):2069–82.
[125] Heeger AJ, Diaz-Garcia MA. Semiconducting polymers as materials for photonic devices. Curr Opin Solid State Mater Sci 1998;3(1):16–22.
[126] Ho PKH, Kim JS, Burroughes JH, Becker H, Li SFY, Brown TM, Cacialli F, Friend RH. Molecular-scale interface engineering for polymer light-emitting diodes. Nature 2000;404(6777):481–4.
[127] Watanabe J, Ono H, Uematsu I, Abe A. Thermotropic polypeptides. 2. Molecular packing and thermotropic behavior of poly(L-glutamates) with long *n*-alkyl side chains. Macromolecules 1985;18:2141–8.
[128] Thünemann AF, Beyermann J, Ferber C, Löwen H. Immobilization of retinoic acid by polyamino acids: lamellar-structured nanoparticles. Langmuir 2000;16(2):850–7.
[129] Rulkens R, Wegner G, Thurn-Albrecht T. Cylindrical micelles of wormlike polyelectrolytes. Langmuir 1999;15(12): 4022–5.
[130] Baur JW, Kim S, Balada PB, Reynolds JR, Rubner MF. Thin-film light-emitting devices based on sequentially adsorbed multilayers of water-soluble poly(*p*-phenylene)s. Adv Mater 1998;10(17):1452–5.
[131] Häger H. PD Thesis (ISBN 3-932149-52-1). Marburg, Germany; 1996. p. 38.
[132] Moore JS. Molecular architecture and supramolecular chemistry. Curr Opin Solid State Mater Sci 1996;1(6):777–88.
[133] Brown SP, Schnell I, Brand JD, Müllen K, Spiess HW. An investigation of pi–pi packing in a columnar hexabenzocoronene by fast magic-angle spinning and double-quantum H-1 solid-state NMR spectroscopy. J Am Chem Soc 1999;121(28):6712–8.
[134] Boden N, Bushby RJ, Clements J, Luo R. Characterization of the cationic species formed in p-doped discotic liquid crystals. J Mater Chem 1995;5(10):1741–8.
[135] Arikainen EO, Boden N, Bushby RJ, Clements J, Movaghar B, Wood A. Effects of side-chain length on the charge transport properties of discotic liquid crystals and their implications for the transport mechanism. J Mater Chem 1995; 5(12):2161–5.
[136] Iyer VS, Wehmeier M, Brand JD, Keegstra MA, Müllen K. From hexa-*peri*-hexabenzocoronene to superacenes. Angew Chem Int Ed 1997;36(15):1604–7.
[137] Stabel A, Herwig P, Müllen K, Rabe JP. Diodelike current–voltage curves for a single molecule—tunneling spectroscopy with submolecular resolution on an alkylated, *peri*-condensed hexabenzocoronene. Angew Chem Int Ed 1995;34(15):1609–11.
[138] van de Craats AM, Warman JM, Müllen K, Geerts Y, Brand JD. Rapid charge transport along self-assembling graphitic nanowires. Adv Mater 1998;10(1):36.
[139] Thünemann AF, Ruppelt D, Ito S, Müllen K. Supramolecular architecture of a functionalized hexabenzocoronene and its complex with polyethyleneimine. J Mater Chem 1999;9(5):1055–7.
[140] Brandrup J, Immergut EH, 3rd ed. Polymer handbook, vol. V/16. New York: Wiley; 1989.

[141] Ponomarenko EA, Waddon AJ, Tirell DA, MacKnight WJ. Structure and properties of stoichiometric complexes formed by sodium poly(alpha, L-glutamate) and oppositely charged surfactants. Langmuir 1996;12(9):2169–72.
[142] Herwig P, Kayser CW, Müllen K, Spiess HW. Columnar mesophases of alkylated hexa-*peri*-hexabenzocoronenes with remarkably large phase widths. Adv Mater 1996;8(6):510–2.
[143] Antonietti M, Neese M, Blum G, Kremer F. Dielectric and mechanic relaxation in polyelectrolyte-supported bilayer stacks—a model for the dynamics of membranes. Langmuir 1996;12(18):4436–41.
[144] Thünemann AF, Ruppelt D, Burger C, Müllen K. Long-range ordered columns of a hexabenzo[*bc*,*ef*,*hi*,*kl*,*no*,*qr*]coronene–polysiloxane complex: towards molecular nanowires. J Mater Chem 2000;10(6):1325–9.
[145] Ikkala O, Ruokolainen J, Torkkeli M, Tanner J, Serimaa R, ten Brinke G. Ordering in self-organizing comb copolymer-like systems obtained by hydrogen bonding between charged or noncharged polymers and amphiphiles. Colloids Surf A—Physicochem Engng Aspects 1999;147(1–2):241–8.
[146] Fechtenkötter A, Saalwächter K, Harbison MA, Müllen K, Spiess HW. Highly ordered columnar structures from hexa-*peri*-hexabenzocoronenes—synthesis, X-ray diffraction, and solid-state heteronuclear multiple-quantum NMR investigations. Angew Chem Int Ed Engl 1999;38(20):3039–42.
[147] Krappe U, Stadler R, Voigtmartin I. Chiral assembly in amorphous ABC triblock copolymers—formation of a helical morphology in polystyrene-*block*-polybutadiene-*block*-poly(methylmethacrylate) block copolymers. Macromolecules 1995;28:4558–61.
[148] Ruland W. Carbon fibers. Adv Mater 1990;2(10):528–36.
[149] Fontes E, Heiney PA, Ohba M, Haseltine JN, Smith AB. Molecular disorder in columnar-phase discotic liquid-crystal strands. Phys Rev Ser A 1988;37:1329–34.
[150] German Patent Application DE 10061573,2.
[151] Thünemann AF, Ruppelt D. Electroluminescent polyelectrolyte surfactant complexes. Langmuir 2001;17(16):5098–102.
[152] Zhou SQ, Chu B. Assembled materials: Polyelectrolyte-surfactant complexes. Advanced Materials 2002;12(8):545–56.